**City, University of London**
School of Mathematics, Computer Science & Engineering
Department of Mechanical Engineering & Aeronautics


# HIGH-FIDELITY SIMULATIONS OF FULLY SUBMERGED, RIGID CANOPY FLOWS

Ph.D. in Aeronautical Engineering

Ph.D. student: Alessandro MONTI
Supervisor: Dr. Mohammad OMIDYEGANEH
Co-Supervisor: Prof. Alfredo PINELLI

July 2019

# Contents

# List of Tables

# List of Figures

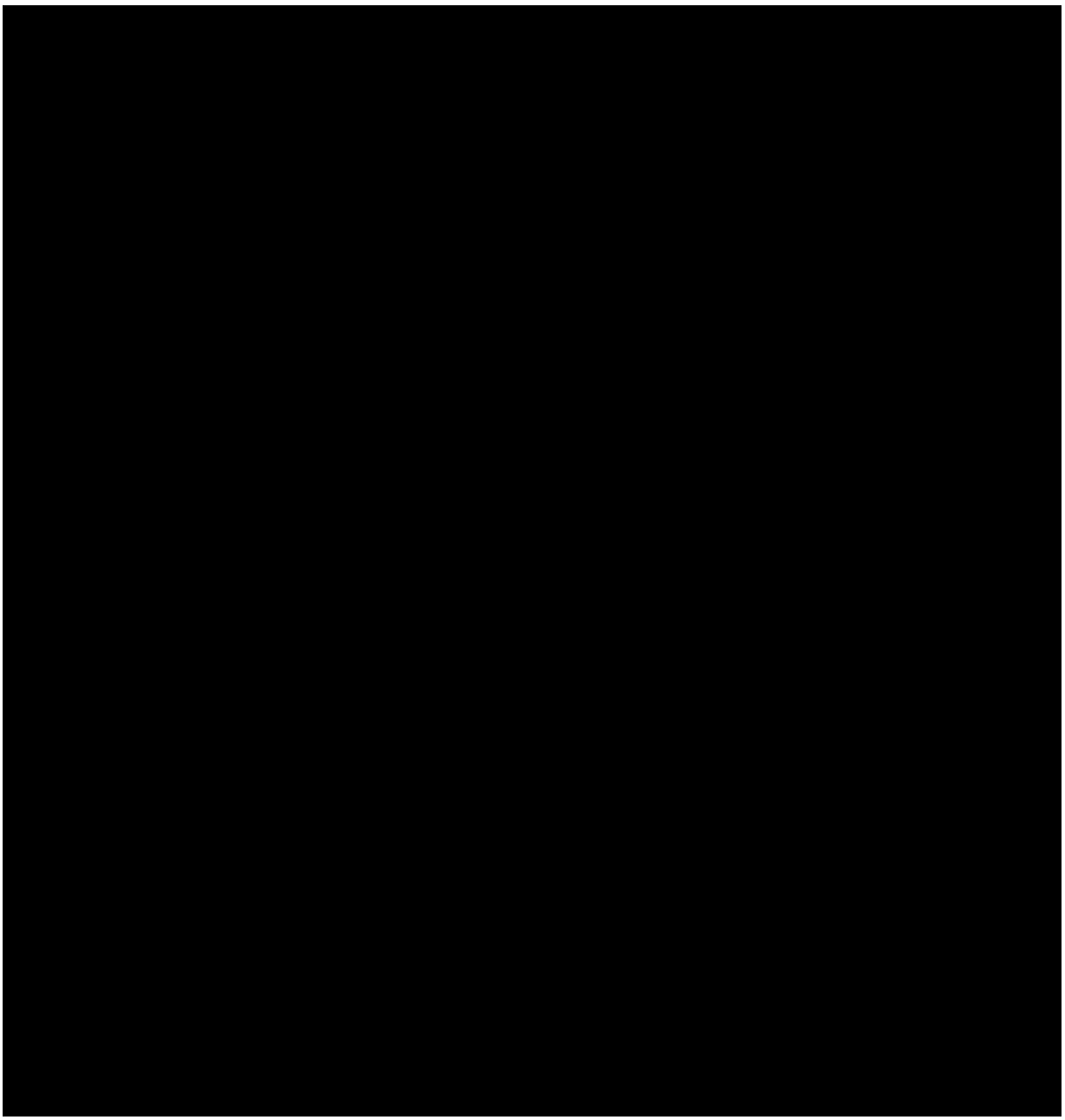

## Abstract

A detailed analysis of turbulent flows in an open channel over rigid submerged canopies, at a moderate bulk Reynolds number (i.e. $Re_b = U_b H/\nu = 6000$, $H$ being the open channel depth and $U_b$ the bulk velocity) has been carried out. Untangling the physical behaviour of these flows can become an impossible task if all the parameters that govern their physics are kept into account, e.g. the density of the layer, the level of submersion of the canopy and the flexibility of the stems, just to mention few of them. Nepf (2012a), after reviewing a number of relevant previous research works on canopy flows in her annual review, suggests to classify the behaviour of the flow by considering the geometrical features of the filamentous layer only. In the case of submerged canopies, based on the solidity of the canopy, three particular regimes are identified: *sparse*, *dense* and *transitional*. While sparse canopies are treated as rough walls, the form drag yielded by the filaments in a dense canopy induces the onset of two inflection points in the mean velocity profile. These two inflection points divide the intra-canopy flow into separate regions: an inner region, very close to the bed, populated by stems generated wakes, an outer region that mainly extends above the canopy and is usually modelled as a flow over a porous/rough wall, and an overlap region (Poggi et al., 2004). The latter can be assumed to behave as a peculiar *Couette* flow (in the literature it has been also described as a mixing-layer region, see Finnigan, 2000) characterised by large fluctuations produced by the meandering of the flow in between the canopy elements. Finally, the transitional regime can be thought of as a dense regime with a higher penetration of the upper layer flow structures into the canopy, where they concentrate (Nepf, 2012a).

Although some phenomenological models for dense canopy regimes are proposed in the literature, they are either based on two-dimensional or even local one-dimensional measurements (Ghisalberti and Nepf, 2004, Nepf, 2012a, Poggi et al., 2004, Raupach et al., 1996) or on numerical simulations that adopt simplified canopy models (Bailey and Stoll, 2013, 2016, Finnigan et al., 2009, Watanabe, 2004). In this context, the present thesis provides an accurate and detailed characterisation of canopy flows through a fully resolved, numerical approach tackling rigid, filamentous canopies made of cylindrical stems mounted normally to an impermeable wall. Firstly, a transitional-dense regime has been considered. Specifically, the first part of the thesis provides a novel and detailed insight that includes a new phenomenological model that also covers the character of the flow within the canopy. Moreover, an original scaling for the mean flow quantities is also proposed. The new approach allows highlighting important similarities and simplify the analysis.

In the second part of the thesis, a parametric study aimed to investigate the relation between the height of the canopy (i.e. its solidity) and the flow regimes is performed. Specifically, four canopy configurations have been considered. All

of them share the same in-plane solid fraction while the canopy to open channel height ratio, $h/H$, has been selected within the range $h/H = [0.05, 0.4]$. The lowest and the highest values are representative of a quasi- sparse and a dense canopy regime, respectively. The other two $h/H$ ratios nominally belong to the transitional regime values. The systematic variation of the height of the filamentous layer allowed us to unravel the main features characterising the different regimes. Particular attention has been paid to the relative locations of the two inflection points of the mean velocity profile and the virtual wall origin (origin seen from the outer flow located in the canopy layer). In view of the relative variations of their distance from the wall and the canopy tip, we propose to adopt the crossing between the internal inflection point and the virtual origin as a condition to infer the transition between canopy flow regimes when the solidity is varied. The structures of the different regimes have been also compared, highlighting the role played by the increasing solidity of the canopy as a natural splitter between the logarithmic structures of the outer flow and the coherent structures located inside the canopy. The wall-normal permeability of the canopy is identified as the main vehicle to transfer momentum through the different canopy layers, playing an important role in shaping the structures of the flow within the filamentous layer. Finally, a new scaling that adapts the flow conditions to the sparsity of the canopy is proposed.

All the results presented in the thesis have been obtained through fully resolved simulations. To the best of our knowledge, this is the first time that a simulation directly tackles the region occupied by the canopy imposing the zero-velocity condition on every single stem by means of an immersed boundary method, thus overcoming the problem of the canopy modelling. Conversely, the outer flow is dealt with a large-eddy formulation that adopts a state-of-the-art grid independent closure for the unresolved scales of motion (Piomelli et al., 2015, Rouhi et al., 2016).

***Keywords:*** canopy flow, scaling, large coherent structures, large-eddy simulation, immersed boundary method.

# Nomenclature

### Mathematical Symbols

| | |
|---|---|
| $\mathcal{C}$ | Convolution operator |
| $\mathcal{D}$ | Divergence operator |
| $\mathcal{G}$ | Gradient operator |
| $\mathcal{I}$ | Interpolation operator |
| $\mathcal{L}$ | Laplacian operator |
| $\mathcal{N}$ | Nonlinear operator |
| $\mathbb{R}$ | Real numbers set |
| $\mathbb{Z}$ | Integer numbers set |

### Greek Characters

| | |
|---|---|
| $\Gamma$ | Surface of the immersed body |
| $\Delta l$ | Grid spacing in a generic direction |
| $\Delta S$ | Average linear spacing between two consecutive filaments |
| $\Delta t$ | Time step |
| $\Delta U$ | Velocity difference between the low- and the high-speed free-stream regions in a mixing-layer |
| $\Delta U^+$ | Roughness function |
| $\Delta V$ | Volume of a single CV |
| $\Delta x$ | Grid spacing in the streamwise direction |
| $\Delta y$ | Grid spacing in the wall-normal direction |

| | |
|---|---|
| $\Delta z$ | Grid spacing in the spanwise direction |
| $\Lambda_x$ | Streamwise wavelength of the initial Kelvin-Helmholtz instability in a mixing-layer |
| $\Phi_{u'u'}$ | Spectrum of the streamwise velocity fluctuations component |
| $\Phi_{v'v'}$ | Spectrum of the wall-normal velocity fluctuations component |
| $\Phi_{w'w'}$ | Spectrum of the spanwise velocity fluctuations component |
| $\Phi_{u'v'}$ | Cospectrum of the streamwise and wall-normal velocity fluctuations components |
| $\Omega$ | Domain size |
| $\Omega_I$ | Support size |
| $\alpha$ | Stretching factor |
| $\delta$ | Dilation parameter |
| $\delta_e$ | Penetration length |
| $\delta_{ij}$ | Kronecker's delta |
| $\delta_\nu$ | Viscous length |
| $\delta_\omega$ | Vorticity thickness |
| $\epsilon$ | Characteristic volume related to the local dilation coefficients of the window function |
| | Turbulence dissipation |
| $\vec{\epsilon}$ | Characteristic volume vector related to the local dilation coefficients of the window function |
| $\eta$ | Dilation parameter |
| $\kappa$ | Von Karman constant |
| | Modified wavenumber |
| $\kappa_x$ | Streamwise wavenumber |
| $\kappa_z$ | Spanwise wavenumber |
| $\lambda$ | Solidity |

| | |
|---|---|
| | Interpolation factor |
| $\lambda_{eff}$ | Effective solidity |
| $\lambda_x$ | Streamwise wavelength |
| $\lambda_z$ | Spanwise wavelength |
| $\mu$ | Dynamic viscosity |
| $\nu$ | Kinematic viscosity |
| $\nu_t$ | Subgrid viscosity |
| $\rho$ | Density |
| $\sigma$ | Dilation parameter |
| $\tau$ | Total shear stress |
| $\tau_{ij}$ | Generic component of the viscous stress tensor |
| | Generic component of the subgrid stress tensor |
| $\phi$ | Projection variable |
| $\phi_{eddy}$ | Eddy diameter |
| $\omega_x$ | Streamwise vorticity component |
| $\omega_y$ | Wall-normal vorticity component |
| $\omega_z$ | Spanwise vorticity component |

**Roman Characters**

| | |
|---|---|
| $A$ | Matrix of the discrete integral of the product between two window functions centred in two different Lagrangian nodes |
| $B$ | Vogel number |
| | Log-law parameter |
| $C_D$ | Drag coefficient |
| $C_L$ | Lift coefficient |
| CV | Control Volume |
| $D$ | Drag |

| | |
|---|---|
| | Cylinder diameter |
| DE | Dense |
| $D_0$ | Integral value of the mean drag |
| $D_r$ | Drag per unit length |
| $E$ | Computational node to the east of $P$ |
| $F$ | Generic flux on the surface of a CV |
| $F_i$ | Vectorial field: $i$th component |
| $\boldsymbol{F}$ | Force field on the Lagrangian grid |
| $F^c$ | Convective flux |
| $F^d$ | Diffusive flux |
| $H$ | Open channel height |
| | Half channel height |
| | Rescaling matrix |
| $L$ | Lift per unit length |
| $L^*$ | Reference length |
| $L_s$ | Shear scale |
| $L_x$ | Streamwise length of the domain |
| $L_y$ | Wall-normal length of the domain |
| $L_z$ | Spanwise length of the domain |
| $L_{P,E}$ | Length between nodes $P$ and $E$ |
| $M$ | Matrix of the moments obtained from the reproducing conditions |
| MD | Marginally Dense |
| MS | Marginally Sparse |
| $N$ | Computational node to the north of $P$ |
| | Number of nodes on the Lagrangian grid |

| | |
|---|---|
| $P$ | Pressure |
| | Computational node considered |
| | Turbulence production |
| $Q$ | Generic function integrated over the volume of a CV |
| $Re$ | Reynolds number |
| $Re_b$ | Bulk Reynolds number |
| $Re_\tau$ | Friction Reynolds number |
| $Re_{\tau,l}$ | Local friction Reynolds number |
| $Re_D$ | Reynolds number based on the free-stream velocity and the cylinder diameter |
| $Re_d$ | Reynolds number based on the mean velocity in the canopy layer and the stems diameter |
| $R_{u'u'}$ | Autocorrelation function of the preaveraged streamwise velocity fluctuations |
| $R_{v'v'}$ | Autocorrelation function of the preaveraged wall-normal velocity fluctuations |
| $R_{w'w'}$ | Autocorrelation function of the preaveraged spanwise velocity fluctuations |
| $S$ | Surface |
| | Computational node to the south of $P$ |
| $S_{ij}$ | Generic component of the strain rate tensor |
| TR | Transitional |
| $U^*$ | Reference velocity |
| $U_b$ | Bulk velocity |
| $U_\infty$ | Free-stream velocity |
| $U_{can}$ | Mean streamwise velocity within the canopy |
| $\boldsymbol{U}$ | Velocity field on the Lagrangian grid |
| $V$ | Volume |

| | |
|---|---|
| $W$ | Computational node to the west of $P$ |
| $\boldsymbol{X}$ | Lagrangian grid nodes |
| $a$ | Ratio between the canopy solid frontal area and the volume of interest occupied by the canopy |
| | Adjustable parameter |
| $b$ | Bottom face of a CV |
| $b_i$ | One-dimensional modified window function coefficients |
| $b_{i,j}$ | Two-dimensional modified window function coefficients |
| $b_{i,j,k}$ | Three-dimensional modified window function coefficients |
| $\vec{b}$ | Modified window function coefficients |
| $d$ | Filaments diameter |
| $e$ | East face of a CV |
| $\boldsymbol{e}_\eta$ | Versor parallel to the CV surface |
| $\boldsymbol{e}_\xi$ | Versor directed alongside the line connecting the nodes $P$ and $E$ |
| $\boldsymbol{e}_i$ | Versor in the $i$th direction |
| $\vec{e}_1$ | Zeros vector with first term equal to one |
| $f$ | Generic integrand function |
| | Generic function |
| $f_i$ | Body force: $i$th component |
| $\boldsymbol{f}$ | Body force vector |
| $f_a$ | Approximated function |
| $f(y)$ | Shape function |
| $h$ | Canopy height |
| $i$ | Integer counter |
| $j$ | Integer counter |

| | |
|---|---|
| $k$ | Integer counter |
| | Roughness length |
| $k_s$ | Equivalent sand roughness length |
| $l$ | Integer counter |
| $m$ | Integer counter |
| $m_i$ | Moments obtained from the reproducing conditions |
| $\dot{m}$ | Mass flux |
| $n$ | North face of a CV |
| | Interpolating polynomial degree |
| $n_i$ | Normal versor: $i$th component |
| $\boldsymbol{n}$ | Normal versor |
| $ni$ | Number of nodes in the streamwise direction |
| $nj$ | Number of nodes in the wall-normal direction |
| $nk$ | Number of nodes in the spanwise direction |
| $p$ | Pressure |
| $q$ | Generic integrand function |
| $r$ | Normalised curvilinear coordinate |
| $\boldsymbol{r}$ | Position vector |
| $s$ | South face of a CV |
| | Curvilinear coordinate |
| $t$ | Time |
| | Top face of a CV |
| | Curvilinear coordinate |
| $u$ | Streamwise velocity component |
| $u_i$ | Velocity: $i$th component |

| | |
|---|---|
| $\boldsymbol{u}$ | Velocity vector |
| $u_\tau$ | Friction velocity |
| $u_{\tau,l}$ | Local friction velocity |
| $v$ | Wall-normal velocity component |
| | Curvilinear coordinate |
| $w$ | Spanwise velocity component |
| | West face of a CV |
| $w_\delta$ | Mono-dimensional kernel function |
| $w_{\delta,\eta}$ | Two-dimensional kernel function |
| $w_{\delta,\eta,\sigma}$ | Three-dimensional kernel function |
| $w_\eta$ | Mono-dimensional kernel function |
| $w_\sigma$ | Mono-dimensional kernel function |
| $x$ | Streamwise coordinate |
| | Generic variable |
| $x_i$ | Coordinates: $i$th component |
| $\boldsymbol{x}$ | Grid (or Eulerian grid) nodes |
| $y$ | Wall-normal coordinate |
| $\tilde{y}$ | Wall-normal coordinate with a shifted origin |
| $y_{vo}$ | Wall-normal location of the virtual origin |
| $y_\alpha^+$ | Scaled local wall units |
| $y_s$ | Location of a possible inviscid instability |
| $y_{\Delta S}^+$ | Local wall units scaled with $\Delta S$ |
| $y_h^+$ | Local wall units scaled with $h$ |
| $z$ | Spanwise coordinate |

**Operators**

$\langle \cdot \rangle$ Average in time and in the two homogeneous spatial directions

$\langle \cdot \rangle_x$ Average in the streamwise (homogeneous) spatial direction

$\langle \cdot \rangle_z$ Average in the spanwise (homogeneous) spatial directions

$\cdot'$ Fluctuations value

$\bar{\cdot}$ Quantity related to the resolved field

$\hat{\cdot}$ Fourier coefficient

$\tilde{\cdot}$ Quantity related to the modified window function

**Subscripts**

$\cdot_P$ Quantity related to the node $P$

$\cdot_E$ Quantity related to the node $E$

$\cdot_e$ Quantity related to the east face of a CV

$\cdot_w$ Quantity computed at the wall

$\cdot_h$ Quantity computed at the canopy tip

$\cdot_{in}$ Quantity related to the inner flow, in particular computed at the wall

$\cdot_{old}$ Quantity related to the previous time-step

$\cdot_{out}$ Quantity related to the outer flow, in particular computed at the canopy tip or at the virtual origin

$\cdot_{rms}$ RMS value

**Superscripts**

$\cdot^+$ Wall (or local wall) units

$\cdot^*$ Predicted quantity

$\cdot^\Gamma$ Boundary value of a quantity on the immersed body

$\cdot^n$ Time $n$

# Chapter 1

# Introduction

The considerable attention for bio-inspired technological advances in aeronautics, hydraulics, chemical engineering, environmental, medical and biological sciences highlights the growing interest in unravelling the interaction mechanisms between complex-textured surfaces and fluid flows. Due to the ubiquitous diffusion in nature, filamentous layers exposed to viscous flows constitute a compelling case (Figure 1.1). Living organisms use surfaces with complex texture and their interaction with surrounding fluid flows to achieve several goals, e.g., decrease the skin friction drag (seal fur) (Itoh et al., 2006), control the flight aerodynamics (bird's feathers) (Carruthers et al., 2007), reduce the form drag (shape reconfiguration of tree foliage) (Vogel, 1989). Living organs use ciliated walls for the control of numerous physiological processes like locomotion, digestion, circulation, respiration, and reproduction (Dauptain et al., 2008, Gardiner, 2005). In many cases, the interaction is also characterised by an adaptive reconfiguration of the textured surface as in the case of the lateral side of shark bodies which are covered with a distributed layer of movable micro denticles able to pop up when the local flow direction is reversed (Lang et al., 2014). Vegetation habitats, occupying a large portion of the terrestrial and aquatic lands, picture another important case of fluid flows over filamentous surfaces. Forming a porous medium called the canopy layer, plant elements alter the flow in various ways, slowing down the flow motion by absorbing its momentum, increasing the turbulence intensity of the flow by generating eddies, exchanging radiation energy and sensible heat with the atmosphere, and serving as sources and sinks of numerous trace gases (Lee et al., 2018). A compelling case are vegetative plants (macrophytes) in rivers. Macrophytes significantly affect the stream, controlling the sediment transport, creating habitats for microorganisms, influencing the nutrient transport, and improving water quality (Mars et al., 1999). Their economic impact has been estimated to be over 10 trillion dollars in the globe (Costanza et al., 2016). The societal, technological and economic importance has driven a special interest in unravelling the mechanisms of the interaction between the vegetation and the

Figure 1.1: Example of filamentous surfaces exposed to fluid flows. From top-left to bottom-right: wheat field (photo credit: Adrian Studer), city skyline (Dubai, UAE; photo credit: Anna Shtraus Photography/Getty Images), fur of a seal (pictures taken from harpseals.org), villi in a human small intestine (photo credit: Alamy Stock Photo).

flow. In particular, the turbulent flows over submerged vegetation have received much attention over the last decades. In this regime, the flow-plants interaction triggers the development of large coherent structures that heavily condition the scalar fluxes governing the nutrient exchange, sediment deposition, and the chemical reaction within the vegetative zones.

The research on vegetative canopy flows started with the pioneering study of Ree and Palmer (1949) where, for the first time, a methodology able to determine an estimate of the drag induced by the vegetation in an open channel was put forward, thus allowing to predict the actual discharge capacity. From that first relevant paper, the research on canopy flows started bursting in the fluid-mechanics field. A witness of this effect is the featuring of the topic in three annual reviews that shape, like milestones, the present knowledge on these flows (Finnigan, 2000, Nepf, 2012a, Raupach and Thom, 1981). Nowadays, the state-of-the-art research seems to suggest that untangling the physical behaviour of these flows can become an impossible task when the effect of all possible parameters are kept into account: vegetation distribution and density, macrophytes stiffness, level of submersion and Reynolds number just to mention few of them.

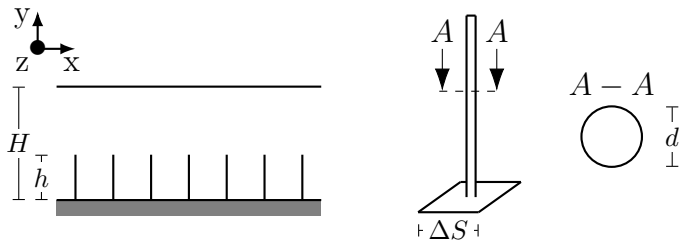


Figure 1.2: Geometrical parameters governing a canopy flow according to Nepf (2012a). In our simulation, the filaments are randomly distributed on the canopy bed, each one occupying an average area $\Delta S^2$.

In recent contributions on aquatic plants, Nepf (2012a) and her collaborators proposed to classify canopy flows only considering their geometrical properties. In particular, the ratio between the flow depth $H$ and the canopy height $h$ (see Figure 1.2), i.e. the level of submersion, is used to distinguish canopies as emergent ($H/h = 1$), shallow submerged ($1 < H/h < 5$) and deeply submerged ($H/h > 10$). This subdivision separates canopy flows according to the relative importance between turbulent stresses, pressure gradient and drag forces (Nepf and Vivoni, 2000). For emergent canopies, the turbulence length scale is imposed either by the stem diameter $d$ or by the average spacing between filaments $\Delta S$ (see Figure 1.2) if the latter is smaller than the former (Nepf, 2012a). In these types of canopy flows, the momentum equation reduces to a balance between the drag force and the pressure gradient driving the mean flow. The consequence of this balance is a self-similar velocity profile (Lightbody and Nepf, 2006) which only depends on the ratio between the frontal area and the canopy volume of influence $a(y) = d(y)/\Delta S^2$. Submerged canopies substantially differ from the emergent ones. The flow approaches two limiting regimes (Nepf, 2012a, Poggi et al., 2004), a sparse and a dense one that are obtained by varying the canopy solidity, defined as

$$\lambda = \int_0^h a(y)\,\mathrm{d}y, \tag{1.1}$$

i.e. the ratio between the frontal area of the canopy and the bed area, that in case of uniform diameter reduced to

$$\lambda = \frac{d\,h}{\Delta S^2}. \tag{1.2}$$

In particular, if $\lambda$ is much smaller than a threshold value (i.e. $\lambda \ll 0.1$) then the flow velocity within and above the canopy shows a behaviour comparable to the one observed in a turbulent boundary layer over a rough wall with a dominance of bed drag over the actual canopy form drag. Conversely, for large

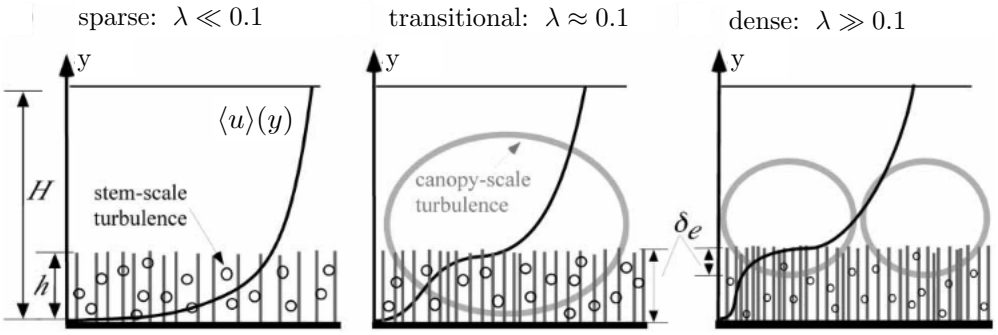


Figure 1.3: Sketch of the typical mean velocity profiles shape of canopy flows in sparse (left image), transitional (middle image) and dense (right image) regimes. The typical dominant turbulence scales are also sketched. Image courtesy of Nepf (2012b).

values of $\lambda$ (i.e. $\lambda \gg 0.1$), the canopy drag becomes larger than the one offered by the bed (see Figure 1.3). This condition, termed dense regime, features a drag discontinuity at the top of the canopy that, in turns, determines the appearance of an inflection point in the mean velocity profile near the canopy edge and another one close to the canopy bed, leading to the establishment of two separate shear layers. This conceptual classification has been firstly proposed by Belcher et al. (2003). Later, Poggi et al. (2004) carried out an experiment campaign on rigid canopy flows varying the canopy rods density. The obtained results showed that the mean velocity profile has no (or very slight) inflection point at the canopy edge for values $\lambda < 0.04$ (sparse regime). Differently, when $\lambda \gg 0.1$, the mean velocity profile displayed two pronounced inflection points, which is in agreement with the classification by Nepf (2012a). Inspired by their experimental observations, the authors also proposed two phenomenological models. In the sparse regime, the flow is considered to behave like a boundary layer, being the canopy like a canonical rough-wall, while in dense regimes, the flow structure can be envisaged as a weighted superimposition of three different dominant flow behaviours dictated by the actual eddy size that can locally penetrate the canopy (i.e. inner, outer and overlap region). In the inner region, i.e. $y/h \ll 1$, for sufficiently high Reynolds number the flow field would be characterised by the von Kármán street vortices, size and intensity depending on the diameter of the stems. The outer region, i.e. $y/h \gg 2$, would resemble a typical boundary layer over a rough wall, although in shallowly submerged canopies the development of the flow is constrained by the space available between the canopy edge and the free surface. In canopies characterised by a large $H/h$ ratio ($H/h > 10$), the boundary layer region is clearly observable (Finnigan, 2000, Raupach et al., 1996). Finally, in the region overlapping the innermost and outermost zones, by

the canopy edge ($y/h \approx 1$), the flow would behave as a turbulent mixing-layer with a similar inflected mean velocity profile. Similar to the mixing-layer, the inflection point would induce a Kelvin-Helmholtz (KH) instability that develops large scale spanwise rollers of a size comparable to the canopy height (the so-called canopy-scale turbulence) (Nepf, 2012a). In this dense regime, these vortices should control the bulk momentum transport between the outer and the inner regions. Raupach et al. (1996) observed that in a fully developed mixing-layer, the streamwise wavelength of the initial KH instability, $\Lambda_x$, is preserved and in particular, the ratio between $\Lambda_x$ and the vorticity thickness that describes a mixing-layer,

$$\delta_\omega = \frac{\Delta U}{(\mathrm{d}\langle u\rangle/\mathrm{d}y)_{max}}, \tag{1.3}$$

where $\Delta U$ is the velocity difference between the low- and high-speed free-stream regions, falls into a specific range (Finnigan, 2000), $3.5 < \Lambda_x/\delta_\omega < 5$. These authors also suggest that in canopy flows, a direct comparison with the coherent structures appearing in canonical mixing-layer flows can be inferred in the region close to the canopy edge. If the low-speed region velocity of the mixing-layer is much lower than $\langle u\rangle(h)$ (hypothesis verified if the canopy is very dense), the height of this region turns out to be proportional to the thickness of the vorticity layer developing at the canopy tip,

$$L_s = \frac{\langle u\rangle(h)}{(\mathrm{d}\langle u\rangle/\mathrm{d}y)_{(y=h)}} \approx \frac{1}{2}\delta_\omega. \tag{1.4}$$

Raupach et al. (1996) also observed that the ratio between the streamwise wavelength of the KH rollers and the shear scale (1.4) must fall into a specific range, $7 < \Lambda_x/L_s < 10$, the validity of which was confirmed by several experiments over a wide range of canopies with different geometric properties. These experiments also allowed to narrow the suggested range, indicating that a robust relation is obtained by considering $\Lambda_x \simeq 8.1L_s$. Within the same context of dense submerged canopies, Nezu and Sanjou (2008) proposed a model similar to the one proposed by Poggi et al. (2004). They also proposed the existence of three regions with their respective vorticity structure, i.e., the emergent zone, the mixing-layer zone and the log-law zone. These zones may not significantly overlap in space because the production mechanism of each zone would prevent the formation of other types of vorticity (Poggi et al., 2004).

Canopy flexibility adds further complexity to the classification of the flow features. In fact, elastic hairy surfaces can drastically modify the turbulent structures and their entrainment inside the porous layer, depending on the natural frequency of the filamentous surface (Sundin and Bagheri, 2019). In the elastic canopy scenario, the drag exerted by the canopy layer on the mean flow is reduced compared to the rigid case due to the reconfiguration mechanism, i.e.

the new shape of the filaments after the flow-induced deformation (Vogel, 1984). In fact, the filaments bend in response to the fluid motion, thus reducing the projected area perpendicular to the flow, and assume a more streamlined shape (Vogel, 1989). In nature, the reconfiguration is also used as an expedient to avoid uprooting or breaking under strong currents by leaves of terrestrial or aquatic plants (Vogel, 1984). The variation of drag can be represented as a departure from the drag quadratic law with velocity. In particular the Vogel number $B$ was introduced (Vogel, 1989), such that the power law dependence of the drag with the flow velocity reads $D \propto \langle u \rangle^{(2+B)}$, with $-2 < B < 0$. Based on the stiffness of the flexible elements, two asymptotic regimes of reconfiguration were identified. In particular, with objects almost rigid, the reconfiguration effect is almost negligible and the quadratic law for the drag is recovered, i.e. $B \approx 0$. On the other hand, in a regime of strong reconfiguration with the flexible elements completely bent, very specific values of the Vogel number were proposed, depending on the initial shape considered, with the typical value $B = -2/3$, associated with the loss of one characteristic length, such as the bending of a beam or a rectangular plate along a single axis, and $B = -4/3$, if reconfiguration leads to the loss of two characteristic lengths, such as the crumpling of a paper or the rolling of a disk into a cone (Pan et al., 2014). A transitional regime of weak reconfiguration was also considered. In particular, Pan et al. (2014) observed that the Vogel number is maximised in this last regime in correlation with a preferential penetration of strong events into the canopy layer. When these strong events transit on the flexible canopy with sufficient momentum able to generate enough drag to overcome buoyancy and rigidity, the filaments start to move in a synchronous (*honami* for terrestrial vegetation, *monani* for aquatic plants) or asynchronous (*gently swaying*) coherent motions of the filaments can appear (Pan et al., 2014). In particular, Ghisalberti and Nepf (2002) observed that the frequency of the coherent deformation of the filamentous layer was in good agreement with the frequency predicted for the KH instability in free mixing-layers, thus implying the high correlation between the two phenomena (Okamoto and Nezu, 2009). The presence of honami also affects the turbulent momentum exchange and mixing between the canopy and the overlying flow. Honami, in fact, allow the turbulent fluxes to penetrate closer to the bed, but the resulting momentum transfer is less efficient (i.e. lower amplitude of the turbulent shear stresses) compared with rigid canopy scenarios (Nepf, 2012a) because the strong events are dampened by the coherent motions of the vegetation.

Despite the amount of work done to unravel the physics of canopy flow, most of the knowledge accumulated until recent times was based on the limited information obtained from laboratory experiments (Finnigan, 2000, Ghisalberti and Nepf, 2002, 2004, Liu et al., 2008, Nepf, 2012a, Nezu and Sanjou, 2008, Poggi et al., 2004, Raupach et al., 1996) (usually 2D or point-wise measurements) and few numerical predictions based on oversimplified flow-vegetation interaction models

(Finnigan et al., 2009, Harman and Finnigan, 2007, López and García, 2001). In this context, high-fidelity simulations have a potential to become a powerful tool to study vegetative flows, providing researchers with three-dimensional and detailed instantaneous flow representations. Indeed, in the last decade, few large-eddy simulations (LES) of flows over dense canopies (Bailey and Stoll, 2013, 2016, Cui and Neary, 2008, Huang et al., 2009, Watanabe, 2004) modelled by a system of volume forces have demonstrated their capability in unravelling the morphology of the coherent structures above the vegetation layer. Untangling the presence and the dynamics of these structures has also allowed to put forward conceptual models describing their generation and evolution (Bailey and Stoll, 2013, 2016). In particular, the recent simulations obtained by Bailey and Stoll (2016) allowed to shed some more light on the emergence and evolution of the coherent structures of a quasi-dense canopy flow. The authors found that near the canopy, quasi two dimensional mixing-layer-like rollers (similar to those proposed by Raupach et al., 1996) dominate the transport of finer vorticity in and out of the canopy. In particular, the large, spanwise-oriented structures stretch upward forming hairpin vortices that eventually break down, de-correlating from the roller structures, generating a wider range of vorticity scales.

The present thesis is a contribution to the study of canopy flows that sheds some new light on their phenomenology, their structure and on the mechanisms that determine the genesis of the three canopy flow regimes that have been identified to take place in a rigid canopy as a function of its geometrical features by a number of researchers in the last few decades. In particular, the solidity $\lambda$ turns out to be the parameter that allows us to discriminate the flow into three phenomenological different regimes. Although the emergence of a certain regime as a function of $\lambda$ has been determined via experimental evidences (Nepf, 2012a, Poggi et al., 2004), its characterisation, the exact inception condition and the identification of the leading physical mechanisms that promote the appearance or disappearance of the flow structures typical of each canopy flow are still open research topics that need further clarification. Other open questions concern the role played by $\Delta S$ and $h$ in defining $\lambda$ and the role of the filaments inclinations (soft canopies) or their eventual flexibility. Concerning the phenomenology of the flow, it is not well understood how the flow inside the canopy scales including the definition and the importance of the right Reynolds numbers in every region and the related question on the mechanisms governing the interactions between the inner and the outer canopy regions.

The focus of this thesis is on rigid canopy flows with different relative heights ratios, $h/H$. The genesis of each regime is explored in detail providing novel insights on the flow phenomenology and the physical mechanisms promoting the emergence of the various flow conditions described in literature when the solidity changes.

## 1.1 Outline

The outline of the thesis is as follows. In Chapter 2 we present the baseline problem set-up employed in this work. The chapter includes the physical and mathematical definitions of the flow together with the adopted numerical discretisation and its validation. Chapter 3 covers the discussion of the results obtained when considering the flow over a wall-normal rigid canopy in a mildly dense regime as first attempt to analyse the scaling and characterises the flow structures arising from the canopy flow turbulence interaction. The content of this chapter reflects a journal article recently appeared on Physics of Fluids. In Chapter 4 we discuss how the height of the canopy layer influences the transition of the regimes following Nepf's (2012a) classification. In particular we will look at the interaction between the "flow layers" using a detailed spectral analysis of the energy content of the velocity fluctuations. The content of this chapter has been submitted to Journal of Fluid Mechanics and is currently under review. Finally, some conclusions will be drawn at the end of the thesis in Chapter 5 and an outlook on the continuation of this research work will be put forward. The results produced in this thesis have been submitted to the aforementioned archival journals and have been presented at international conferences.

- A. Monti, M. Omidyeganeh, and A. Pinelli. *Large-Eddy Simulation of an open channel flow with submerged rigid vegetation.* EPiC Series in Engineering, 2018;

- A. Monti, M. Omidyeganeh, and A. Pinelli. *Large-Eddy Simulation of an open channel flow with submerged rigid vegetation.* Direct and Large-Eddy Simulation XI - Springer, 2019;

- A. Monti, M. Omidyeganeh, and A. Pinelli (2019). *Large-Eddy Simulation of an open channel flow bounded by a semi-dense rigid filamentous canopy: scaling and flow structure.* Physics of Fluids, 31(6), 065108;

- A. Monti, M. Omidyeganeh, B. Eckhardt and A. Pinelli. *On the genesis of different regimes in canopy flows: a numerical investigation.* Journal of Fluid Mechanics, under review;

- A. Monti, M. Omidyeganeh, and A. Pinelli. *Large-Eddy Simulation of an open channel flow with rigid vegetation.* DLES11, Pisa (Italy), May 2017;

- A. Monti, M. Omidyeganeh, and A. Pinelli. *Large-Eddy Simulation of an open channel flow with rigid vegetation.* IAHR5, Trento (Italy), June 2018;

- A. Monti, M. Omidyeganeh, and A. Pinelli. *Large-Eddy Simulation of an open channel flow with rigid vegetation.* HIC2018, Palermo (Italy), June 2018;
- A. Monti, M. Omidyeganeh, and A. Pinelli. *Large-Eddy Simulations of flows over submerged rigid canopies in different regimes.* ETMM12, Montpellier (France), September 2018;
- A. Monti, M. Omidyeganeh, and A. Pinelli. *Large-Eddy Simulations of flows over rigid canopies in different canopy flow regimes.* APS71, Atlanta (USA), November 2018;
- A. Monti, M. Omidyeganeh, and A. Pinelli. *Large-Eddy Simulation of sparse and dense rigid canopy regimes.* ETC17, Torino (Italy), September 2019;

# Chapter 2

# Methodology

In this work, we will deal with the governing equations of the unsteady isochoric flows, i.e. the incompressible Navier-Stokes equations. The momentum and continuity equations, in an inertial, Cartesian frame of reference, can be written as

$$\begin{aligned} \frac{\partial u_i}{\partial t} + \frac{\partial u_i u_j}{\partial x_j} &= -\frac{\partial p}{\partial x_i} + \frac{1}{Re}\frac{\partial^2 u_i}{\partial x_j \partial x_j} + f_i, \\ \frac{\partial u_i}{\partial x_i} &= 0, \end{aligned} \tag{2.1}$$

where $u_i$ is the $i$th velocity component, $p$ is the pressure acting as a Lagrange multiplier that forces the velocity field to live in a solenoidal space, $f_i$ a volume force, and $Re$ is the Reynolds number. Repeated indices are summed over. To make the set (2.1) nondimensional, we chose a reference length and velocity, $L^*$ and $U^*$, therefore introducing the corresponding Reynolds number $Re = \rho U^* L^*/\mu$, where $\rho$ and $\mu$ are the density and dynamic viscosity of the fluid, respectively. The closure of (2.1) is ensured by imposing the associated boundary conditions and a compatible initial state.

## 2.1 Finite volume method

A numerical solution of the set (2.1) is obtained by applying the Finite Volume Method to the integral form of the equations. An exhaustive discussion on this methodology is contained in Ferziger and Peric (2012) and Rosti (2016) but, to cover every aspect, we shall give here a brief introduction. The incompressible Navier-Stokes equations (2.1) are firstly integrated over an arbitrary control vol-

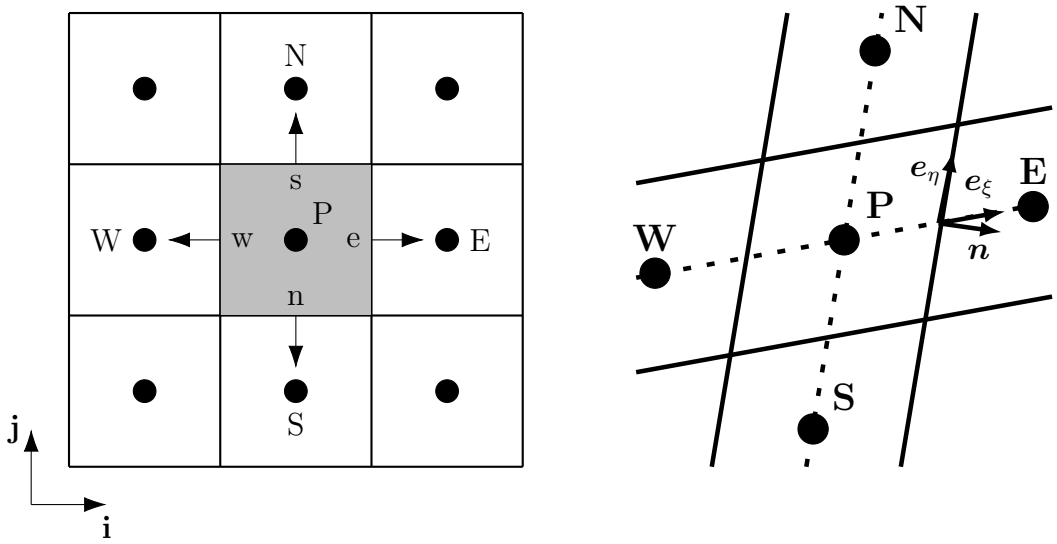


Figure 2.1: Left: a typical CV with the compass notation used for the neighbour cell centres and the CV faces. Right: a typical CV with a skewed grid.

ume $V$,

$$\begin{aligned} \frac{\partial}{\partial t}\int_V u_i \,\mathrm{d}V + \int_S u_i u_j n_j \,\mathrm{d}S = -\int_V \frac{\partial p}{\partial x_i}\,\mathrm{d}V + \int_S \tau_{ij} n_j \,\mathrm{d}S + \int_V f_i \,\mathrm{d}V, \\ \int_S u_i n_i \,\mathrm{d}S = 0, \end{aligned} \tag{2.2}$$

being $S$ the surface that bounds $V$, $n_i$ the $i$th component of the outward versor normal to $S$, and $\tau_{ij}$ the viscous stress tensor

$$\tau_{ij} = \frac{1}{Re}\left(\frac{\partial u_i}{\partial x_j} + \frac{\partial u_j}{\partial x_i}\right). \tag{2.3}$$

To obtain the surface integrals (the fluxes) in (2.2), we applied the Gauss' theorem,

$$\int_V \frac{\partial F_i}{\partial x_i}\,\mathrm{d}V = \int_S F_i n_i \,\mathrm{d}S, \tag{2.4}$$

to a generic differentiable vectorial field $F_i$.

A numerical approximation to (2.2) is obtained by applying the integral equations to every contiguous, non-overlapping Control Volume (CV), in which the solution domain has been subdivided (see Figure 2.1). This method has the peculiarity to be conservative by construction, i.e., considering a CV and its neighbour, the fluxes entering a CV are the same ones exiting the adjacent CV on the sharing

boundary. The computational variables, $u_i$ and $p$, are assigned at the centroid of every CV (colocated approach). In this way, the amount of data to be stored and computed is minimised, and the programming is simplified. The colocated approach has also other significant advantages when dealing with complicated domains, or when the boundary conditions have discontinuities. However, this approach may lead to some difficulties with the pressure-velocity coupling and the occurrence of spurious oscillations in the pressure field, that cause a natural nonconservation of the mass (see §2.1.1).

To find a numerical solution of the set of equations (2.2), a numerical approximation for the volume and surface integrals has to be introduced using quadrature formulae.

Since in this thesis we will only consider CVs with cuboidal shape in three-dimensions (quadrangular in the bi-dimensional scenario), the surface that bounds the CV is composed of six (four) plane faces. In Figure 2.1, a typical 2D control volume used in this work is shown together with the notation we shall use. The extension to the third dimension is straightforward.

Integration over the volume of a CV can be estimated with a second-order accurate approximation, obtained extending the midpoint rule in 3D cases. In this quadrature technique, the integral is estimated as the product of the integrand at the cell centre and the corresponding volume,

$$Q_P = \int_V q \, \mathrm{d}V \approx q_P V_P, \tag{2.5}$$

where $q_P$ is the value of $q$ at the CV centre and $V_P$ is the volume of the respective cell. Having set the computational node in the centroid of the CV, no interpolation to compute $q_P$ is needed.

The net flux through a CV boundary, instead, can be computed as the sum of the contributions over the faces of the CV,

$$\int_S f \, \mathrm{d}S = \sum_k \int_{S_k} f \, \mathrm{d}S, \tag{2.6}$$

where $f$ is any component of a flux vector in the direction normal to the face (e.g., the normal convective or viscous flux in the momentum equations, $\int_S u_i u_j n_j \, \mathrm{d}S$ and $\int_S \tau_{ij} n_j \, \mathrm{d}S$, respectively). Note that, for an incompressible fluid with constant viscosity, the viscous flux reduces to

$$\int_S \tau_{ij} n_j \, \mathrm{d}S = \frac{1}{Re} \int_S \frac{\partial u_i}{\partial x_j} n_j \, \mathrm{d}S. \tag{2.7}$$

The surface integral is estimated using again the midpoint rule, leading to an approximation of second-order accuracy. As an example the flux on the east face

(see Figure 2.1) of a rectangular cell would read as

$$F_e = \int_{S_e} f \, \mathrm{d}S \approx f_e S_e. \tag{2.8}$$

Equation (2.8) requires the values of the variables at the face centre. To obtain these values, we use a linear interpolation between the two nearest nodes, $f_E$ and $f_P$. For example, at location $e$ we have

$$f_e = f_E \lambda_e + f_P (1 - \lambda_e), \tag{2.9}$$

where the linear interpolation factor, $\lambda_e$, is defined as

$$\lambda_e = \frac{x_e - x_P}{x_E - x_P}. \tag{2.10}$$

This method, which corresponds to the first-order approximation Taylor polynomial evaluated in the neighbourhood of $P$, is also second-order accurate and, on a uniform, Cartesian mesh, would correspond to the central-difference approximation of the first derivative in a finite difference framework. The assumption of a linear variation between points $P$ and $E$, provides also a simple method to approximate the derivative,

$$\left( \frac{\partial f}{\partial x} \right)_e \approx \frac{f_E - f_P}{x_E - x_P}. \tag{2.11}$$

We will apply now the approximation principles just described to set (2.2), in order to obtain a spatial discretisation of the equations. The volume integrals, corresponding to the unsteady, pressure and forcing terms, can be easily computed applying equation (2.5). The convective flux $F^c$ is computed by assuming that the mass flux $\dot{m}$ is already known, using the midpoint rule approximation,

$$F_e^c = \int_{S_e} u \, \boldsymbol{u} \cdot \boldsymbol{n} \, \mathrm{d}S \approx \dot{m}_e u_e. \tag{2.12}$$

Here, again for the sake of simplicity, we have considered only the $x$ component of the velocity field, being $\dot{m}_e$ the mass flux through the $e$ face, computed as

$$\dot{m}_e = \int_{S_e} u_j n_j \, \mathrm{d}S \approx (\boldsymbol{u} \cdot \boldsymbol{n})_e \, S_e. \tag{2.13}$$

The approximation of the diffusive flux, $F^d$,

$$F_e^d = \int_{S_e} \frac{1}{Re} \frac{\partial u}{\partial x_j} n_j \, \mathrm{d}S \approx \frac{1}{Re} \left( \boldsymbol{\nabla} u \cdot \boldsymbol{n} \right)_e S_e, \tag{2.14}$$

the gradient of $u$ at the cell face centre is needed. First, we approximate the derivative at the CV centre by the average value over the cell,

$$\left(\frac{\partial u}{\partial x_i}\right)_P \approx \frac{1}{V_P}\int_V \frac{\partial u}{\partial x_i}\,\mathrm{d}V; \tag{2.15}$$

then, the volume integral at the numerator in the above equation can be substitute with a surface integral applying the Gauss' theorem, i.e.

$$\int_V \frac{\partial u}{\partial x_i}\,\mathrm{d}V = \int_S u\boldsymbol{e}_i \cdot \boldsymbol{n}\,\mathrm{d}S \approx \sum_c u_c S_c^i \text{ for } c = e, n, w, s, b, t, \tag{2.16}$$

where $\boldsymbol{e}_i$ is the versor in the $i$th direction. Finally, the derivative can be computed as

$$\left(\frac{\partial u}{\partial x_i}\right)_P \approx \frac{\sum_c u_c S_c^i}{V_P}. \tag{2.17}$$

However, interpolating the derivatives to get the cell face values may not detect the generation of an oscillatory solution. To avoid this problem and prevent oscillatory solutions, we use the so-called *deferred correction* method (Böhmer et al., 1984), where an additional term, which is the difference between the correct and approximated flux, is added. The deferred correction approach adjusts the diffusive flux as follow,

$$F_e^d = F_e^d\mathrm{impl} + \left[F_e^d\mathrm{expl} - F_e^d\mathrm{impl}\right]^{\mathrm{old}}, \tag{2.18}$$

where "old" stands for a value from the previous iteration or time-step, and "impl" or "expl" means that the term is computed using a central difference scheme or the interpolated value on the face centre obtained from (2.17), respectively. Muzaferija (1994) suggested an effective method for quasi-orthogonal grid: when the line connecting nodes $P$ and $E$ is nearly orthogonal to the cell face, the derivative with respect to $\boldsymbol{n}$ can be estimated by a derivative with respect to the coordinate $\boldsymbol{e}_\xi$ along that line, using an implicit flux approximation,

$$F_e^d\mathrm{impl} = \frac{1}{Re}S_e\left(\frac{\partial u}{\partial \xi}\right)_e = \frac{1}{Re}S_e\frac{u_E - u_P}{\|\mathbf{r_E} - \mathbf{r_P}\|}, \tag{2.19}$$

that, in particular, leads to a second order accurate approximation when the line connecting $P$ and $E$ is orthogonal to the surface. When the grid is nonorthogonal, the deferred correction term must contain the difference between the gradient in

the $\boldsymbol{n}$ and $\boldsymbol{e}_\xi$ directions (see Figure 2.1). So, the diffusive flux can be written as

$$F_e^d = \frac{1}{Re} S_e \left(\frac{\partial u}{\partial \xi}\right)_e + \frac{1}{Re} S_e \left[\left(\frac{\partial u}{\partial n}\right)_e - \left(\frac{\partial u}{\partial \xi}\right)_e\right]^{\text{old}}, \tag{2.20}$$

where the first term on the right hand side is the one treated implicitly, while the second one is the deferred correction, which is calculated using interpolated cell centre gradients (2.17), resulting in the following expression for the diffusive fluxes,

$$F_e^d = \frac{1}{Re} S_e \frac{u_E - u_P}{L_{P,E}} + \frac{1}{Re} S_e \left(\boldsymbol{\nabla} u\right)_e^{\text{old}} \cdot \left(\boldsymbol{n} - \boldsymbol{e}_\xi\right), \tag{2.21}$$

i.e. the second term is treated completely explicitly, as opposed to (2.18). If the line connecting nodes $P$ and $E$ is orthogonal to the cell face, the deferred correction term is null as expected. Note that this correction does not affect the overall second-order accuracy of the method.

### 2.1.1 Time discretisation

The numerical solution of the incompressible Navier-Stokes equations is complicated by the lack of an independent equation for the pressure. In fact, the continuity equation represents only a kinematic constraint for the velocity field, without supplying a dynamic equation for a thermodynamic variable, such as pressure or density. Therefore, when dealing with incompressible flows, the thermodynamics becomes meaningless and the absolute pressure is of no significance (only its gradient affects the flow). A way out to this problem is to construct a pressure field that guarantees satisfaction of the continuity constraint. One of the mainstream approaches to accomplish this possibility is to rely on the fractional step method. This technique was firstly developed by Chorin (1968) and later on modified and improved by several other authors. The results obtained in the thesis rely on a modified version of the method originally proposed by Kim and Moin (1985). The algorithm is based on the Helmholtz–Hodge decomposition of the velocity field on a simply connected domain into a solenoidal and an irrotational part, and consists of two stages: the prediction step, where the momentum equation is solved computing a velocity field that does not satisfy the continuity equation, and the correction step, where the previous solution is corrected by projecting the velocity field onto a divergence-free field.

We can write the numerical discretisation of the incompressible Navier-Stokes equations concisely as follows,

$$\frac{\boldsymbol{u}^* - \boldsymbol{u}^n}{\Delta t} = -\mathcal{N}_l\left(\boldsymbol{u}^n, \boldsymbol{u}^{n-1}\right) + \frac{1}{Re}\mathcal{L}\left(\boldsymbol{u}^*, \boldsymbol{u}^n\right) - \mathcal{G}\left(\phi^n\right), \tag{2.22}$$

$$\frac{\boldsymbol{u}^{n+1} - \boldsymbol{u}^*}{\Delta t} = -\mathcal{G}\left(\phi^{n+1}\right), \tag{2.23}$$

with the constraint

$$\mathcal{D}\left(\boldsymbol{u}^{n+1}\right) = 0, \tag{2.24}$$

where $\boldsymbol{u}^*$ is the predicted velocity field, $\boldsymbol{u}^n$ the solenoidal velocity field at time $n$, $\Delta t$ the time step, $\mathcal{N}_l$, $\mathcal{G}$, $\mathcal{D}$ and $\mathcal{L}$ are the discrete nonlinear, gradient, divergence and Laplacian operators, respectively, and $\phi$ is the projection variable. Note that, the operators include coefficients that are specific to the selected time scheme. The variable $\phi^{n+1}$ to be used in the projection step (2.23) can be found by solving a Poisson's equation for $\phi$, obtained by applying the divergence operator to equation (2.23), which gives

$$\mathcal{L}\phi^{n+1} = \frac{1}{\Delta t}\mathcal{D}\left(\boldsymbol{u}^*\right), \tag{2.25}$$

with the boundary condition

$$\frac{\partial \phi^{n+1}}{\partial n} = 0, \tag{2.26}$$

being $\boldsymbol{n}$ the outward normal vector. So, the fractional step method used to solve the incompressible Navier-Stokes equations can be resumed with a sequence of phases, i.e. a prediction step (2.22), the solution of a Poisson's equation (2.25), and a final correction step (2.23) that ensures the divergence-free property of the velocity field. From a computational point if view, the most expensive step is the one related with the solution of the Poisson pressure equation. However, when one of the directions is homogeneous, periodic boundary conditions can be assumed and a $3D$ Poisson's equation can be transformed into a series of two-dimensional Helmholtz equations in the wave numbers space via a discrete fast Fourier transform (FFT). In particular, assuming the spanwise direction $z$ to be the periodic direction, $\phi$ is transformed in the wave number space using the discrete anti-transform

$$\phi\left(x, y, z\right) = \sum_{l=0}^{N-1} \hat{\phi}_l\left(x, y\right) exp\left(ilz\right), \tag{2.27}$$

where $\hat{\phi}_l$ is the $l$th Fourier coefficient of $\phi$ and $N$ is the number of modes considered (i.e., $l = 0, \ldots, N-1$). Using the orthonormality of the Fourier basis, we obtain a set of $N$ decoupled Helmholtz equations,

$$\frac{\partial^2 \hat{\phi}_l}{\partial x^2} + \frac{\partial^2 \hat{\phi}_l}{\partial y^2} - \kappa_l \hat{\phi}_l = \hat{r}_l, \tag{2.28}$$

where $\kappa_l$ is the modified wave number and $\hat{r}_l$ is the Fourier transform of the right

hand side of equation (2.25). Further details can be found in Canuto et al. (2012).

When a colocated arrangement of variables on a numerical grid is used, the divergence term of equation (2.25) requires the values of the velocities at cell faces that can be obtained by linear interpolation. As a consequence, the Poisson's equation needs to be discretised on a grid which is coarser than the one used for the predicted variables. The mismatch in the number of discrete values makes the kernel of the pressure operator nontrivial, giving rise to pressure spurious modes. To eliminate those modes we use a method originally proposed by Rhie and Chow (1983). Initially, we solve the momentum equation as usual, and then, before solving the Poisson's equation, the mass fluxes obtained with the interpolated velocity are corrected by subtracting the difference between the pressure gradient and the interpolated gradient at the cell face location obtained at the previous time step, in a sort of deferred correction fashion (2.18),

$$\dot{m}_e = (\boldsymbol{u} \cdot \boldsymbol{n})_e S_e - \Delta t S_e \left[ (p_E - p_P) - \boldsymbol{\nabla} p \cdot \boldsymbol{e}_\xi \right]^{\text{old}} . \tag{2.29}$$

This method automatically detects the oscillations and smooths them out.

### 2.1.2 Numerical implementation

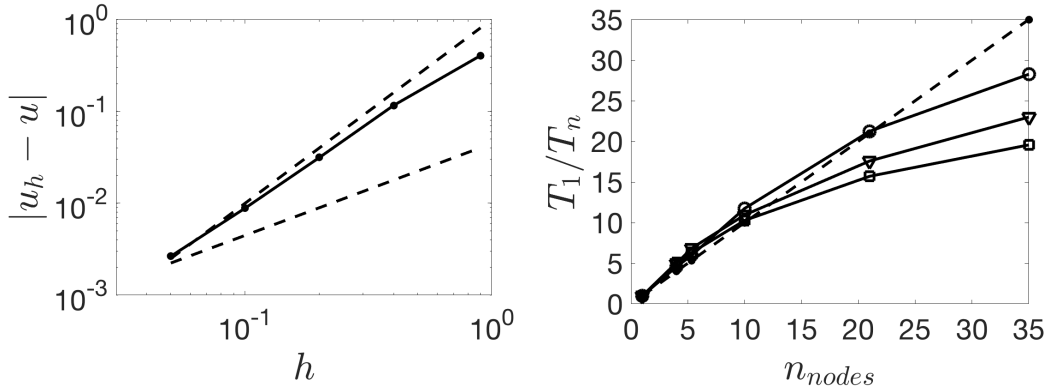


(a) (b)

Figure 2.2: (a) Spatial accuracy of the finite volume code. The dashed lines represents the first and second order accuracy, while the solid line is the accuracy of our finite volume code. (b) Scalability of the finite volume code. The dashed line represents the reference linear value, while the solid lines are the speed-up of our code ( ○ $nj = 194$; ▽ $nj = 388$; □ $nj = 776$).

The discrete counterparts of equations (2.1) have been implemented in a well-established curvilinear finite volume code (Omidyeganeh and Piomelli, 2013a,b,

Rosti, 2016) written in Fortran 77. As previously mentioned, the code approximates the fluxes using a second-order central formulation (Figure 2.2a), and the method proposed by Rhie and Chow (1983) to avoid the pressure spurious oscillations. The equations are advanced in time using a second-order semi-implicit fractional-step procedure (Kim and Moin, 1985), where the implicit Crank-Nicolson scheme is implemented for the wall-normal diffusive terms while an explicit Adams-Bashforth scheme is applied to the other terms. The Poisson's pressure equation, that needs to be solved at each time step to enforce the solenoidal condition of the velocity field, is transformed into a series of two-dimensional Helmholtz equations in the wavenumber space via a Fast Fourier Transform (FFT) in the spanwise direction. Each of the resultant elliptic $2D$ problem is then solved using a preconditioned Krylov method (usign the PETSc library implementation, Balay et al., 2017). In particular, we have found the iterative Biconjugate Gradient Stabilized (BiCGStab) method with an algebraic multigrid preconditioner (boomerAMG, Yang et al., 2002) to behave quite efficiently. The code is parallelised using the domain decomposition technique and the message passing interface (MPI) library. Figure 2.2b shows the strong scaling of the code, defined as the ratio between the time needed to perform one time-step with one processor $T_1$ and the time using $n$ processors $T_n$, carried out on the ARCHER platform. This test has been produced with a series of channel flow simulations at friction Reynolds number, based on the mean wall-shear velocity and the channel half height, $Re_\tau = 1000$. The test was performed on a Cartesian grid with $10080 \times nj \times 16$ points in the $x$, $y$ and $z$ directions respectively. Different series have been produced varying the number of points in the wall-normal direction, $nj$. For every series (solid lines with symbols), the problem size has then been kept fixed while increasing the computing nodes up to 35 (each node has 24 CPUs). The dashed line shows the ideal strong scaling. The solid lines overcome the ideal scaling for lower number of nodes. This effect is caused by the nonlinearity of the memory (and cache) available increasing the number of nodes.

### 2.1.3 Turbulent channel flow

We consider the flow of an incompressible viscous fluid through a channel with smooth, impermeable walls, as sketched in Figure 2.3. We introduce the Cartesian coordinate system shown in Figure 2.3, where $x$, $y$ and $z$ denote the streamwise, wall-normal and spanwise coordinates, while $u$, $v$ and $w$ denote the respective components of the velocity vector field. The lower and upper walls are placed at a distance $L_y = 2H$ and are located at $y = 0$ and $y = 2H$, respectively. At the walls, a no-slip condition is imposed. It is assumed that the fully developed turbulent channel flow is homogeneous in the streamwise and spanwise directions, so that periodic boundary conditions can be used in these directions. The use of

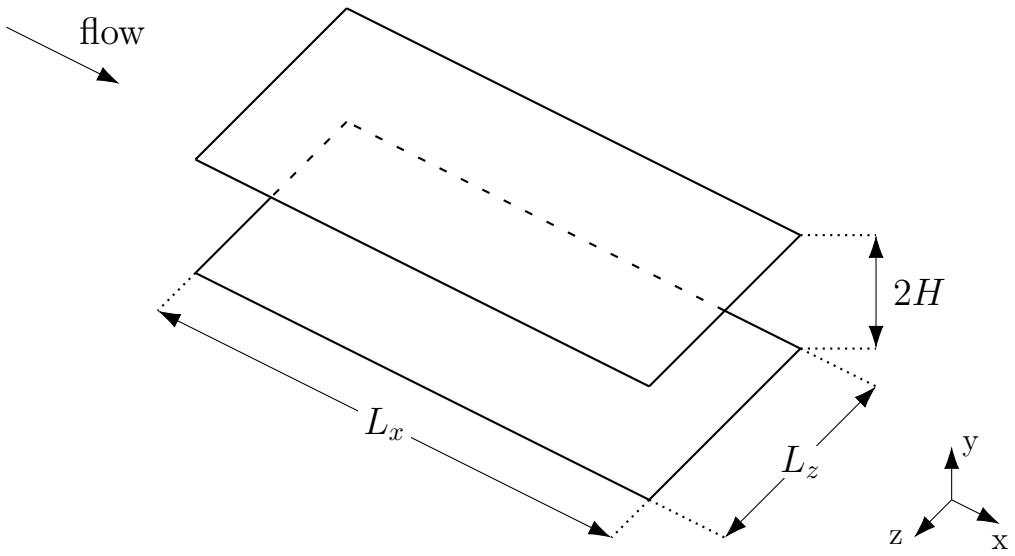


Figure 2.3: Sketch of the channel geometry.

the periodic boundary condition can be justified if the computational box is long and large enough to include the largest eddies in the flow (Kim et al., 1987).

In order to write the problem in a dimensionless form, we select the channel semi-height as characteristic length,

$$L^\star = H, \tag{2.30}$$

and the bulk velocity as characteristic velocity,

$$U^\star = U_b = \frac{1}{2H} \int_0^{2H} \langle u \rangle (y) \ \mathrm{d}y, \tag{2.31}$$

where $\langle u \rangle (y)$ is the mean velocity in the streamwise direction and the $\langle \cdot \rangle$ indicates the average over both time and homogeneous directions, $x$ and $z$. With this choice, the Reynolds number is defined as

$$Re_b = \frac{U_b H}{\nu}, \tag{2.32}$$

where $\nu$ is the kinematic viscosity defined as $\nu = \mu/\rho$.

To validate the value of the code used, we select a typical channel flow simulation at $Re_b = 2800$ and we compare our results with the ones in the well-known, seminal paper by Moser et al. (1999). The simulation is carried out on a computational grid of $256 \times 192 \times 192$ points, in the $x$, $y$ and $z$ directions respectively. The computational domain size is set to $2\pi H \times 2H \times \pi H$ in the $x$, $y$ ans $z$ directions. The mesh in the nonhomogeneous direction $y$ has been generated with

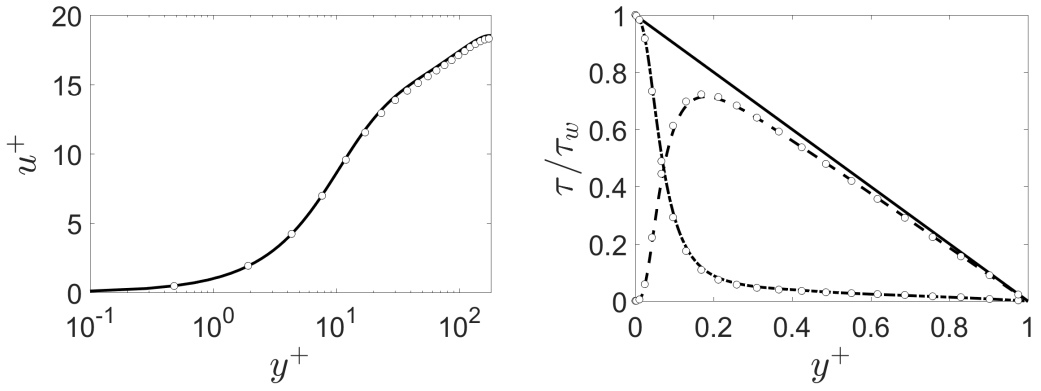


(a) (b)

Figure 2.4: (a) Mean velocity profile in wall units. (b) The total shear stress (solid line), decomposed in the viscous stress (dash-dotted line) and Reynolds shear stress (dashed line) obtained from the simulation. The circles in both the plots are used for the results by Moser et al. (1999).

the stretching function,

$$y = \frac{\tanh(a\overline{y})}{a}, \tag{2.33}$$

where $a$ is an adjustable parameter used to modify the mesh deformation, and $\overline{y}$ is a mesh grid with constant spacing coming from the lower to the upper wall.

With the mentioned grid, the resolution turns out to be $\Delta x^+ \approx 5$ in wall units in the streamwise direction, $\Delta z^+ \approx 3$ in the spanwise direction, and with a minimum $\Delta y^+$ in the wall-normal direction which is less than 1. The wall units, indicated by the superscript $\cdot^+$, are measured in terms of the viscous length $\delta_\nu$, which is defined as follows

$$\delta_\nu = \frac{\nu}{u_\tau}, \tag{2.34}$$

where $u_\tau$ is the friction velocity that, in a turbulent channel flow with solid walls, is defined as follows

$$u_\tau = \sqrt{\nu \left.\frac{\mathrm{d}\langle u\rangle}{\mathrm{d}y}\right|_{y=0}}, \tag{2.35}$$

where $y/H = 0$ is the location of the wall. Note that the viscous length and the friction velocity as reference length and velocity scale, respectively, are used in the near-wall regions.

The Reynolds number based on the friction velocity $u_\tau$ and the channel semi-height is called friction Reynolds number $Re_\tau$, and is defined as $Re_\tau = u_\tau H/\nu$. In our case, with the choice of $Re_b = 2800$, the friction Reynolds number is $Re_\tau = 180$.

Figure 2.4a shows the mean velocity profiles $u^+ = u/u_\tau$ versus the logarithm of the distance from the wall expressed in wall units. The solid line is used for the results of our simulation, while the circles for the reference values of Moser et al. (1999). The agreement is very good, even if our friction velocity is slightly underestimated.

The total shear stress, $\tau$, defined as the sum of the Reynolds shear stress with the viscous stress

$$\tau = \mu \frac{\mathrm{d}\langle u \rangle}{\mathrm{d}y} - \rho \langle u'v' \rangle. \tag{2.36}$$

is given in Figure 2.4b, compared with the results by Moser et al. (1999). As for the mean velocity profile, the agreement between our simulation and the reference data is very good.

The next section will introduce the immersed boundary method which is the technique that has been chosen to deal with the presence of complex and/or moving portions of the boundary.

## 2.2 Immersed Boundary Method

The Immersed Boundary Method (IBM) is a numerical technique able to simulate fluid flows around moving or deforming bodies with complex surface geometry without requiring a computational grid that conforms to the immersed-body geometry itself. The pioneer of this numerical technique has been Charles Peskin who, back in the seventies, was able to simulate the blood flow around the natural mitral valve in a human heart (Peskin, 1972). As mentioned, the key feature of this method is that the numerical grid is not required to conform to the geometry of the object, which is replaced by an appropriate body force distribution $\boldsymbol{f}$ that mimics the effect of the body on the fluid by restoring the desired velocity boundary values on its immersed surface at every time step.

This technique has drawbacks and advantages that need to be considered. Concerning the former, surely the imposition of the right boundary conditions is not straightforward and the impact of the method on the accuracy and conservation properties of the numerical scheme is not obvious. Moreover, a body-fitted grid would allow a better control on the grid resolution close to the boundary of the body. Despite this, the advantages of the IBM become huge when dealing with complex surfaces or moving bodies. In fact, with complex surfaces, the primary advantage brought by the IBM is the simplification of the grid generation process that could be burdensome. When it comes to moving bodies, the computational cost of regenerating the grid at every time step would significantly impact the overall computational cost. Moreover, the IBM allows keeping a Cartesian grid that has a significant lower computational cost per grid-point compared with a curvilinear, body-shaped grid (Mittal and Iaccarino, 2005). Many IBMs were

proposed in the past (a detailed overview can be found in Mittal and Iaccarino, 2005). The main difference between the methods is related with the way in which the aforementioned body force distribution is computed. IBMs can be grouped in two main categories, the continuous and discrete forcing ones. In the first approach the forcing is incorporated into the continuous equations before discretisation, whereas in the second approach the forcing is introduced after the equations are discretised. The method used in this thesis, developed by Pinelli et al. (2010), belongs to the first group and is based on the Reproducing Kernel Particle Method (RKPM) (Liu et al., 1996, 1995).

Next, we explain how the equations are modified to take into account the presence of an immersed body when using the RKPM approach. Firstly, the surface $\Gamma$ of the immersed surface delimiting the body is discretised using $N$ markers, called Lagrangian points $\boldsymbol{X}$. These points, in general, do not correspond with the grid nodes $\boldsymbol{x}$.

The discrete equations are then modified in order to accomplish the presence of the immersed body by introducing the body force distribution, as mentioned above. The surface that delimits the immersed body is discretised with a *Lagrangian grid* using $N$ markers that, in general, do not conform with the underlying domain grid (*Eulerian grid*). To advance in time the Navier-Stokes equations, firstly, a simple prediction step (2.22) is performed, without taking into account the presence of the immersed object. To compute the velocity onto the embedded geometry , $\boldsymbol{U}^*$, an interpolation operator, $\mathcal{I}$, is applied to the surrounding Eulerian grid points with corresponding velocity $\boldsymbol{u}^*$,

$$\boldsymbol{U}^* = \mathcal{I}\left(\boldsymbol{u}^*\right). \tag{2.37}$$

The values of $\boldsymbol{U}^*$ are then used to determine a distribution of singular forces along $\Gamma$ that restore the prescribed boundary values $\boldsymbol{U}^\Gamma$ as

$$\boldsymbol{F}^* = \frac{\boldsymbol{U}^\Gamma - \boldsymbol{U}^*}{\Delta t}. \tag{2.38}$$

The force field defined over $\Gamma$ is transformed into a body force distribution applied to the fluid grid using a convolution operator, $\mathcal{C}$,

$$\boldsymbol{f}^* = \mathcal{C}\left(\boldsymbol{F}^*\right). \tag{2.39}$$

Then, the prediction step of the momentum equation is repeated adding the computed volume force field as a source term,

$$\frac{\boldsymbol{u}^* - \boldsymbol{u}^n}{\Delta t} = -\mathcal{N}_l\left(\boldsymbol{u}^n, \boldsymbol{u}^{n-1}\right) + \frac{1}{Re}\mathcal{L}\left(\boldsymbol{u}^*, \boldsymbol{u}^n\right) - \mathcal{G}\left(\phi^n\right) + \boldsymbol{f}^*, \tag{2.40}$$

and a new predicted, nonsolenoidal velocity field $\boldsymbol{u}^*$ is computed. Finally, the

time advancement step can be completed with the usual solution of the pressure Poisson's equation and the predicted velocity field is projected onto a divergence-free space. The given procedure is common to a number of IB methods. The peculiarity of the present method concerns the way in which the operators $\mathcal{I}$ and $\mathcal{C}$ are built.

### 2.2.1 Interpolation and convolution

We use the Reproducing Kernel Particle Method (RKPM) (Liu et al., 1996, 1995, Pinelli et al., 2010, Zhang et al., 2004) to define the interpolation and spreading operators. In this method, the approximation $f_a(x)$ of the value of a given smooth function at point $x \in \Omega$ can be expressed as a *kernel* approximation,

$$f_a(x) = \int_\Omega w_\delta(x - s) f(s) \, ds, \tag{2.41}$$

where $w_\delta$ is a non-negative kernel function with compact support, and the subscript indicates the dependence of the kernel function on a parameter $\delta$, called dilation parameter. The latter determines the dimension of the support, $\Omega_I$. Hence, $w_\delta$ is nonzero only in a subdomain $\Omega_I$ of $\Omega$ and zero elsewhere, i.e. in $\Omega_I \setminus \Omega$. It is worth noticing from (2.41) that, if the kernel is the Dirac delta function, then $f_a(x) = f(x)$ and the considered function $f$ is exactly reproduced. Roma et al. (1999) proposed a discrete approximation of the kernel function,

$$w_\delta(r) = \begin{cases} \dfrac{1}{6}\left(5 - 3|r| - \sqrt{-3\left(1 - |r|\right)^2 + 1}\right), & \text{if } 0.5 \le |r| \le 1.5, \\ \dfrac{1}{3}\left(1 + \sqrt{-3r^2 + 1}\right), & \text{if } |r| \le 0.5, \\ 0, & \text{otherwise,} \end{cases} \tag{2.42}$$

with $r = (x - s)/\delta$ (see Figure 2.5a), that satisfies the following properties:

1. $w_\delta(r)$ is continuous;
2. $w_\delta(r) = 0$ if $|r| > 1.5$;
3. $\sum_l w_\delta(r - l) = 1$;
4. $\sum_l (r - l) w_\delta(r - l) = 0$;
5. $\sum_l \left[w_\delta(r - l)\right]^2 = 1/2$.

The latter is valid $\forall r \in \mathbb{R}$ and $\forall l \in \mathbb{Z}$. Figure 2.5a shows the function $w_\delta$ and its discrete counterpart (represented with dots in the figure), considering $r = 0.0$. The discrete kernel function is not null only for $l = -1, 0, 1$.

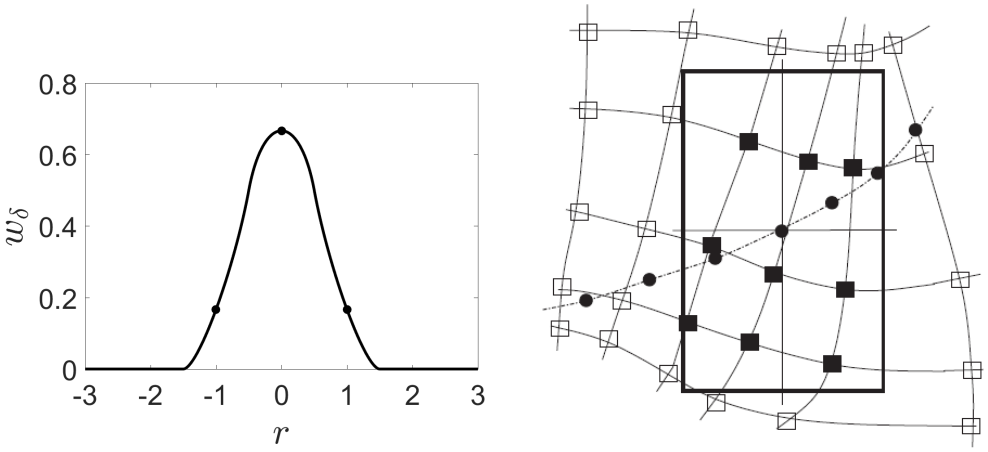


(a) (b)

Figure 2.5: (a) Kernel function proposed by Roma et al. (1999). (b) Taken from Pinelli et al. (2010). The black rectangle is the cage around one of the Lagrangian points, shown as dots. The squares represents grid points, and the black ones are the grid points falling within the cage.

Since the previous properties involve the natural number $l$, they can be satisfied by a function interpolated using equation (2.41) and equation (2.42) only if the nodes are equispaced. To extend this approach to a nonuniform lattice, following Liu et al. (1995) and Pinelli et al. (2010), we use a modified window function $\widetilde{w}_\delta$, defined as

$$\widetilde{w}_\delta\left(x-s\right)=\sum_{i=0}^{n} b_i\left(x-s\right)^i w_\delta\left(x-s\right), \tag{2.43}$$

where $b_i$ are $n+1$ coefficients determined by imposing the continuous equivalent of properties 3 and 4,

$$\widetilde{m}_i\left(x\right)=\int_\Omega \left(x-s\right)^i \widetilde{w}_\delta\left(x-s\right) ds=\delta_{i0} \qquad \text{for } i=0,1,\ldots,n \tag{2.44}$$

where $\delta_{ij}$ is the Kronecker's delta. Note that these conditions imply the exact representation of the elements of the canonical polynomial base $\{1, x, x^2, \ldots\}$. The number $n$ is the higher order of the polynomial that we want to represent exactly. For example, $n=2$ would lead to an exact representation of all polynomials of

degree up to 2. Substituting equation (2.43) into equation (2.44), we obtain

$$\widetilde{m}_i(x) = \int_\Omega (x-s)^i \, \widetilde{w}_\delta(x-s)\, ds = \sum_{j=0}^{n} b_j m_{i+j}(x) = \delta_{i0}, \tag{2.45}$$

for $i = 0, 1, \ldots, n$, where we have defined

$$m_i(x) = \int_\Omega (x-s)^i \, w_\delta(x-s)\, ds. \tag{2.46}$$

The equations (2.45) form a symmetric linear system $M\vec{b} = \vec{e}_1$, where the right hand side $\vec{e}_1$ is a vector, whose elements are all zeros, except the first one which is equal to 1. From the solution of this linear system (2.45), we can obtain the coefficients $b_i$ and, finally, we can write the corrected window function (here given for $n = 2$) as

$$\widetilde{w}_\delta(x-s) = \left[b_o + (x-s)\, b_1 + (x-s)^2 \, b_2\right] w_\delta(x-s). \tag{2.47}$$

The procedure can be extended to higher dimensions, defining the window function as a Cartesian product of the $1D$ kernels. In $2D$, it becomes

$$w_{\delta,\eta}(x-s, y-t) = w_\delta(x-s)\, w_\eta(y-t) \tag{2.48}$$

and in $3D$

$$w_{\delta,\eta,\sigma}(x-s, y-t, z-v) = w_\delta(x-s)\, w_\eta(y-t)\, w_\sigma(z-v), \tag{2.49}$$

where $\delta$, $\eta$ and $\sigma$ are the dilatation parameters in the coordinate directions. The linear systems to find the coefficients $b_{i,j}$ and $b_{i,j,k}$ are obtained from the following conditions

$$\widetilde{m}_{i,j} = \int_\Omega (x-s)^i (y-t)^j \, \widetilde{w}_{\delta,\eta} ds = \delta_{l0} \qquad \text{for } i, j = 0, 1, \ldots, n, \tag{2.50}$$

in $2D$, where $l = i + j$ and $i + j \leq n$, and

$$\widetilde{m}_{i,j,k} = \int_\Omega (x-s)^i (y-t)^j (z-v)^k \, \widetilde{w}_{\delta,\eta,\sigma} ds = \delta_{l0} \qquad \text{for } i, j, k = 0, 1, \ldots, n, \tag{2.51}$$

in $3D$, where $l = i + j + k$ and $i + j + k \leq n$. So, the corrected window functions

in $2D$ and $3D$ are

$$\begin{aligned}\widetilde{w}_{\delta,\eta}\left(x-s,y-t\right)=&\left[b_{0,0}+\left(x-s\right)b_{1,0}+\left(y-t\right)b_{0,1}+\right.\\&\left(x-s\right)\left(y-t\right)b_{1,1}+\left(x-s\right)^{2}b_{2,0}+\left(y-t\right)^{2}b_{0,2}\left.\right]\times\\&w_{\delta,\eta}\left(x-s,y-t\right),\end{aligned}\tag{2.52}$$

and

$$\begin{aligned}\widetilde{w}_{\delta,\eta,\sigma}\left(x-s,y-t,z-v\right)=&\left[b_{0,0,0}+\left(x-s\right)b_{1,0,0}+\left(y-t\right)b_{0,1,0}+\left(z-v\right)b_{0,0,1}+\right.\\&\left(x-s\right)\left(y-t\right)b_{1,1,0}+\left(y-t\right)\left(z-v\right)b_{0,1,1}+\left(z-v\right)\left(x-s\right)b_{1,0,1}+\\&\left(x-s\right)^{2}b_{2,0,0}+\left(y-t\right)^{2}b_{0,2,0}+\left(z-v\right)^{2}b_{0,0,2}\left.\right]\times\\&w_{\delta,\eta,\sigma}\left(x-s,y-t,z-v\right),\end{aligned}\tag{2.53}$$

respectively.

Finally, we briefly describe the implementation of the IB based on RKPM. Around every node belonging to the Lagrangian lattice, $\boldsymbol{X}$, we define a cage that contains at least three nodes of the underlying Eulerian mesh in every direction, as shown in Figure 2.5b, whose edges measure $3\delta$, $3\eta$ and $3\sigma$ in $x$, $y$ and $z$, respectively, as suggested by equation (2.42). Once the Eulerian nodes that fall within the cage have been defined, the terms of the moments matrix (the $3D$ version of (2.46)) can be numerically evaluated to assemble the local window function, using the mid-point quadrature rule. The coefficients $\vec{b}$ of the correction polynomials are found by solving the symmetric linear system $M\vec{b}=\vec{e}_1$ for every Lagrangian point. Due to the very low values that the window function may take at the nodes close to the boundary of the cage, the moment matrix may become ill conditioned. This problem is avoided by rescaling the linear system, and solving the equivalent one $HMH^{-1}\vec{b}=\vec{e}_1$, where the diagonal matrix $H$ has the inverse of the dilation factors in the main diagonal. In $3D$, $H$ can be written as

$$H=\operatorname{diag}\left(1,\frac{1}{\delta},\frac{1}{\eta},\frac{1}{\sigma},\frac{1}{\delta\eta},\frac{1}{\eta\sigma},\frac{1}{\delta\sigma},\frac{1}{\delta^{2}},\frac{1}{\eta^{2}},\frac{1}{\sigma^{2}}\right).\tag{2.54}$$

Once the coefficients $\vec{b}$ have been computed, the window function, $\widetilde{w}_{\delta,\eta,\sigma}$, can be used for the interpolation (2.37) and spreading (2.39) operations. In particular, the discrete interpolation, using the midpoint rule, becomes

$$U_l=\mathcal{I}\left(u_{i,j,k}\right)=\sum_{i,j,k\in\Omega_I}u_{i,j,k}\tilde{w}_{\delta,\eta,\sigma}\left(x_{i,j,k}-X_l\right)\Delta V_{i,j,k},\tag{2.55}$$

while the spreading operation reads as

$$f_{i,j,k} = \mathcal{C}\left(F_l\right) = \sum_{l=1}^{N} F_l \tilde{w}_{\delta,\eta,\sigma}\left(x_{i,j,k} - X_l\right) \epsilon_l, \tag{2.56}$$

where $\epsilon_l$ is a characteristic volume related to the local dilation coefficients of the window function. To determine the correct value of $\epsilon$, first, we consider the value of the force on the Lagrangian points, obtained by interpolation,

$$F_l = \sum_{i,j,k \in \Omega_I} f_{i,j,k} \tilde{w}_{\delta,\eta,\sigma}\left(x_{i,j,k} - X_l\right) \Delta V_{i,j,k}, \tag{2.57}$$

then, we replace $f_{i,j,k}$ with (2.56), thus obtaining

$$F_l = \sum_{i,j,k \in \Omega_I} \left[ \sum_{m=1}^{N} F_m \tilde{w}_{\delta,\eta,\sigma}\left(x_{i,j,k} - X_m\right) \epsilon_m \right] \tilde{w}_{\delta,\eta,\sigma}\left(x_{i,j,k} - X_l\right) \Delta V_{i,j,k}. \tag{2.58}$$

The linear system (2.58) can be written, using a matrix notation, as

$$A \operatorname{diag}\left(\vec{\epsilon}\right) \vec{F} = \vec{F}. \tag{2.59}$$

By requiring that $\vec{\epsilon}$ is independent of the actual force distribution, we obtain the constraint $\det\left[A \operatorname{diag}\left(\vec{\epsilon}\right) - I\right] = 0$, whose solution is found by solving

$$A\vec{\epsilon} = \vec{1}, \tag{2.60}$$

where $\vec{1}$ is a vector of ones. As shown by Pinelli et al. (2010), the conditioning of the matrix $A$ depends on the ratios between the distances of the Lagrangian nodes and the local grid size. When the Lagrangian spacing is approximately equal to the local grid size (or slightly higher), the linear system for $\vec{\epsilon}$ is well conditioned and is easily solved.

### 2.2.2 Flow around a cylinder

The validation of the RKPM immersed boundary implementation is done by simulating the flow of an incompressible viscous fluid around a circular cylinder, as sketched in Figure 2.6. We introduce the Cartesian coordinate system shown in Figure 2.6, where $x$ and $y$ denote the streamwise and normal coordinates, while $u$ and $v$ denote the respective components of the velocity vector field. On the

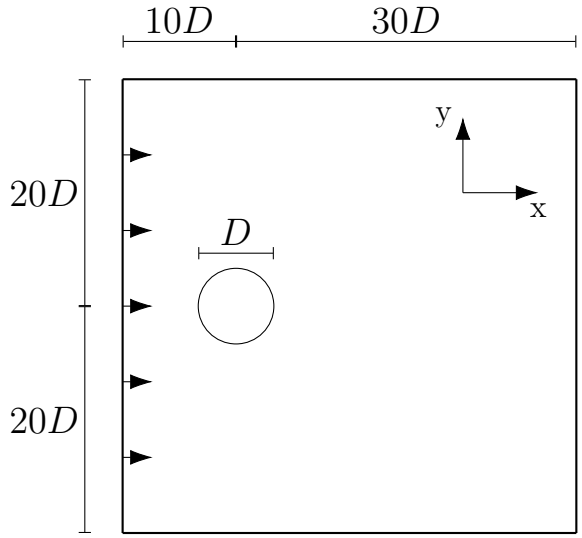


Figure 2.6: Sketch of the computational domain around a cylinder.

lower and upper surfaces, we impose the free slip condition, i.e.

$$\frac{\partial u_i}{\partial y} = 0; \qquad v = 0, \tag{2.61}$$

while the no-slip condition is imposed on the body surface. At the inlet, a uniform velocity in the streamwise direction, $U_\infty$, is imposed, while a convective outflow condition, computed using

$$\frac{\partial \boldsymbol{u}}{\partial t} + (\boldsymbol{u_{old}} \cdot \boldsymbol{\nabla})\, \boldsymbol{u} = 0, \tag{2.62}$$

where $\boldsymbol{u}_{old}$ is the velocity computed at the previous time-step, is enforced at the outlet. The problem is made dimensionless by using the cylinder diameter as characteristic length,

$$L^* = D, \tag{2.63}$$

and the free-stream velocity as characteristic velocity,

$$U^* = U_\infty. \tag{2.64}$$

Consistently, the Reynolds number is defined as

$$Re_D = \frac{U_\infty D}{\nu}. \tag{2.65}$$

We fixed the Reynolds number to $Re_D = 100$. The simulation is is carried out on a lattice of $672 \times 671$ points, that spans a computational domain of $40D \times 40D$.

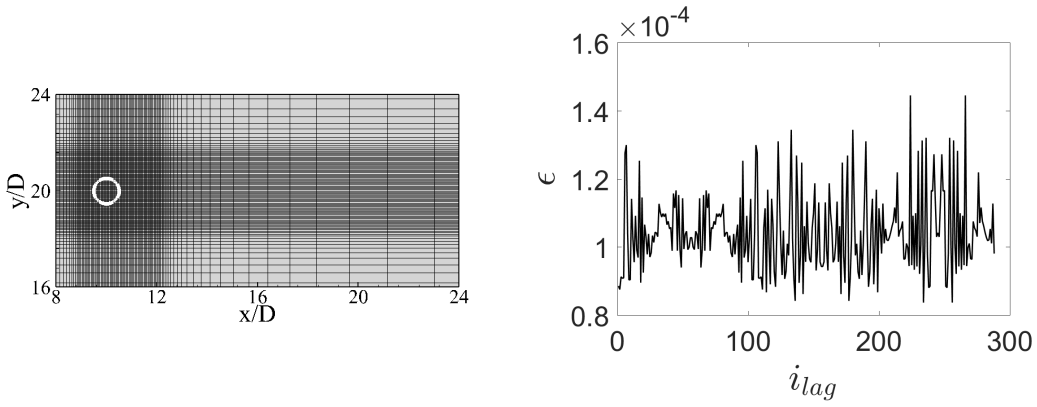


(a) (b)

Figure 2.7: (a) Grid in the proximity of the cylinder (nodes are plotted with a skip index of 5). (b) The values of $\epsilon$ (2.60) for every Lagrangian point.

The centre of the cylinder is at $(10D, 20D)$, and its surface is discretised with 288 equispaced Lagrangian points. In the region inside and surrounding the cylinder, the mesh is uniform with a spacing of $0.0084D$ and stretches towards the boundaries of the domain, as shown in Figure 2.7a. Figure 2.7b reports the values of $\epsilon$ (2.60) computed for every Lagrangian point. Note that the square root of the average value $0.0102D$ is close to the mesh spacing.

Figure 2.8a shows the instantaneous contours of the spanwise vorticity, $\omega_z$, around the cylinder. At this Reynolds number, the wake of the cylinder is characterised by the von Kármán vortex street typical of bluff bodies. Vortices of opposite sign are shed from the cylinder periodically, at a Strouhal number equal to $S_t = f_s D/U_\infty = 0.17$, which is close to the experimental value of $S_t = 0.165$ reported by Williamson (1996). The value was obtained by the spectrum of the instantaneous lift coefficient value, $C_L = 2L/(\rho U_\infty^2 D)$ (where $L$ is the lift per unit length), whose time history is reported in Figure 2.8b with a solid line together with the drag coefficient, $C_D = 2D_r/(\rho U_\infty^2 D)$ (where $D_r$ is the drag per unit length), shown with a dashed line. The mean lift and drag coefficients are $C_L = 0.0$ and $C_D = 1.35$, respectively. The maximum absolute lift value is $C_L^{max} = 0.33$. These results show good agreement with the ones obtained by Guilmineau and Queutey (2002), who found a mean drag coefficient $C_D = 1.35$, and a maximum lift equal to $C_L^{max} = 0.36$ using an O-type structured grid, with a mesh built using 120 points in the angular direction and 100 points in the radial direction. The first points of the mesh in the fluid are located at $y = 0.001D$ away from the cylinder wall.

Table 2.1 reports the mean drag coefficients $C_D$ and the maximum instantaneous lift coefficients $C_L^{max}$ obtained from various simulations, changing the

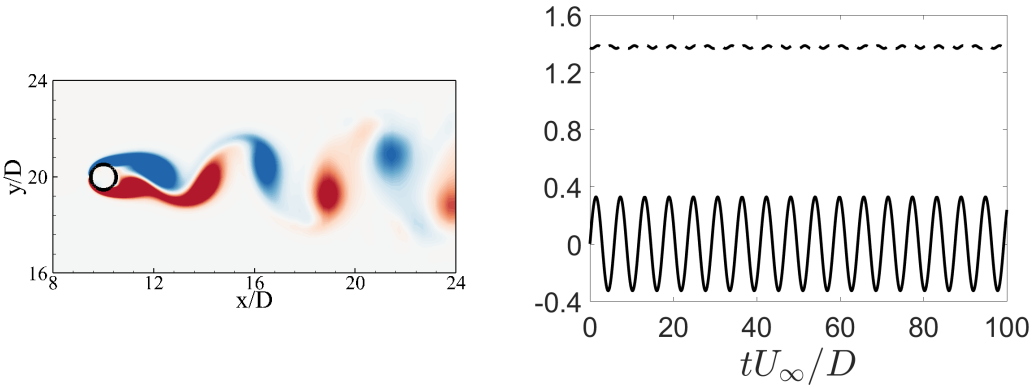


(a) (b)

Figure 2.8: (a) Contours of the spanwise vorticity $\omega_z$. (b) Evolution of the lift $C_L$ (solid line) and drag coefficients $C_D$ (dashed line) over time.

Table 2.1: Aerodynamic coefficients for the cylinder simulations campaign. The data of the reference case shown in the first row are taken from Guilmineau and Queutey (2002).

| Case | $N$ | $C_L^{max}$ | $C_D$ |
|---|---|---|---|
| Ref. | – | 0.36 | 1.35 |
| Cyl-1 | 96 | 0.35 | 1.52 |
| Cyl-2 | 144 | 0.35 | 1.43 |
| Cyl-3 | 216 | 0.35 | 1.39 |
| Cyl-4 | 288 | 0.33 | 1.35 |
| Cyl-5 | 320 | 0.33 | 1.35 |

number of Lagrangian points used to represent the cylinder surface. We notice that the cases with 288 and 320 points have the same values, meaning that 288 points are enough to correctly represent the solid cylinder at this Reynolds number.

Figure 2.9a shows the contours of the instantaneous streamwise velocity around the cylinder. In Figure 2.9b the $u$ and $v$ velocity profiles on a vertical line passing through the centre of the cylinder at $x = 10D$ are reported using solid and dashed lines, respectively. Both the velocity components have values close to 0 at the cylinder boundary. The symbols represent the points of the mesh, showing the density of the mesh in the cylinder region.

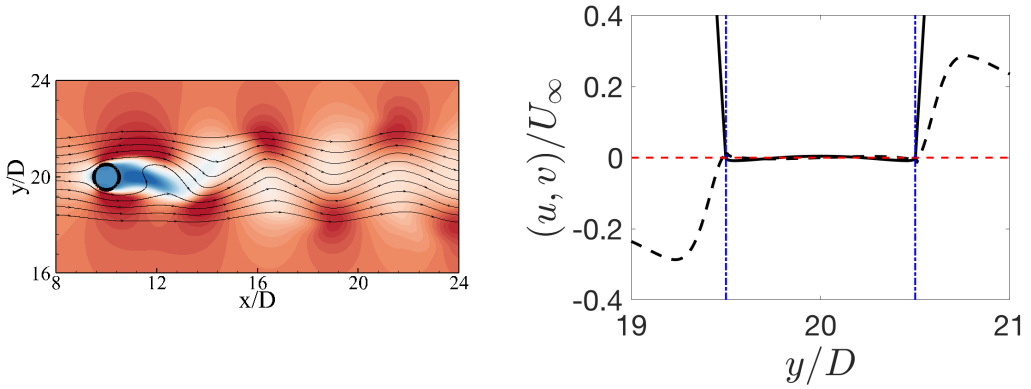


(a) (b)

Figure 2.9: (a) Contours of the streamwise velocity $u/U_\infty$. (b) $u/U_\infty$ (solid line) and $v/U_\infty$ (dashed line) velocity profiles at $x = 10D$. The red dashed line represents the zero velocity line, while the blue dash-dotted lines mark the boundaries of the cylinder.

## 2.3 Flow above a rigid canopy

We now briefly describe the numerical set-up that has been used as a common ground to simulate the flow above an infinite rigid canopy composed of resolved filamentous elements. In order to be able to correctly simulate this flow, avoiding very costly simulations that would have taken very long time, we used a Large-Eddy Simulation (LES) approach. The computational cost is lowered by reducing the computational grid that would be necessary to catch the right dissipation induced, for instance, by the wakes behind the canopy elements as the Reynolds number is increased. In order to include this contribution and make sure that the dissipation introduced in the flow field is enough, we need to add an unresolved subgrid stress tensor to the Navier-Stokes momentum equation. In this section, in particular, we will introduce the closure model used to deal with the subgrid stress tensor for the LES, the grid and the boundary conditions. This section terminates with the description of test cases used to verify and to validate the numerical implementation.

### 2.3.1 Numerical set-up

We now consider an incompressible three-dimensional unsteady flow field in an open channel, with infinite streamwise and spanwise dimensions, above a rigid canopy. The computational domain is shown in Figure 2.10. In the LES approach, the governing equation are obtained by filtering out the smallest length-scales from the velocity and pressure fields (Leonard, 1975). Thus, in a Cartesian

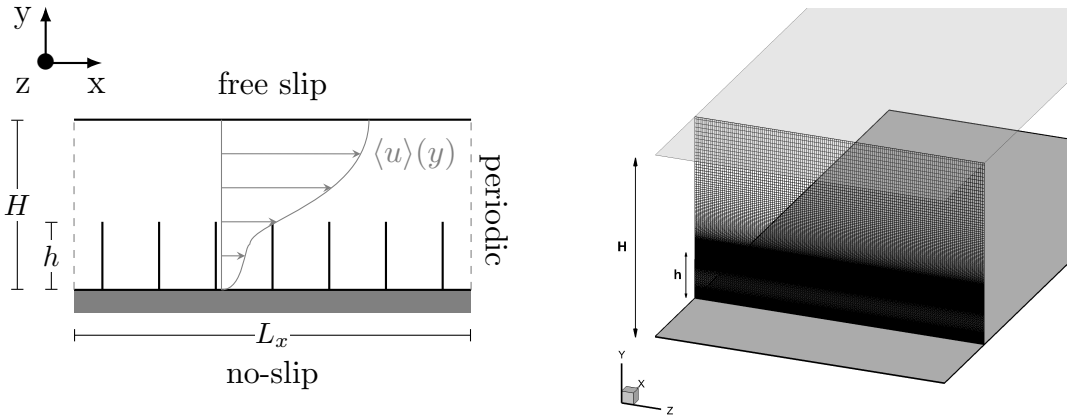


Figure 2.10: Sketch of the computational domain (on the left) with the emphasis on the mesh in the wall-normal direction (on the right).

reference frame – being $x_1$, $x_2$ and $x_3$ ($u_1$, $u_2$ and $u_3$) the streamwise, wall-normal and spanwise directions (velocities) respectively, also referred to $x$, $y$ and $z$ ($u$, $v$ and $w$) – the dimensionless equations for the resolved fields are

$$\begin{aligned} \frac{\partial \overline{u}_i}{\partial t} + \overline{u}_j \frac{\partial \overline{u}_i}{\partial x_j} &= -\frac{\partial \overline{P}}{\partial x_i} + \frac{1}{Re_b} \frac{\partial^2 \overline{u}_i}{\partial x_j \partial x_j} + \frac{\partial \tau_{ij}}{\partial x_j} + f_i, \\ \frac{\partial \overline{u}_i}{\partial x_i} &= 0, \end{aligned} \tag{2.66}$$

where $Re_b$ is the Reynolds number based on the flow depth $H$ and the bulk velocity,

$$U_b = \int_0^H \langle u \rangle \, \mathrm{d}y, \tag{2.67}$$

being $\nu$ the kinematic viscosity. The symbols $\overline{\cdot}$ represents the resolved field. The unresolved, subgrid stress tensor, $\tau_{ij} = \overline{u_i u_j} - \overline{u}_i \overline{u}_j$, comes from the drainage of momentum by the unresolved small scales over the resolved ones. To close the set (2.66), $\tau_{ij}$ is modelled using an eddy-viscosity assumption

$$\tau_{ij} - \delta_{ij} \tau_{kk}/3 = -2\nu_t \overline{S}_{ij} \tag{2.68}$$

where $\nu_t$ is the subgrid eddy-viscosity, $\overline{S}_{ij} = (\partial \overline{u}_i / \partial x_j + \partial \overline{u}_j / \partial x_i)/2$ is the resolved strain-rate tensor. The subgrid eddy-viscosity is modelled using the Integral Length-Scale Approximation (ILSA) model described in Piomelli et al. (2015) and Rouhi et al. (2016), which consists of a grid-independent spatial filtering operation.

The computational domain is meshed with uniform spacings in the homoge-

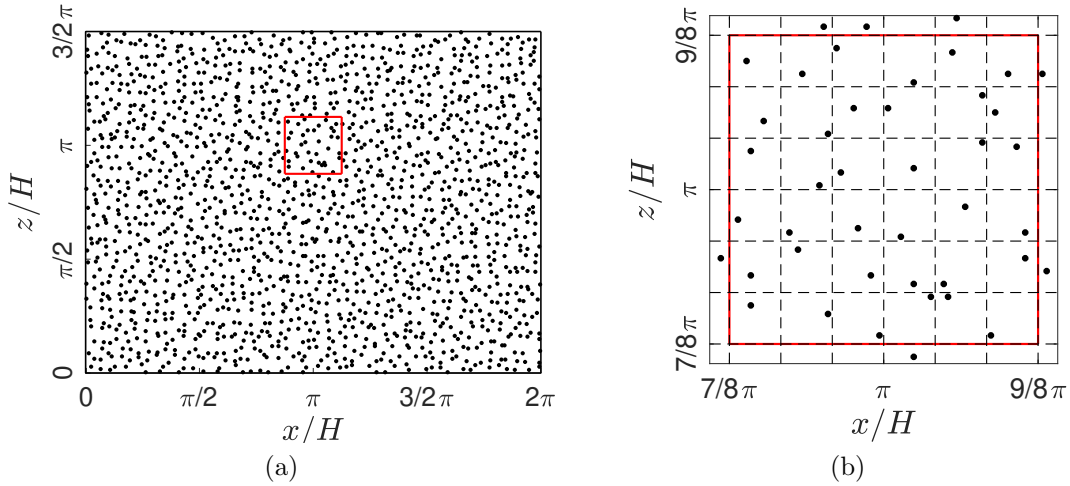


Figure 2.11: Panel (a) Computational domain with the filaments distribution: wall-parallel view. The red box is zoomed out in panel (b), where the random allocation of each filament into its own tile of size $\Delta S \times \Delta S$ is highlighted.

neous directions and with a stretched grid in wall-normal direction to capture the right shear in the region of a very high velocity gradient (see Figure 2.10). The canopy elements are resolved directly introducing a set of rigid and solid filaments of finite cross-section, related to the local grid size, which are placed perpendicularly to the horizontal wall. To impose the boundary conditions that each rigid filament exerts on the fluid (i.e., zero velocity) we have used the IBM described in §2.2.

The domain has been divided into tiles of area $\Delta S^2$ and a single filament has been placed with a random uniform distribution in each tile (see Figure 2.11). The tile size ($\Delta S$) and the filament height $h$ have been chosen in order to design the canopy configuration needed, based on the solidity $\lambda = d\,h/\Delta S^2$ (Nepf, 2012a, see also Figure 1.2). The random distribution of the filaments into each tile has been selected in order to avoid the introduction of any particular momentum increase or decrease into the canopy layer due to the blockage effect introduced by the filaments.

The simulations have been carried out on a periodic box in the streamwise (i.e. $x$) and spanwise (i.e. $z$) directions. The choice of selecting a streamwise periodic condition has been motivated by the experiments of Ghisalberti and Nepf (2004). Although they observed the presence of a mixing-layer developing at the canopy edge, they also suggested that its thickness was independent of the streamwise location, meeting the conditions required by periodic boundaries. At the bottom wall, a no-slip boundary condition is imposed while a free slip condition, i.e. (2.61), is set at the top surface (see Figure 2.10). The simulations

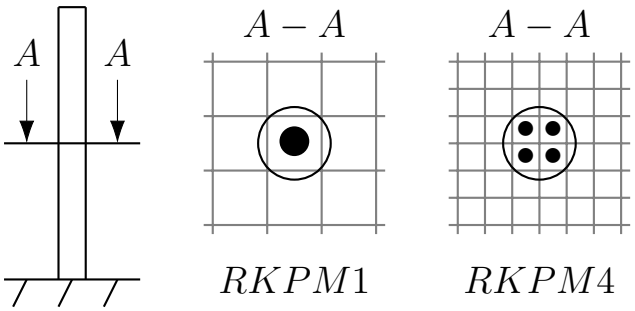


Figure 2.12: Filament cross section representation with RKPM method using one (RKPM1) or four (RKPM4) blobs.

are driven by a uniform pressure gradient in streamwise direction that maintains the bulk velocity $U_b$ of the flow constant, to keep the desired $Re_b$.

### 2.3.2 Assessment of the IB method behaviour

To verify the suitability of the method that we have used to enforce the zero velocity conditions at the stems locations, we compare results from simulations that have been carried out using an identical box, smaller than the case studied in this work, with identical driving force, but with two different IB methods adopted to enforce the presence of the stems. The reference case adopts the bilinear direct forcing (DF) approach (Fadlun et al., 2000), that was already validated in our code (Pinelli et al., 2017). This approach delivers a sharp zero velocity condition on the immersed body surface but requires a significantly higher resolution in the horizontal planes within the canopy. The second approach (RKPM) is the one chosen for the present study. The RKPM IB method approximates each filament using a set of nodes distributed on a formally unidimensional stem. The effective thickness of the filaments depends on the size of the support containing the mesh nodes surrounding each stem node. Here we consider two cases where the representation of the cross section of the filament is kept into account either using one single blob (a support obtained using three mesh nodes in each direction, see Figure 2.5b – RKPM1) or using four adjacent blobs (a support made by the union and intersection of the three mesh nodes support of the four single blobs – RKPM4), as sketched in Figure 2.12. Since this is a purely numerical exercise, we have considered small boxes to compare the three cases, DF vs RKPM1 vs RKPM4. In particular, we chose a box built around a set of four filaments. The distribution of nodes along each stem for the RKPM cases (i.e., the normal resolution) is kept uniform. The cross plane resolution needs to be adopted to the IB method of choice, as summarised in Table 2.2. The simulations are driven by the same uniform pressure gradient, which has been chosen to be a periodic function of time mimicking a pseudo-turbulent condition obtained from a precursor simu-

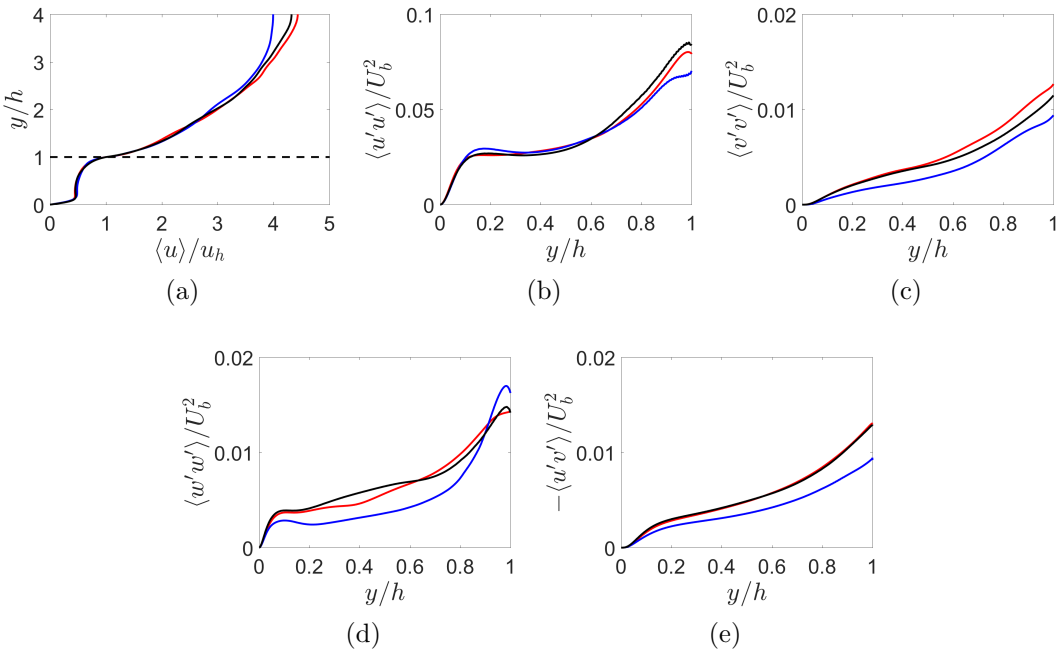


Figure 2.13: Methodology verification. Comparison of the inner velocity and rms fluctuations profiles (note, the latter only in the in-canopy region) obtained by using DF, RKPM1 and RKPM4 methods: in solid red, the curve obtained using a typical direct forcing (DF); in solid blue and black, the curves obtained using RKPM1 and RKPM4, respectively. The dashed line in panel (a), where the full domain is considered, represents the canopy height $h$.

Table 2.2: Verification case parameters.

| | DF | RKPM1 | RKPM4 |
|---|---|---|---|
| $Re_b$ | $\approx 6000$ | $\approx 6000$ | $\approx 6000$ |
| $L_x/H$ | 0.25 | 0.25 | 0.25 |
| $L_y/H$ | 1 | 1 | 1 |
| $L_z/H$ | 0.25 | 0.25 | 0.25 |
| $h/H$ | 0.25 | 0.25 | 0.25 |
| $ni$ | 168 | 12 | 24 |
| $nj$ | 450 | 450 | 450 |
| $nk$ | 168 | 12 | 24 |

lation over a large computational box. The applied forcing term gives an average flow rate that sets the bulk Reynolds number,

$$Re_b = \frac{U_b\, H}{\nu} \approx 6000. \tag{2.69}$$

Figure 2.13 shows a good agreement among the mean velocity profiles normalised with their value at the canopy tip, $u_h$. However, the Reynolds stresses inside the canopy differ considerably. In particular, the RKPM1 method is not sufficiently accurate (solid blue lines in figure 2.13), while the approximate RKPM4 approach allows us to reproduce satisfactorily higher order statistics of the dynamics of the flow in the canopy region as compared to the highly resolved DF method. This numerical test allows to determine the size of the filament diameter obtained using a RKPM method that does not define a sharp boundary surface but rather a set of mesh nodes where the boundary condition is only weakly enforced (Favier et al., 2014). In particular, by comparing with the sharp DF method, we found that the hydraulic diameter of each stem corresponds to approximately $1.15\Delta x$, i.e. 1.15 times the size of the finite volume cell in the horizontal direction. Using RKPM4 instead of the fully resolved DF approach allows a massive saving in terms of required computational resources, at least two orders of magnitude.

### 2.3.3 Validation case

While the baseline Navier-Stokes solver was extensively validated in the past (Omidyeganeh and Piomelli, 2011, 2013a,b, Rosti et al., 2016), its combination with a network of immersed filaments required further validation. To this end, we have considered the flow over a submerged canopy that was experimentally characterised by Shimizu et al. (1991). The parameters of the simulation used for the validation case are provided in Table 2.3 together with the corresponding experimental values (Shimizu et al., 1991). The velocity boundary conditions are set to no-slip at the bed and to free slip at the top surface, while the streamwise

Table 2.3: Validation case. The reference case is the experiment R31 carried out by Shimizu et al. (1991). The Reynolds numbers are defined through the flow depth $H$, and the bulk velocity $U_b$, the friction velocity computed at the wall, $u_{\tau,in}$ and the friction velocity computed at the canopy tip, $u_{\tau,out}$, from top to bottom respectively.

| | Current | Ref. |
|---|---|---|
| $Re_b$ | 7070 | 7070 |
| $Re_{\tau,in}$ | 535 | – |
| $Re_{\tau,out}$ | 1310 | – |
| $L_x/H$ | $2\pi$ | – |
| $L_y/H$ | 1 | 1 |
| $L_z/H$ | $1.5\pi$ | – |
| $h/H$ | 0.65 | 0.65 |
| $\lambda$ | 0.83 | 0.83 |
| Resolution | | |
| $\Delta x^+_{in} \times \Delta y^+_{\mathrm{w},in} \times \Delta z^+_{in}$ | $6 \times 0.15 \times 6$ | – |
| $\Delta x^+_{out} \times \Delta y^+_{\mathrm{h},out} \times \Delta z^+_{out}$ | $20 \times 0.5 \times 20$ | – |

and the spanwise directions are set to be periodic. The domain is discretised with a Cartesian grid system with a number of nodes (equispaced in streamwise and spanwise directions) that yield a resolution in inner viscous units of $\Delta x^+_{in} \approx 6$, $\Delta y^+_{w,in} \approx 0.15$ and $\Delta z^+_{in} \approx 6$, in the streamwise, wall-normal and spanwise directions, respectively. The inner viscous units are defined as

$$\Delta x^+_{i,in} = \frac{u_{\tau,in}\,\Delta x_i}{\nu} \tag{2.70}$$

being $u_{\tau,in} = (\tau_w/\rho)^{0.5}$ the friction velocity obtained from the wall shear stress at the bottom wall. Alternatively, one could define the viscous units as

$$\Delta x^+_{i,out} = \frac{u_{\tau,out}\,\Delta x_i}{\nu}, \tag{2.71}$$

being $u_{\tau,out}$ the friction velocity obtained from the total shear stress on a plane parallel to the bottom wall, located at the canopy (the region with the highest shear stress). With this alternative definition, the resolution measured using the viscous units computed turns out to be $\Delta x^+_{out} \approx 20$, $\Delta y^+_{h,out} \approx 0.5$ and $\Delta z^+_{out} \approx 20$.

The comparison of the mean velocity profile with the reference experimental data reveals to be very good, as shown in the left panel of Figure 2.14. The inset in the same figure highlights the imposition of part of the free slip condition, i.e. $\partial u/\partial y = 0$, that has been numerically imposed as

$$u_{nj} = u_{nj-1}, \tag{2.72}$$

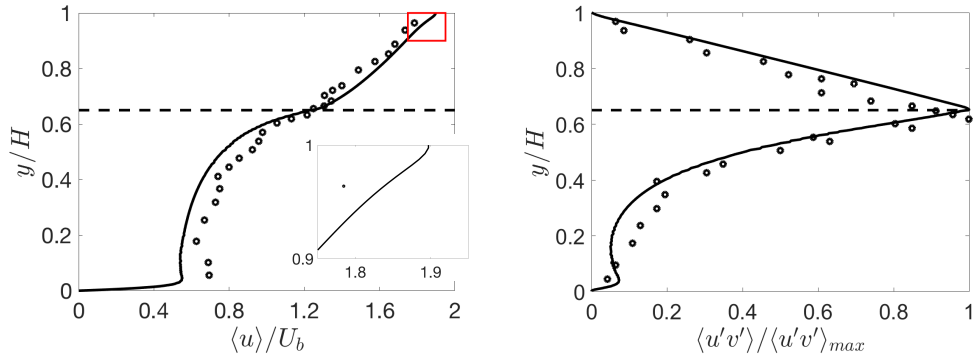


(a) (b)

Figure 2.14: On the left, comparison of the predicted mean velocity profile (solid line) with the experimental values R31 of reference Shimizu et al. (1991) (dotted curve). The inset represents the zoom of the area highlighted in red. On the right, Reynolds shear-stress distribution predicted by our numerical method (solid line) versus the experimental value R31 (Shimizu et al., 1991). The dashed line represents the location of the canopy tip $h$.

being $nj$ the number of points used to discretise the mesh in the wall-normal direction. In the same way, we impose all the Neumann conditions of (2.61). This numerical imposition of the boundary condition has been applied to all the cases described in the next chapters.

Concerning the comparison of the Reynolds shear stress, the profiles plotted in the right panel of Figure 2.14 show a satisfactory agreement. Some minor inconsistencies can be observed in the velocity profile that can be attributed to the limitations of the measurement technique in the region close to the solid elements.

### 2.3.4 Summary

The most important methodological feature of the present thesis concerns the treatment of the canopy elements. In particular, we have used an improved and adapted version of the IB method described in §2.2 to enforce the zero-velocity boundary conditions on every stem.

In this chapter, we have introduced the baseline IB method and the considered variations whose accuracy and reliability have been assessed by conducting a series of numerical experiments. The preliminary part of the methodology has concerned the set-up of a benchmark case made of a limited number of filaments embedded in a background flow mimicking turbulent conditions. Although the case has no physical meaning, it allowed us to assess and tune the IB method

selected to model the presence of the stems. In particular, the verification and the accuracy assessment has been carried out by comparing the results of two weak IB methods (RKPM with two different numbers of Lagrangian points representing the cross section of the filaments, termed RKPM1 and RKPM4, see §2.3.2) with a direct IB method that guarantees a sharp imposition of the boundary conditions at the stems surfaces. This systematic comparison has shown that RKPM4 delivers mean statistical values in very good agreement with the more computationally expensive predictions obtained using the direct IB method (see §2.3.2). The assessment campaign has also allowed the calibration of the IB method. In particular, the diameter of the stems that depends on the support and the density of the underlying grid has been measured.

To validate the overall methodology, we compared our numerical predictions with the measurements of Shimizu et al. (1991). The comparison between the mean values measured in a rigid canopy and the actual predictions presented in §2.3.3 showed a quite good agreement. All the simulations that will be presented in the results sections have been undertaken using a very similar resolution in the cross plane $x - z$ as the one used to assess our predictions versus the aforementioned experiment.

# Chapter 3

# Flow over a rigid wall-normal canopy in a mildly dense regime

Although some pioneering numerical simulation started to appear in the literature (see Chapter 1), their use was limited to very dense canopy scenario, where the flow has difficulties to seep into the thick layer of stems (Finnigan et al., 2009). Thence, the simulations proposed in the literature do not resolve the canopy "stem-by-stem" by imposing the required zero-velocity boundary conditions on each element, but rather rely on modelling the presence of the canopy via a distributed set of body forces mimicking the drag offered by the canopy on the flow. This approach breaks down when applied to sparser canopies, where the hydrodynamic interactions between the stems become progressively important as the stem Reynolds number, $Re_d(y) = U_{can}(y)\, d/\nu$ (being $d$ the stem diameter and $U_{can}(y)$ the mean streamwise velocity inside the canopy) increases and local von Kármán wakes generate extra vorticity. Moreover, those models fail to predict the drag close to the stems extrema because the finite size of the filamentous elements is not kept into account by a quadratic law (Bailey and Stoll, 2013, 2016).

Differently from other authors (Sharma and García-Mayoral, 2018), the approach that we have considered in this thesis relies instead on a genuine direct simulation inside the canopy (see §2.3). To our knowledge, this is the first simulation of a canopy flow offering such a high level of accuracy. In particular, we report results obtained using an LES of a fully developed turbulent flow through an open channel bounded by a shallow submerged, mildly dense, rigid vegetation layer. The aim of the work is to explore the mechanisms that govern the interaction between the turbulent flow and the canopy in a regime that, a priori, cannot be classified as dense or sparse. Identifying the proper scaling of a turbulent canopy flow in this regime is also one of the major motivations.

This chapter is subdivided as follows: firstly a brief set-up of the numerical simulation, introducing the parameters used, will be presented §3.1, after that

Table 3.1: Simulation parameters.

| | External units | Inner wall units | Outer wall units |
|---|---|---|---|
| Reynolds number | $Re_b$ 6000 | $Re_{\tau,in}$ 270 | $Re_{\tau,out}$ 940 |
| Length | $l/H$ | $l^+_{in}$ | $l^+_{out}$ |
| $L_x$ | $2\pi$ | 1700 | 5900 |
| $L_y$ | 1 | 270 | 940 |
| $L_z$ | $1.5\pi$ | 1270 | 4430 |
| $h$ | 0.25 | 68 | 236 |
| $\Delta S$ | $L_x/48$ | 35 | 133 |
| Resolution | $\Delta l^+_{in}$ | $\Delta l^+_{out}$ | |
| $\Delta x \times \Delta y_{\mathrm{w/h}} \times \Delta z$ | $3 \times 0.3 \times 3$ | $11 \times 0.3 \times 11$ | |

the results will be reported and discussed §3.2. Finally, some conclusions will be drawn in §3.3.

## 3.1 Numerical set-up

The solver tackles the LES governing equations (2.66) using a second order accurate, cell centred finite volume approach described in Chapter 2. As described in §2.3.1, the domain has been divided into tiles of area $\Delta S^2$ and a single filament has been placed with a random uniform distribution in every tile (see Figure 2.11). The tile size ($\Delta S$) and the filament height $h$ have been chosen in order to design a mildly dense canopy, based on the solidity parameter, $\lambda = d\,h/\Delta S^2$ (Nepf, 2012a) (in particular, here $\lambda \approx 0.35 > 0.1$).

The simulation has been carried out on a periodic in streamwise (i.e. $x$) and spanwise (i.e. $z$) directions domain. The size of the computational box is $L_x = 2\pi H$, $L_y = H$ and $L_z = 3/2\pi H$, (a size similar to the one used by Bailey and Stoll, 2013), being $H$ the open channel height. At the bottom wall, a no-slip boundary condition is imposed while a free slip condition is set at the top surface. A sketch of an $(x-y)$ slice of the domain with the respective boundary conditions applied is shown in Figure 2.10.

As similarly done in §2.3.3, the domain is discretised with a Cartesian lattice, equispaced in streamwise and spanwise directions and stretched in the wall-normal direction using two tangent hyperbolic distributions, inside and outside the canopy, ensuring that the ratio between neighbouring cells in the interval $[0, h] \cup [h, H]$ is kept below 4%. The stretching in the wall-normal lattice is meant to capture the high velocity gradients at the wall and at the canopy tip.

The number of nodes chosen yields a resolution in inner viscous units of

$\Delta x^+_{in} \approx 3$, $\Delta y^+_{\mathrm{w},in} \approx 0.3$ and $\Delta z^+_{in} \approx 3$, in the streamwise, wall-normal and spanwise directions, respectively. The definition of the generic inner viscous units, $\Delta l^+_{in}$ is given in (2.70). For the region above the canopy, we considered a virtual wall for the outer flow (later on, we will explain how the virtual wall location has been computed) and computed the viscous length on that virtual origin, a slightly different definition of $\Delta l^+_{out}$ from (2.71). The resolution for the outer flow turned out to be $\Delta x^+_{out} \approx 11$, $\Delta y^+_{vo,out} \approx 0.3$ and $\Delta z^+_{out} \approx 11$, in the streamwise, wall-normal and spanwise directions, respectively. The subscripts $w$ and $vo$ indicates the location of the *wall* and the *virtual origin*, respectively. The resolution and the simulation are validated and numerically verified (see §2.3.4).

The simulation is driven by a uniform pressure gradient in streamwise direction that keeps the bulk velocity $U_b$ of the flow, i.e. (2.67), constant and the Reynolds number based on the bulk velocity and the domain height $H$ has been fixed to $Re_b = 6000$, which is in the range of the one used in the experiments reported in Ghisalberti and Nepf (2004). The simulation parameters are summarised in Table 3.1.

The simulation ran for about 2000 hours on 96 processors of the Cray XC30 (Phase 2) supercomputer of ARCHER, the UK National Supercomputing Service.

## 3.2 Results

As clearly visible from Figure 3.1 (a), the mean velocity profile of a turbulent canopy flow in a sufficiently dense regime (e.g., $\lambda > 0.1$, Nepf, 2012a) exhibits two inflection points (Nepf, 2012a, Poggi et al., 2004), one at the edge of the canopy and the other closer to the wall. The inflection points of the mean profile are ultimately caused by the drag exerted by the filamentous layer on the flow that produces a convexity in the velocity profile. The location of the inflection points can be evaluated by determining the zeros of the average momentum balance in the streamwise direction,

$$\frac{1}{Re_b}\frac{\mathrm{d}^2\langle u\rangle}{\mathrm{d}y^2} = \frac{\partial P}{\partial x} + \frac{\mathrm{d}\langle u'v'\rangle}{\mathrm{d}y} + \langle D\rangle. \tag{3.1}$$

In the above, the symbol $\langle\ \cdot\ \rangle$ represents the triple average in time and in the two homogeneous, $x$ and $z$, spatial directions (note that the average includes the volume occupied by the stems). In the balance equation (3.1), the first term represents the mean viscous force, the second is the mean pressure gradient, the third is the contribution of the mean Reynolds stresses and $\langle D\rangle$ contains the mean canopy drag. The two inflection points enclose a transitional zone between two boundary layers located in the innermost and outermost portions of the canopy (Poggi et al., 2004) and can be thought of as a local Couette-type flow. Figure 3.1 (b) shows the mean velocity profile of the inner and the outer layers

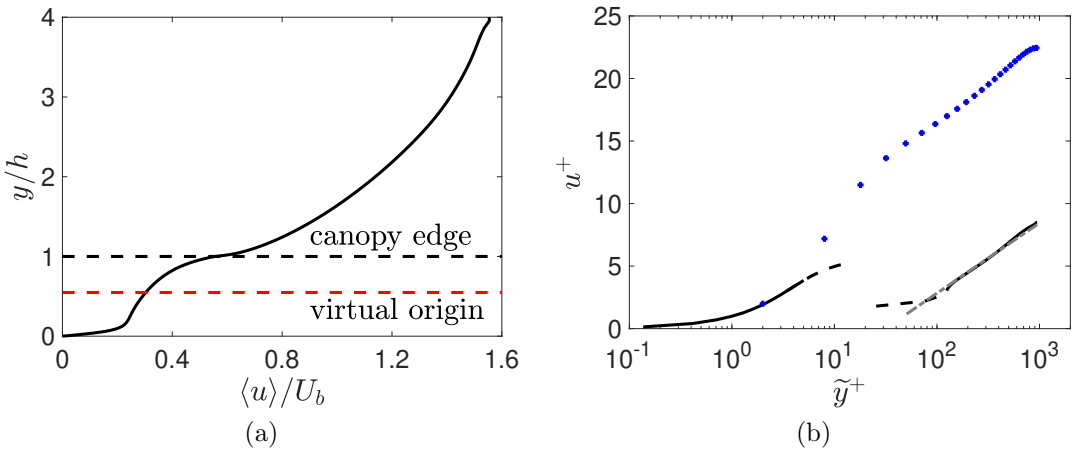


Figure 3.1: Mean velocity profiles. On the left panel (a): mean velocity profile normalised with the outer units. The black dashed line represents the canopy height at $y = h$. The red dashed line identifies the position of the virtual origin of the outer region. On the right panel (b), the blue dotted line shows the velocity profile of a channel flow over a smooth wall at $Re_\tau = 950$ (Hoyas and Jiménez, 2008). The black line represents the results of the present simulation scaled with the inner and the outer wall units. The coordinate $\widetilde{y}^+$ indicates the wall-normal distance in wall units of the inner and outer flow from their respective origins, i.e. $\widetilde{y}^+ = y\ u_{\tau,in}/\nu$ in the inner region and $\widetilde{y}^+ = (y - y_{vo})\ u_{\tau,out}/\nu$ in the outer region.

made dimensionless using two different friction velocities inside and outside the canopy. In particular, for the inner boundary layer, the friction velocity has been defined as $u_{\tau,in} = \sqrt{\tau_w/\rho}$, $\tau_w$ being the skin friction at the bottom wall (i.e. $y/H = 0$). Differently, the external velocity profile is scaled with $u_{\tau,out}$, a velocity scale computed using the total shear stress evaluated at location $y_{vo}$ within the canopy. In particular, $y_{vo}$ is the origin of the "external boundary layer" assumed to obey the "shifted" velocity log-law,

$$\langle u \rangle = \frac{u_\tau}{\kappa} \log\left[\frac{(y - y_{vo})u_\tau}{\nu}\right] + B, \tag{3.2}$$

where $u_\tau = u_\tau(y_{vo})$, being $B$ a parameter that depends on the roughness of the wall surface. Equation (3.2) is a nonlinear, implicit equation that can be used to determine the value of $y_{vo}$ for any given value of $\kappa$. Table 3.2 shows a sensitivity analysis of the location of the virtual origin and of the external friction Reynolds number for values of the von Kármán constant $\kappa$ chosen within the range $[0.37 - 0.43]$, an interval covering a wide range of values obtained in experiments and simulations for various geometrical configurations (Bailey and Stoll,

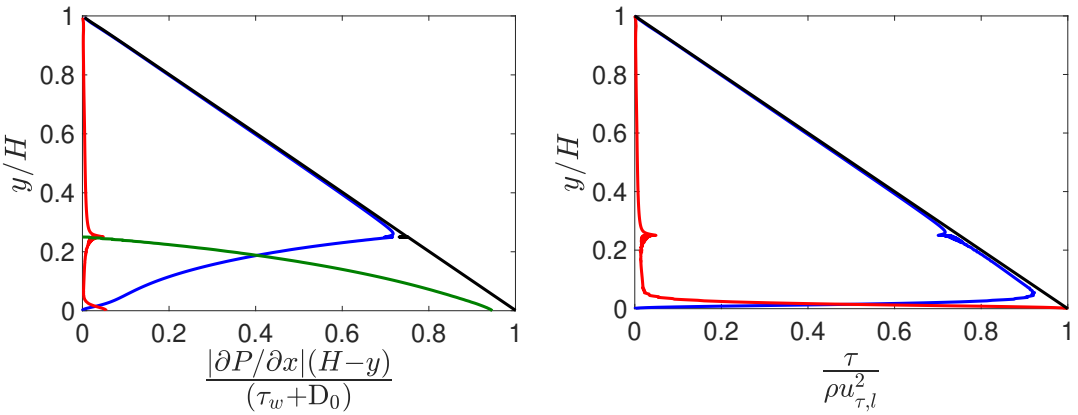


(a) (b)

Figure 3.2: Pressure gradient balance. (a) Black line: left hand side of equation (3.3); Red line: viscous shear stress; Blue line: Reynolds shear stress; Green line: cumulative drag component. The term, $D_0 = \int_0^H \langle D \rangle \, dy$, represents the integral of the mean drag. (b) Same as (a) but the viscous and the Reynolds shear stress have been rescaled with the local friction velocity defined in (3.8).

2013). The variations of the coordinate of the virtual origin are within 4% of

Table 3.2: Sensitivity analysis of the virtual origin location and friction Reynolds number as a function of the assumed constant $\kappa$ in (3.2)

| $\kappa$ | $y_{vo}/H$ | $Re_{\tau,out}$ |
|---|---|---|
| 0.37 | 0.1075 | 997 |
| 0.39 | 0.1231 | 970 |
| 0.41 | 0.1303 | 948 |
| 0.43 | 0.1494 | 926 |

$H$ for the considered range of $\kappa$. From now on, we consider a canonical value of $\kappa = 0.41$ that leads to a virtual origin location at $y_{vo}/h = 0.55$, as indicated in Figure 3.1 (a) with a dashed red line. Concerning the inner flow, Figure 3.1 (b) reveals that the flow matches a typical velocity profile of a turbulent channel flow only in the viscous sub-layer, where the wall skin friction drag dominates the drag of the stems. As it will be further discussed, it is also noticed that the buffer layer profile is completely altered by the combined actions of the stems-induced hydrodynamics and by the penetration of the outer flow. Differently, when scaling the outer flow velocity profile with the friction velocity computed at the virtual origin, a standard boundary layer logarithmic profile is recovered. As expected, the intercept $B$ in equation (3.2) differs from the usual value of a flow over a smooth wall, indicating that the canopy layer behaves like a rough

surface as seen by the outer flow (Jiménez, 2004). Although the standard buffer layer characteristics are altered by the presence of the stems, overall the logarithmic structures of the outer flow are not significantly modified. In different frameworks, other authors (Flores and Jiménez, 2006, Mizuno and Jiménez, 2013) have reported the robust behaviour of the outer, large-scale motions in the logarithmic layer even in presence of strong alterations of the region close to the wall (i.e. the buffer layer). In particular, Flores and Jiménez (2006) have carried out numerical experiments replacing the smooth-wall boundary condition with imposed velocity disturbances, while Mizuno and Jiménez (2013) have completely removed the wall imposing instead a condition based on matching a prescribed buffer layer turbulent velocity profile representative of the mean flow over rough surfaces. Both numerical experiments showed a very robust and consistent behaviour of the outer flow structure independently of the imposed manipulations at the wall.

Next, we consider the average momentum balance (3.1) integrated from the wall to a distance $y$ measured from the bed location,

$$\frac{\partial P}{\partial x} y + \tau_w + \int_0^H \langle D \rangle \, \mathrm{d}y = \mu \frac{\mathrm{d}\langle u \rangle}{\mathrm{d}y} - \rho \langle u'v' \rangle + \int_y^H \langle D \rangle \, \mathrm{d}y. \tag{3.3}$$

Integrating equation (3.1) again, using as an upper limit of the integral the free slip surface location, i.e. substituting $y = H$ in equation (3.3), the total balance (3.3) reads as

$$\tau_w + \int_0^H \langle D \rangle \, \mathrm{d}y = -H \frac{\partial P}{\partial x}. \tag{3.4}$$

Therefore, equation (3.3) can be also restated as

$$\left(1 - \frac{y}{H}\right) \left|\frac{\partial P}{\partial x}\right| H = \mu \frac{\mathrm{d}\langle u \rangle}{\mathrm{d}y} - \rho \langle u'v' \rangle + \int_y^H \langle D \rangle dy. \tag{3.5}$$

In the previous equation, we have used the absolute value of the pressure gradient to highlight that the left-hand-side of the balance (3.5) is a non-negative quantity. The computed contributions of all the terms appearing in the balance are reported in Figure 3.2 (a). To include the contribution of the mean drag into the shear stress, we can reorganise equation (3.5), obtaining the balance

$$\mu \frac{\mathrm{d}\langle u \rangle}{\mathrm{d}y} - \rho \langle u'v' \rangle = \left(1 - \frac{y}{H}\right) \left|\frac{\partial P}{\partial x}\right| H - \int_y^H \langle D \rangle \, \mathrm{d}y = f(y) \left(1 - \frac{y}{H}\right) \left|\frac{\partial P}{\partial x}\right| H, \tag{3.6}$$

In (3.6), $f(y)$ is a dimensionless shape function defined as

$$f(y) = 1 - \frac{\int_y^H \langle D \rangle \, \mathrm{d}y}{\left(1 - \frac{y}{H}\right) \left| \frac{\partial P}{\partial x} \right| H}. \tag{3.7}$$

The balance provided by equation (3.6) allows introducing a local friction velocity (Sharma and García-Mayoral, 2018, Tuerke and Jiménez, 2013) that incorporates the contribution of the mean drag in the total stress as

$$u_{\tau,l}(y) = \sqrt{\frac{f(y)}{\rho} \left| \frac{\partial P}{\partial x} \right| H} = \sqrt{\frac{\mu \, \mathrm{d}_y \langle u \rangle - \rho \langle u'v' \rangle}{\rho(1 - y/H)}}. \tag{3.8}$$

It is easy to verify that, when the total stress is scaled by $u_{\tau,l}(y)$, the non-dimensional linear profile $(1 - y/H)$ is recovered as also apparent in Figure 3.2 (b).

Figure 3.3 shows the diagonal Reynolds stresses outside and inside the canopy, with a standard and a local normalisation (i.e. obtained using as a velocity scale $u_{\tau,l}(y)$ given in (3.8)). Outside the canopy, the velocity fluctuations reveal a clear resemblance with the ones in an open channel flow over a rough surface, as for example reported by Scotti (2006). The behaviour of the diagonal stresses outside the canopy highlights once more that, away from the wall, surface roughness or even filamentous canopy elements have little effects on the structures of the external flow. In Figure 3.3, we also compare the normal Reynolds stresses distribution, made non-dimensional with both the local friction velocity, as in (3.8) and with the outer friction velocity $u_{\tau,out} = u_\tau(y_{vo})$. The figure also displays how the canopy influences the velocity fluctuations in the wall-parallel directions by weakening the streamwise component, while significantly increasing the intensity of the spanwise fluctuations. This redistribution of velocity fluctuations is generated by the presence of the stems that disrupt the coherence of the streamwise velocity fluctuations while acting as obstacles that continuously deviate the flow in the spanwise direction. This mechanism is confirmed by the distribution of the vertical component of the velocity fluctuations that remain almost unaffected by the blocking effect of the obstacles, showing the "bi-dimensional" effect of the stems in the innermost region of the canopy. From Figure 3.3, one can also assess the range of validity of the proposed scaling (3.8) that holds valid until the canopy edge region is approached. A possible explanation of this deficiency can be based on the unbalance between turbulence production and dissipation as already suggested for flows with an imposed, discontinuous body force by Tuerke and Jiménez (2013). From Figure 3.4, we notice a production peak close to the bed that, differently from a standard channel flow, drops soon after having reached its maximum

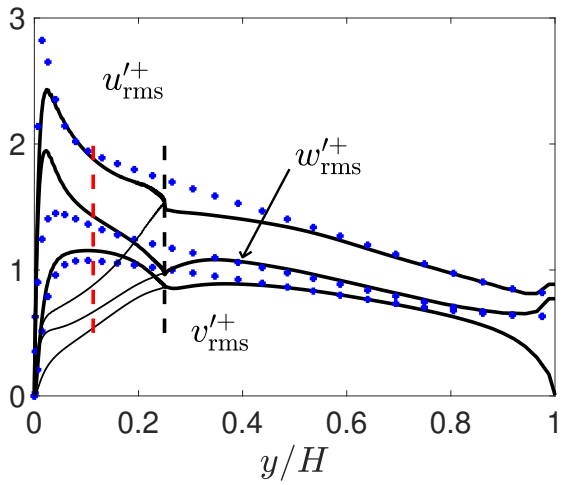


Figure 3.3: Velocity fluctuations RMS. Comparison between the present case (solid black) normalised with the local friction velocity $u_{\tau,l}$ (thicker line) and the reference values from the turbulent channel flow at $Re_\tau = 950$ (Hoyas and Jiménez, 2008) (blue dotted). The difference in $v'^{+}$ at the top of the domain is due to the different boundary conditions (open channel vs. channel flow) applied for the simulation. The thin black solid line represents the RMS of the velocity fluctuations normalised with the outer friction velocity $u_{\tau,out}$ evaluated at $y_{vo}$. The black and red dashed lines refer to the same locations as in Figure 3.1.

value. A second broader peak is also present just outside the canopy region indicating that a production mechanism, similar to the one found at the bed (i.e. a wall production cycle, Jiménez and Pinelli, 1999) also operates by the interface canopy-outer flow. In Figure 3.5, the joint p.d.f. of $u'$ and $v'$ at a distance from the virtual origin $y^+_{out} = (y - y_{vo})\ u_{\tau,out}/\nu = 48$ is shown together with the same quantity measured at a similar distance (i.e. $y^+ = 35$) from a smooth wall in a plane turbulent channel flow (Ong and Wallace, 1998). The comparison between the two indicates that the canopy tip behaves as a permeable wall for the outer flow inducing a shift of the peak towards the second quadrant (i.e. positive $v'$), while in an impermeable wall, where the sweeps events are more probable than ejections, the maximum is located in the fourth quadrant. Also note that, in Figure 3.5, the local maximum probability associated with negative streamwise velocity fluctuations occurring when the wall-normal velocity fluctuations are almost zero, is related to the presence of the canopy stems. Another interesting observation concerns the peaks of the velocity fluctuations whose locations match the ones of the reference channel flow data (Hoyas and Jiménez, 2008) although the extrema are located inside the canopy. From Figure 3.6, displaying the profiles of the vorticity fluctuations, it is noticed that the location of the peak of the wall-normal component $\omega_{y,rms}$ is only slightly shifted outwards when compared

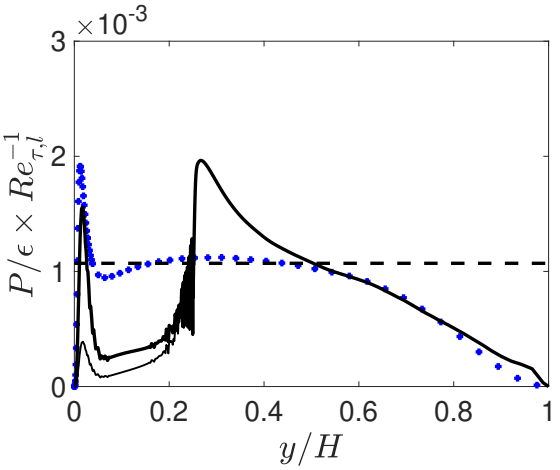


Figure 3.4: Turbulent kinetic energy production to dissipation ratio. Thick solid line: ratio normalised with the local friction Reynolds number, defined as $Re_{\tau,l} = u_{\tau,l}H/\nu$, where $u_{\tau,l}$ is as given in (3.8); Thin solid line: same quantity normalised with the outer friction Reynolds number; Dashed horizontal line: production to dissipation equilibrium condition (i.e. $1/Re_{\tau,l}$); Blue dotted symbols are plane turbulent channel flow data at $Re_\tau = 950$ (Hoyas and Jiménez, 2008).

to the set of channel flow reference data (Hoyas and Jiménez, 2008). The short distance between the peaks further emphasises the analogy between the outer region of the canopy flow with the flow developing over a rough wall. This shift between peaks can be attributed to the variation of the spanwise velocity fluctuation in the streamwise direction (i.e. $\partial w/\partial x$) caused by the presence of the filamentous canopy. The instantaneous snapshots in Figure 3.7, representing the velocity fluctuations on a plane parallel to the wall within the canopy and close to the bed, clearly illustrate the effect of the stems that deviate the flow in a sinuous fashion in the spanwise and streamwise directions contributing to the increase of the coherence of the spanwise velocity fluctuations $w'$.

Further insight on the emergence and on the organisation of the large coherent structures that characterise the flow can be obtained by considering the spectral energy content and the two-point velocity autocorrelation function of the velocity components. The top row of Figure 3.8 and of Figure 3.9 shows the premultiplied spectra and the two-point autocorrelation functions of the velocity fluctuations as a function of the distance from the bed and as a function of either wavelengths $\lambda_x$ or the streamwise separation $\Delta x$. Figure 3.8 was obtained by averaging the spectra of the velocity fluctuations in the spanwise direction, while Figure 3.9 was obtained by pre-applying the spanwise average operator, $\langle \cdot \rangle_z$, to the velocity fluctuations and then computing the two-point autocorrelation function in the streamwise direction. As an example, the autocorrelation function in the

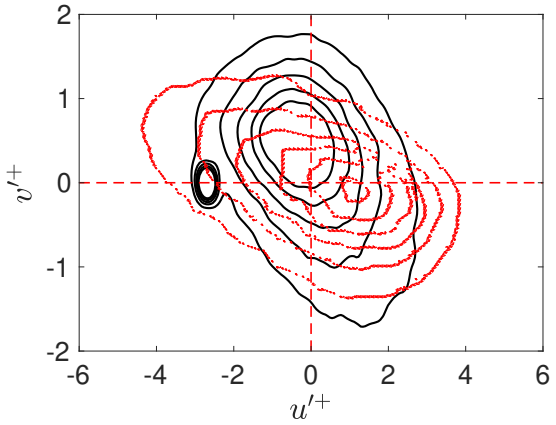


Figure 3.5: Joint probability density function of streamwise and wall-normal velocity fluctuations. Solid black iso-lines: actual predictions at $y/H = 0.18$ ($y^+_{out} = 48$) of $(u'^+, v'^+) = (u'/u_{\tau,l}, v'/u_{\tau,l})$. Dotted red lines: isolines from Ong and Wallace (1998) at $y^+ = 35$ in a smooth-wall channel flow. Range and increments as in figure 10(a) of Ong and Wallace (1998). Dashed red lines are the Cartesian axes passing through the origin.

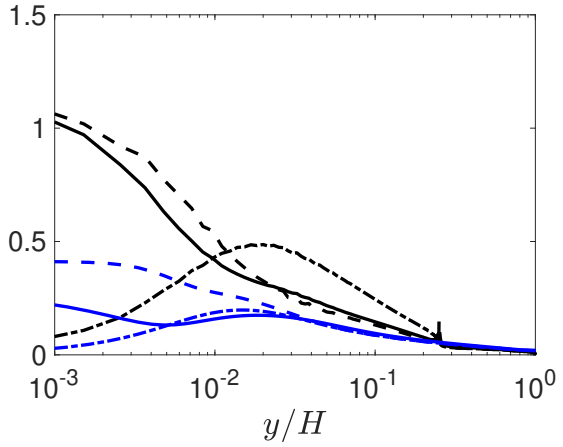


Figure 3.6: Black lines refer to the actual canopy simulation while the blue ones are taken from the channel flow data of Hoyas and Jiménez (2008). Solid line $\omega'^+_{x,rms}$, dashed-dotted line $\omega'^+_{y,rms}$, dashed line $\omega'^+_{z,rms}$. The wall units are based on the local friction velocity $u_{\tau,l}$.

streamwise direction of the pre-averaged $u$ component, $\langle u' \rangle_z$, can be computed as

$$R_{u'u'} = \frac{\langle \, \langle u' \rangle_z(0,y) \, \langle u' \rangle_z(\Delta x, y) \, \rangle}{\langle u' \rangle_z^2(0,y)}. \tag{3.9}$$

This technique is useful to evince the presence of the largest structures that popu-

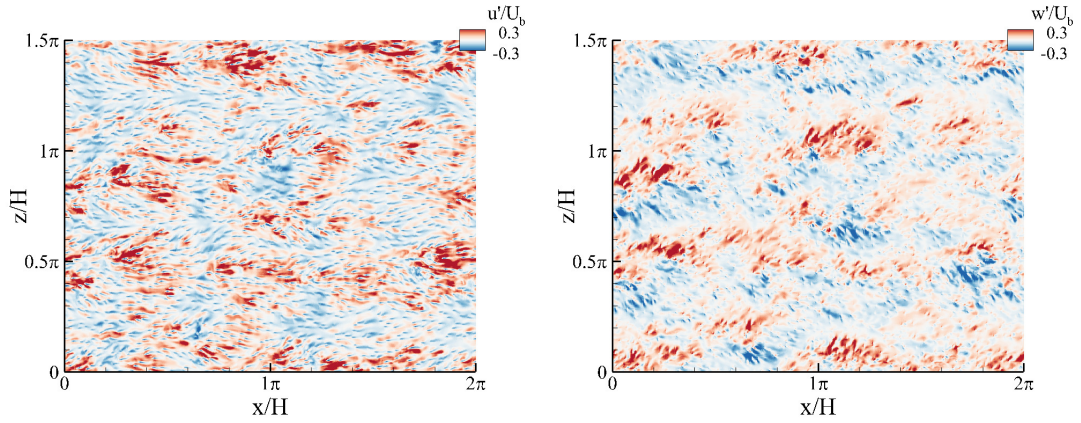


Figure 3.7: Panel (a): contours of instantaneous streamwise velocity fluctuations inside the canopy, on a plane located at $y/H = 0.02$. Panel (b): spanwise velocity fluctuations on the same plane as (a)

late the flow. The second row of the same two figures report the same quantities, averaged (or pre-applying the streamwise averaged operator, $\langle \cdot \rangle_x$, to the velocity fluctuations, as described above) in the streamwise direction as a function of either the spanwise wavelength $\lambda_z$ or the separation $\Delta z$. A quick glance at Figure 3.8 reveals the presence of fluctuations maxima taking place at three different spatial location along the wall-normal direction. Some extrema are localised in the outer region, while others lie within the canopy either in its core or in the bed proximity. With the aim of simplifying the interpretation of the spectra, we also consider Figure 3.10 illustrating the same premultiplied spectra as a function of the streamwise and spanwise wavelengths at three wall-normal locations ($y/H = 0.02$, $y/H = 0.18$ and $y/H = 0.63$) roughly corresponding to the centres of the three aforementioned regions (no space average involved). Concerning the outer region, panel (g) in Figure 3.10 and panel (a) of Figure 3.8 and Figure 3.9 reveal the presence of highly elongated streamwise velocity streaks that span a third of the domain in the spanwise direction (panel (d) of Figure 3.9). The large outer velocity streaks are also clearly visible in the instantaneous snapshot of Figure 3.11. The $v'$ and $w'$ spanwise energy maxima located just above the canopy displayed in panels (e) and (f) of Figure 3.8 show that the outer velocity streaks are connected with a system of streamwise vortices with an average streamwise length of roughly one channel height $H$ (see panels (b) and (c) of the same figure), separated by about the same distance $\lambda_z \simeq H$ in the spanwise direction (see panels (h) and (i) of Figure 3.10). The association between the outer streamwise velocity streaks and the aforementioned system of quasi-streamwise vortices is also revealed by the joint p.d.f. of the streamwise and wall-normal

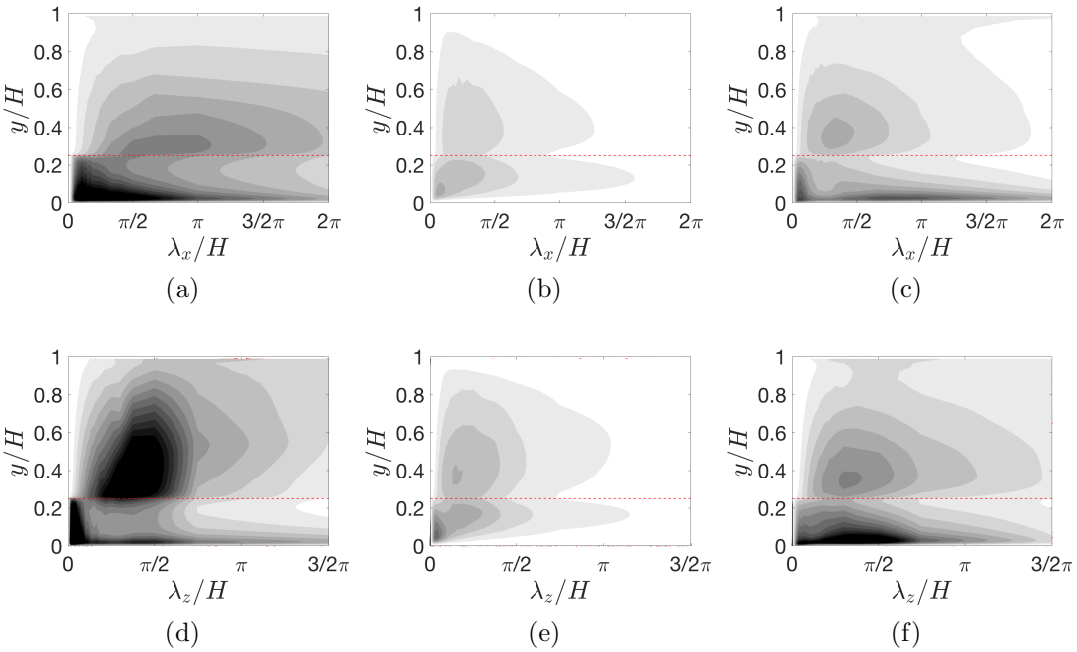


Figure 3.8: The panels in the first row are the premultiplied spectra of the velocity components as a function of the streamwise wavelength and the wall-normal coordinate: Panel (a): $\kappa_x \Phi_{u'u'}/u_{\tau,l}^2$; Panel (b): $\kappa_x \Phi_{v'v'}/u_{\tau,l}^2$; Panel (c): $\kappa_x \Phi_{w'w'}/u_{\tau,l}^2$. The panels in the second row are the premultiplied spectra of the velocity components as a function of the spanwise wavelength and the wall-normal coordinate: (d): $\kappa_z \Phi_{u'u'}/u_{\tau,l}^2$; Panel (e): $\kappa_z \Phi_{v'v'}/u_{\tau,l}^2$; Panel (f): $\kappa_z \Phi_{w'w'}/u_{\tau,l}^2$. The levels range from 0 (white) to 0.6 (dark) with spacing of 0.05. The red dashed line represents the canopy height. All the spectra are normalised with the local friction velocity.

vorticity components (Ong and Wallace, 1998) shown in Figure 3.12. The joint p.d.f., computed for two $x-z$ planes above the virtual origin at $y_{out}^+ = 48$ and 541, clearly indicates a preference for $\omega_x$ and $\omega_y$ to occur with the same sign at the same time (note that $\omega_x$ and $\omega_y$ represent footprints of the streamwise velocity streaks and of the quasi-streamwise vortices typical of wall-bounded flows, Jiménez and Pinelli, 1999). The streamlines obtained by space averaging the $v$ and $w$ component using a time snapshot plotted on the $y$–$z$ side of the computational box in Figure 3.11, offer a clear visual, further evidence of the presence of these streamwise vortices that penetrate vertically the whole canopy (see panels (d), (e) and (f) of Figure 3.9 as well). The existence of streamwise coherent velocity streaks above the canopy has been reported in previous studies (Bailey and Stoll, 2016, Finnigan et al., 2009). They also highlighted the co-existence of the outer velocity streaks with large hairpin vortices whose heads are sequentially pointing upward and downward. On one hand, our results seem to confirm

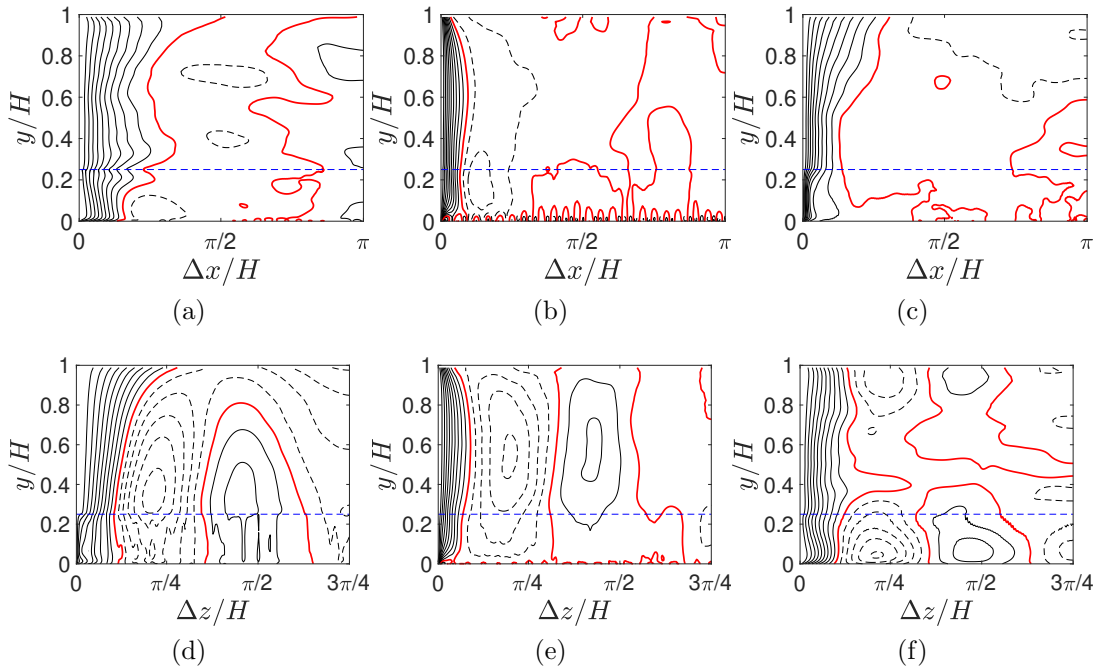


Figure 3.9: Contour maps showing the variation of the two-point autocorrelation functions of the velocity fluctuations. Panels (a), (b) and (c) in the first row refer to the streamwise auto-correlations of $u$, $v$ and $w$ respectively. Panels (d), (e) and (f) in the second row refer to the spanwise auto-correlations of $u$, $v$ and $w$ respectively. The contours are spaced by 0.1, starting from one. The negative values are plotted with a dashed line. The red line represents the zero-level. The leftmost column shows the streamwise velocity component $R_{u'u'}$, the central one shows the wall-normal component $R_{v'v'}$, and the rightmost column shows the spanwise component $R_{w'w'}$. Note that, in the panels of the first row, the spanwise average operator was pre-applied to the velocity fluctuations, and then the streamwise autocorrelation function was computed. In the panels of the second row, instead, the streamwise average operator was pre-applied to the velocity fluctuations, and then the spanwise autocorrelation function was computed (see equation (3.9) as an example).

that the outer flow is characterised by the typical structure found in the logarithmic region of wall-bounded flows. The latter is known not to be very much affected by the geometric details of the solid boundary, presenting an almost universal behaviour (Flores and Jiménez, 2006, Mizuno and Jiménez, 2013), thus verifying the Townsend's similarity hypothesis (Townsend, 1976). Concerning the sequence of hairpin vortices described by the aforementioned authors, the results of our simulation do not display any clear evidence of their presence. This may be attributed to the short distance between the canopy tip and the upper bound-

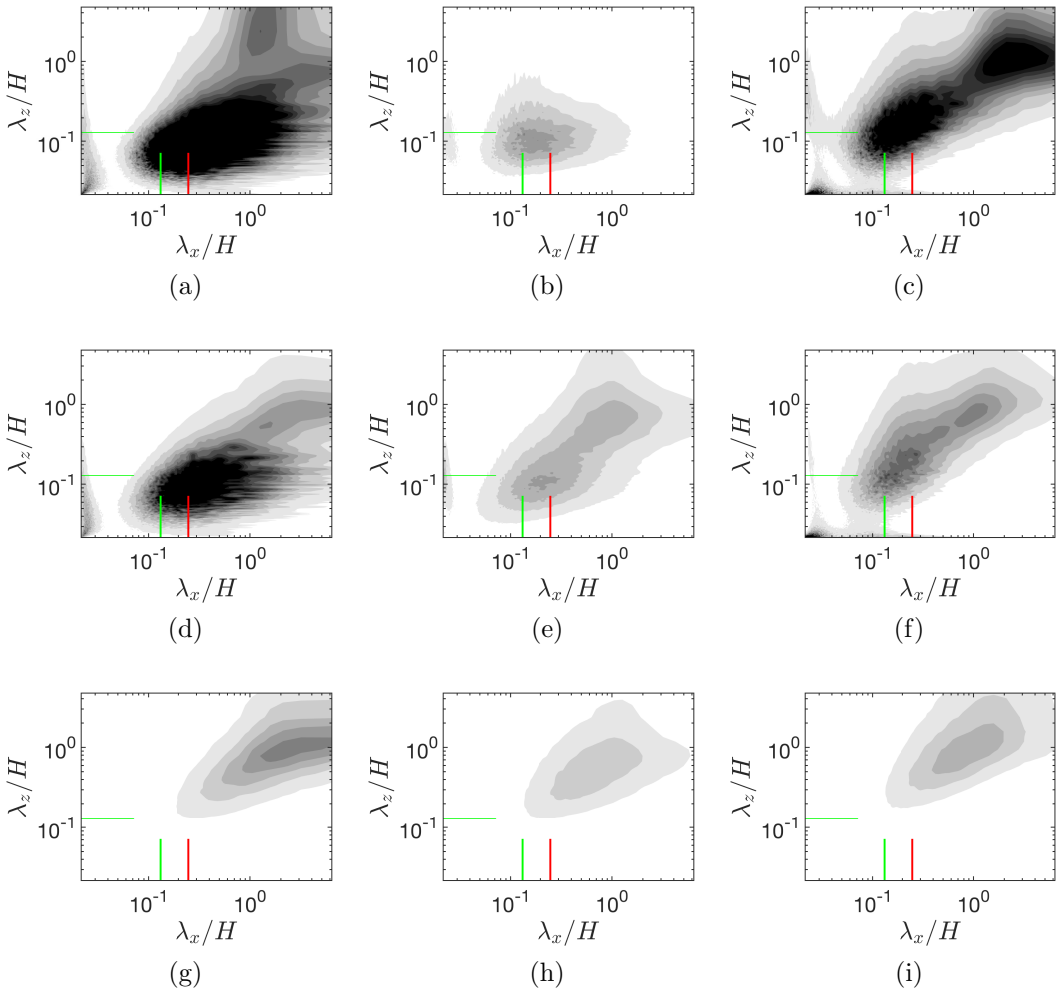


Figure 3.10: Contour maps showing the variation of the two-dimensional premultiplied velocity fluctuations spectra $\kappa_x \kappa_z \Phi_{u_i' u_i'} / u_{\tau,l}^2$ at three selected distances from the bottom wall. Panels (a), (b) and (c) are computed at $y/H = 0.02$ and refer to the streamwise, wall-normal and spanwise components, respectively. Panels (d), (e) and (f) represent the same spectra at $y/H = 0.18$ while the spectra in panels (g), (h) and (i) have been computed at $y/H = 0.63$. The short green lines mark the average filament spacing $\Delta S$, while the short red line marks the filament height $h$. The darkest colour represents the highest value, the grey levels range from 0 to 0.1 with iso-levels sampled at each 0.01 interval.

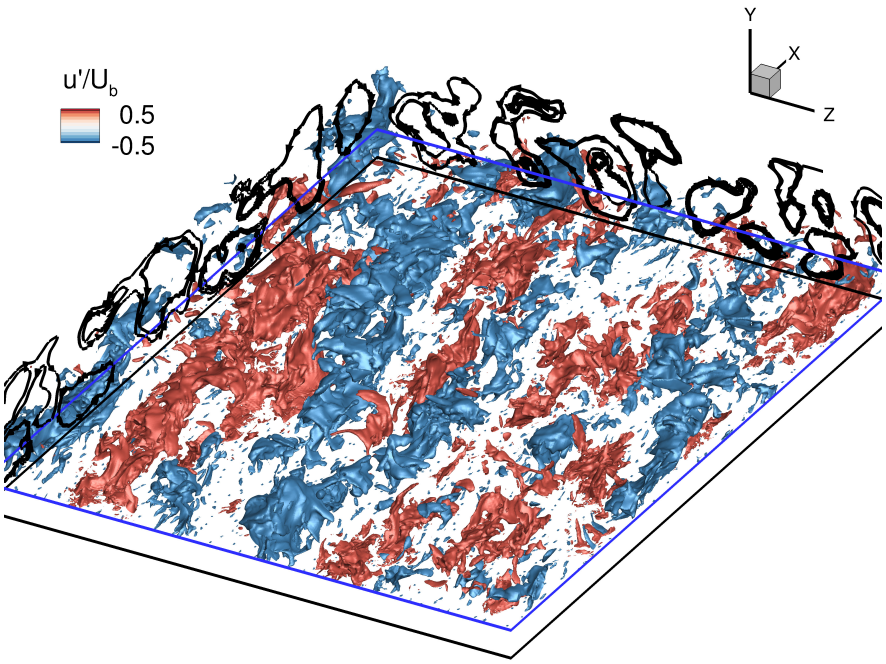


Figure 3.11: Instantaneous isosurfaces of streamwise velocity fluctuations. The streamlines drawn on the lateral sides have been obtained by averaging the instantaneous velocity fluctuations along the normal to the considered faces: the spanwise direction ($\langle u\rangle_z$, $\langle v\rangle_z$) for the left lateral side and the streamwise direction ($\langle v\rangle_x$,$\langle w\rangle_x$) for the frontal face. The plane indicated with the blue line corresponds to the tip of the canopy, while the black line indicates the bottom solid wall.

ary that would constrain the emergence of these structures in their wholeness by inhibiting the formation of their heads. The energy distribution in the region occupied by the core of the canopy is shown in the central row of Figure 3.10 that reveals a bimodal pattern. While the footprints of the outer structures are still visible for all velocity fluctuations (i.e. peaks at $\lambda_x/H = \lambda_z/H = \mathcal{O}(1)$ for $v'$ and $w'$, and $\lambda_x/H \sim 2-3$, $\lambda_z/H = \mathcal{O}(1)$ for $u'$), a set of new maxima is generated for shorter wavelengths. While the peak of $w'$ seems to be inherited from the outer vortices that penetrate the canopy (see also panel (f) of Figure 3.9), the peak of $u'$ in panel (d) of Figure 3.10 that penetrates down to the canopy bed (see panel (a) of the same figure) is related to the appearance of a system of spanwise oriented vortices. This observation is confirmed by two-point velocity autocorrelation functions, especially the one that concerns the normal-to-the-wall component that is less affected by the filtering effect of the canopy stems. In-

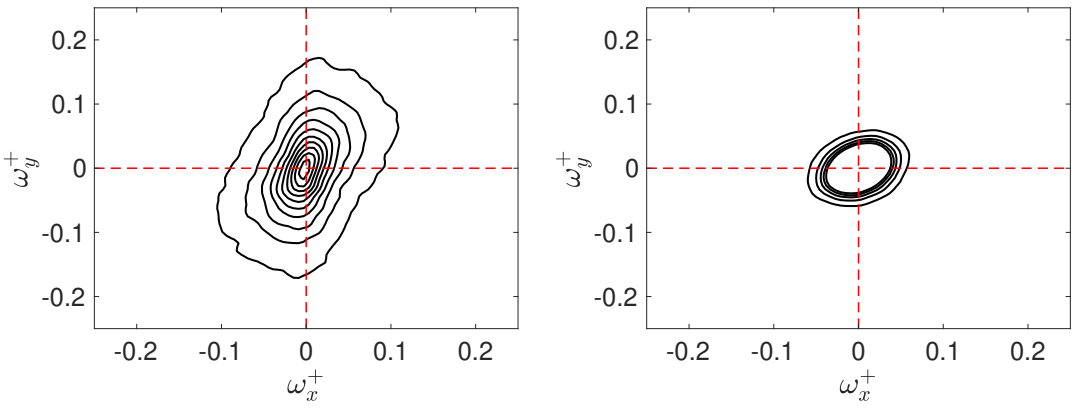


Figure 3.12: Joint probability density function of $\omega_x$ and $\omega_y$. Panel (a), on the left is computed on a $x-z$ plane at $y/H = 0.18$ ($y^+_{out} = 48$); Panel (b) is for a $x-z$ plane at $y/H = 0.63$ ($y^+_{out} = 541$). The vorticity components are normalised with $\nu/u^2_{\tau,out}$. Range and increment in (a) are [0:5:50], in (b) [0:10:50]. Red dashed lines are the Cartesian axes through the origin.

deed, panel (b) of Figure 3.9 shows that, inside the canopy, the $v'$ correlation goes from positive to negative values within a streamwise correlation length of roughly one canopy height that matches the one corresponding to maximum of the energy content of $v'$ (i.e. the location of the internal maxima in panel (e) of Figure 3.10). This system of vortices is not easily detectable from the streamwise two-point autocorrelation of $u'$ partly because of the disrupting effect of the canopy elements and partly because modulated in the spanwise direction by the presence of the outer structures: note that the spanwise correlation length of $u'$ in panel (d) of Figure 3.9 matches the ones of panels (e) and (f) in the same row of the same figure. Nonetheless, the existence of organised short spanwise rollers is confirmed by visual inspection of the streamlines plotted on the $x$–$y$ side of the box in Figure 3.11 (streamlines obtained by spanwise averaging the $u'$ and $v'$ component) and by the instantaneous isocontours of the streamwise velocity components close to the bed, revealing a strong directional coherence albeit chopped by the sweep-ejection action of the outer quasi-streamwise vortices. Moreover, the appearance of spanwise oriented rollers is a ubiquitous characteristic of all flow fields over textured surfaces (e.g. canopies (Nepf, 2012a), porous (Jiménez et al., 2001) or ribletted walls (García-Mayoral and Jiménez, 2011)) that induce an inflection point in the mean velocity profile. In our case, the inflection point is generated by the discontinuous drag imposed by the canopy on the mean flow and is located at its tip. As already pointed out by Finnigan et al. (2009), the inflection point leads to a Kelvin-Helmholtz instability that induces the forma-

tion of large spanwise rollers that are advected downstream by the mean flow. Finally, the panels (a) and (c) of Figure 3.10 show two intense peaks associated energy content of $u'$ and $w'$ fluctuations very close to the impermeable bed. These peaks are due to the presence of the wall that inhibits all wall-normal velocity fluctuations to take place. Because of the solenoidal condition on the flow field, strong accelerations or decelerations of the wall-normal velocity imply an insurgence of in-plane motions (i.e. $\partial_y v = -(\partial_x u + \partial_z w)$). In particular, the sweeps and ejections induced by the outer quasi-streamwise vortices and the spanwise rollers generate coherent $u'$ and $w'$ patterns that are clearly visible in Figure 3.7.

## 3.3 Conclusion

We have carried out a resolved numerical simulation of a turbulent flow over a rigid canopy with the aim of exploring the structure of the flow generated by the interaction of a pressure-driven open channel flow with a *mildly dense* filamentous layer covering the solid wall. This condition, often termed *transitional* (Nepf, 2012a), is achieved when the ratio between the in-plane solidity and the depth of the canopy is fixed to a value that corresponds to a physical situation in which the outer, turbulent structures partially penetrate the canopy and the contribution to the total drag offered by the canopy itself is comparable in magnitude to the one generated by the shear at the bed. The main conclusions of our work are of both methodological and physical character. Concerning the simulation methodology, it should be highlighted that the numerical technique that has been presented and validated in this work allows carrying out accurate and resolved canopy flow simulations efficiently. Indeed, to the authors' knowledge, this is the first time that a canopy-flow simulation in which the physical boundary values are imposed stem-by-stem has been reported in the literature. The other main conclusions concern the physical characterisation of the flow. In the particular regime that has been considered the flow can be roughly divided into three regions. The outer region shows strong similarities with high Reynolds number wall turbulence developing over a rough, solid boundary. The classical logarithmic velocity profile can be obtained by introducing a classical shift of the origin of the wall-normal axis (i.e. a *virtual origin* located inside the canopy). The scalings of the outer fluctuations, normalised in wall units based on the friction velocity obtained from the total stress at the virtual origin, also present a reasonable collapse over data obtained by other authors in the logarithmic layer of turbulent channel flows at moderately high Reynolds numbers. The structure of the outer flow resembles the one found within the logarithmic layer of wall-flows at Reynolds numbers sufficiently high to allow a scale separation: long elongated velocity streaks flanked by vortices oriented along the streamwise direction. The streamwise vortices are particularly intense and, because of the high wall-normal permeability of the

canopy, they fully penetrate the canopy eventually reaching the bed. The intra-canopy-region velocity distribution scales reasonably well with a friction velocity distribution obtained locally along the wall-normal direction. The mean velocity profile shows two inflections points. The top one is imposed at the canopy tip by the drag discontinuity and, in turns, it is known to trigger a Kelvin-Helmholtz instability producing a series of counter-rotating spanwise rollers that may form a mixing-layer of quasi-constant thickness above the canopy (Nepf, 2012a). According to some authors, this system of spanwise vortices would induce a series of alternating regions of upwash and downwash events that would locally bend up or bend down the rollers forming the so-termed *head-up*, *head-down* hairpin vortices (Finnigan et al., 2009). Our simulation seems to offer an alternative point of view in which the spanwise vorticity formed as a consequence of the inflectional instability loose part of its coherence as a result of the strong sweeps and ejections generated by the outer, quasi-streamwise vortices. The existence or the prevalence of this mechanism or of the one based on the self-induced lifting and depression of the rollers proposed by other authors probably depends on the parameters defining the canopy solidity. Finally, the region in the proximity of the bed is again strongly influenced by the outer structures which provoke vigorous inrush and ejections towards and from the bed that encounter almost no resistance in the wall-normal direction. The wall-normal velocity field induced by the outer flow interacts with the impermeable bed conditions forming organised streamwise and spanwise velocity patterns in the proximity of the wall.

# Chapter 4

# On the genesis of different regimes in canopy flows: a numerical investigation

In this chapter, we report the analysis on wall-resolved large-eddy simulations of flows over submerged rigid canopies. All the numerical predictions have been obtained considering the same nominal bulk Reynolds number (i.e. $Re_b = U_b H/\nu = 6000$, $H$ being the open channel depth and $U_b$ the bulk velocity). We used the methodology described in §2.3 to tackle the canopy flows. Four canopy configurations have been considered. All of them share the same in-plane solid fraction while the canopy to channel height ratios have been selected within the range $h/H = [0.05, 0.4]$. The lowest and the highest values lead to flow conditions approaching the two asymptotic states that in literature are usually termed as *sparse* and *dense* regimes (see Nepf, 2012a). The other two $h/H$ selected ratios are representative of *transitional* regimes, a generic category that incorporates all the non-asymptotic states. While the interaction of a turbulent flow with a filamentous canopy in the two asymptotic conditions is relatively well understood, not much is known on the transitional flows and on the physical mechanisms that are responsible for the variations of flow regimes when the canopy solidity is changed.

The aim of this work has concerned the exploration of the effect of the canopy solidity on the intra-canopy flow, on the outer flow and on their mutual interaction. We will also provide clear evidence on the key role played by the relative positions of the mean profile inflection points and the location of the wall origin (origin seen from the outer flow). Indeed, the relative locations of these points ultimately determine the flow structure that results from the interaction between the outer turbulence and the canopy layer. The work also seeks to unravel the appropriate scales that govern the canopy flows. Thus, new phenomenological models will be proposed based on the universality of the flow found. In fact, de-

spite the proliferation of canopy-flow models (Bailey and Stoll, 2013, Nepf, 2012a, Poggi et al., 2004, Raupach et al., 1996), the identification of the dominant velocity and length scales in different canopy-flow regimes is still an open research topic. In particular, the insurgence of different intra-canopy flows at intermediate flow regimes is still not well understood. In this *transitional* regime, the outer structure can deeply penetrate in the bed-normal direction and the *long* stems redistribute the outer momentum that rushes normally into the canopy into in-plane, small scale motions. At the same time, the presence of the Kelvin-Helmholtz generated spanwise vorticity rollers, their modification by the outer flow structures and their role in redistributing the local momentum (Monti et al., 2019) are features that in the past have not been investigated in-depth.

The Chapter is organised as follows. In §4.1, we will briefly report the information on the simulations carried out, while in §4.2, we will describe and analyse the obtained results, focusing on the statistical analysis and then identifying the structures that populate the flows. Finally, some conclusions will be drawn in §4.3.

## 4.1 Numerical set-up

The solver tackles the LES governing equations (2.66) using a second order accurate, cell centred finite volume approach described in Chapter 2. To distribute the stems on the bottom wall, we subdivided the latter in a Cartesian mesh of uniform squares of area $\Delta S^2$ (see Figure 1.2). Each filament was attached orthogonally to each squared tile, with its local positioning determined according to a uniform random distribution (see Figure 2.11). We decided to use a stem random assignment to minimise channelling effects within the canopy, i.e. preferential flow corridors in an aligned positioning, or repeating, ordered flow patterns as in a staggered configuration. The tile size and the filament height $h$ can be adjusted to match any solidity value $\lambda$, that for stems of uniform cross-sectional area (i.e. constant stem diameter $d$ ) is defined as

$$\lambda = \frac{d}{\Delta S}\frac{h}{\Delta S}. \tag{4.1}$$

In particular, by keeping constant the tiles and the stems cross-sectional areas while varying the height of the canopy (i.e. of each stem), we selected four solidity values $\lambda$, that would nominally lead to different canopy-flow-regimes (Nepf, 2012a), as detailed in table 4.1. For all the four cases, the computational box size, made dimensionless with the open channel height $H$ is $L_x/H = 2\pi$, $L_y/H = 1$ and $L_z/H = 3/2\pi$ (a size similar to the one used by Bailey and Stoll (2013) for the case of a nominally dense canopy flow regime). The numerical domain is set to be periodic in both the stream- (i.e., $x$) and the spanwise (i.e., $z$) directions.

| Case | Canopy height $h/H$ | Solidity $\lambda$ | Nominal Regime |
|---|---|---|---|
| *MS* | 0.05 | 0.07 | *marginally sparse* |
| *TR* | 0.10 | 0.14 | *transitional* |
| *MD* | 0.25 | 0.35 | *marginally dense* |
| *DE* | 0.40 | 0.56 | *dense* |

Table 4.1: Considered canopy configuations: canopy solidity and corresponding nominal regimes (Nepf, 2012a).

The choice of selecting a streamwise periodic condition, even for the densest case, has been motivated by the experiments of Ghisalberti and Nepf (2004). Although they observed the presence of a mixing-layer developing at the canopy edge, they also suggested that its thickness was independent of the streamwise location. At the bottom wall, i.e. the canopy bed, a zero-velocity boundary condition is imposed. Conversely, to model an open channel flow condition, a free slip condition, i.e. (2.61), is set at the top surface (see Figure 2.10 for a sketch of the domain). The four simulations have been carried out using a Cartesian grid with a uniform distribution in the $x$ and $z$ directions, and with a mildly stretched distribution of the nodes in the bed-normal direction. While the grid on each $x-z$ plane has been kept the same for the four simulations, the wall-normal distribution has been adjusted to adapt to the variations of the height of the stems. The number of nodes in the $x$ and $z$ directions is set to $ni = 576$ and $nk = 432$, respectively. In the $y$-direction, the number of grid points ranges from a minimum value of $nj = 180$, for the sparse (*MS*) case, to a maximum of $nj = 340$ for the densest canopy (*DE*). With this choice, the $x$ and $z$ spacings in wall units inside the canopy are kept below 3, i.e. $\Delta x^+_{in} = \Delta x \cdot u_{\tau_{in}}/\nu \leq 3$ and $\Delta z^+_{in} = \Delta x^+_{in} \leq 3$ (note that $u_{\tau_{in}} = \sqrt{\tau_w/\rho}$, where $\tau_w$ is the wall shear stress at the bed, i.e. at $y = 0$). In the portion of the flow outside the canopy, the $x$ and $z$ spacings verify the inequalities $\Delta x^+_{out} = \Delta x \cdot u_{\tau_{out}}/\nu \leq 11$ and $\Delta z^+_{out} = \Delta x^+_{out} \leq 11$, thus well within literature values (Kim et al., 1987). Here $u_{\tau_{out}}$ is a *friction velocity* determined using the total stress in the $y$ location corresponding with the origin of the outer logarithmic boundary layer (further explanations are provided in §3.2 and in the next section). Concerning the grid spacings along the $y$-direction, two tangent hyperbolic distributions have been used inside and outside the canopy ensuring that the ratio between neighbouring cells in the interval $[0, h] \cup [h, H]$ is kept below 4%. Table 4.2 summarises the adopted $y-$spacings inside and outside the canopy. Further discussion on the suitability of the numerical scheme and on the adopted resolution inside and outside the canopy can be found in §2.3.4.

Finally, concerning the global channel flow equilibrium, a uniform pressure gradient is applied in the streamwise direction. In particular, at each time step, the mean streamwise pressure gradient is adjusted to fix the volumetric flow rate

| Case | Spacing at $y = 0$ | Spacing at $y = h$ | Spacing at $y = H$ |
|---|---|---|---|
| *MS* | $\Delta y = 10^{-3}\ H$ | $\Delta y = 7.0 \times 10^{-4}\ H$ | $\Delta y = 3.2 \times 10^{-2}\ H$ |
| *TR* | $\Delta y = 10^{-3}\ H$ | $\Delta y = 5.0 \times 10^{-4}\ H$ | $\Delta y = 2.0 \times 10^{-2}\ H$ |
| *MD* | $\Delta y = 10^{-3}\ H$ | $\Delta y = 3.0 \times 10^{-4}\ H$ | $\Delta y = 2.3 \times 10^{-2}\ H$ |
| *DE* | $\Delta y = 10^{-3}\ H$ | $\Delta y = 2.5 \times 10^{-4}\ H$ | $\Delta y = 2.0 \times 10^{-2}\ H$ |

Table 4.2: Details on the nodes distribution in the wall normal direction for the four simulated canopies. Note that for cases *MS* and *TR* the $\max(\Delta y_{j+1}/\Delta y_j) \leq 1.03,\ \forall j$, while for cases *MD* and *DE* the $\max(\Delta y_{j+1}/\Delta y_j) \leq 1.04,\ \forall j$.

to a constant value leading to a bulk Reynolds number of $Re_b = U_b\ H/\nu = 6000$ (being $U_b$ the bulk velocity of the flow, defined as in (2.67)) very close to the one used in the experimental work of Ghisalberti and Nepf (2004).

Each simulation ran for about 2000 hours on 96 processors of the Cray XC30 (Phase 2) supercomputer of ARCHER, the UK National Supercomputing Service.

## 4.2 Results

To shed some light on the physical mechanisms that are responsible for generating different flow regimes when varying the solidity $\lambda$ of a canopy as defined in (4.1), we have considered the four cases detailed in Table 4.1. As already mentioned, the four different values of $\lambda$ are attained by varying the canopy height while keeping constant both the ratio between the filament diameter and the size of the tile occupied by each stem. In particular, in (4.1) we have set $\Delta S/d \approx 5.5$.

### 4.2.1 Mean velocity profiles

We start by considering the effect of $\lambda$ on the mean velocity profiles. In a non-sparse regime (i.e., $\lambda > 0.04$), the mean velocity profile of a turbulent canopy flow is known to exhibit two inflection points (Nepf, 2012a, Poggi et al., 2004), one at the edge of the canopy and the other closer to the wall. The mean velocity profiles obtained for the four considered $\lambda$ values, shown in Figure 4.1, exhibit the aforementioned pair of inflection points. The inflection point at the canopy edge is due to the drag discontinuity arising as a consequence of the sudden end of the stems, while the inner inflection point is a result of the merging of the linear, close-to-the-bed velocity profile with the convex shape of the mean velocity distribution at the canopy tip. The location of the inflection points can be determined by computing the zeros of the average, streamwise momentum

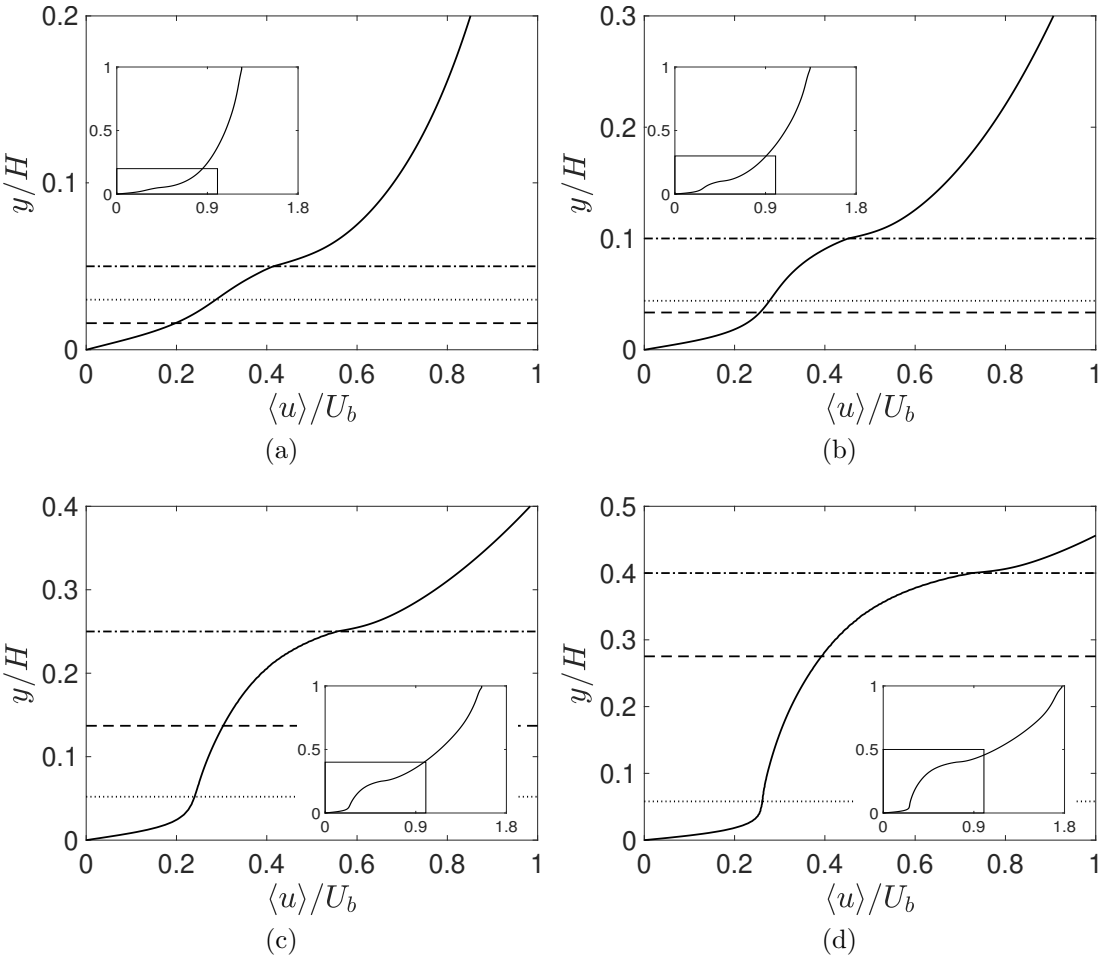


Figure 4.1: Mean velocity profiles for the four cases. The inset in each plot shows an enlarged view. The profiles are ordered left to right, top to bottom according to the $\lambda$ value of each case: (a) *MS* ($\lambda = 0.07$ and $h/H = 0.05$); (b) *TR* ($\lambda = 0.14$ and $h/H = 0.10$); (c) *MD* ($\lambda = 0.35$ and $h/H = 0.25$); (d) *DE* ($\lambda = 0.56$ and $h/H = 0.40$). The three lines parallel to the bed indicate: the location of the first inflection point (dotted line), the location of the virtual origin (dashed line) and the location of the canopy height, i.e. the second inflection point (dash-dotted line).

balance,

$$\frac{1}{Re_b}\frac{\mathrm{d}^2\langle u\rangle}{\mathrm{d}y^2} = \frac{\partial P}{\partial x} + \frac{\mathrm{d}\langle u'v'\rangle}{\mathrm{d}y} + \langle D\rangle. \tag{4.2}$$

In the above equation, the symbol $\langle \quad \rangle$ denotes the triple average operator obtained by taking the mean values in time and along the two homogeneous spatial directions, $x$ and $z$. The first term of (4.2) represents the mean viscous force, the second the mean pressure gradient, the third the mean Reynolds stresses and the last one keeps into account the global mean drag offered by the canopy stems which is discontinuous at $y = h/H$. The two inflection points enclose a *transitional* zone, where a mixing-layer-like flow develops between the innermost and outermost boundary layers (Poggi et al., 2004). Along the wall-normal direction, the origins of these two boundary layers are located at the solid wall and just below the canopy tip, respectively. The wall location seen by the outer flow, $y_{vo}$, representing the position of the *virtual origin* of the boundary layer developing above the canopy, is determined by enforcing the mean outer flow to take on a canonical logarithmic shape,

$$\langle u\rangle = \frac{u_{\tau,out}}{\kappa}\log\left(\frac{(y-y_{vo})u_{\tau,out}}{\nu}\right) + B. \tag{4.3}$$

The above is one of the standard modifications of the boundary layer *log laws* for flows over rough surfaces (Jiménez, 2004). In (4.3) $\kappa$ is the von Kármań constant (e.g. $\kappa \in [0.37, 0.42]$), $B$ a parameter that depends on the roughness of the wall surface ($B = 5.2$ for a smooth surface) and $u_\tau$ is the friction velocity computed using the value of the total stress at the virtual origin $y_{vo}$, i.e. $u_{\tau,out} = (\tau(y_{vo})/\rho)^{1/2}$, being

$$\tau(y_{vo}) = \mu\frac{\mathrm{d}\langle u\rangle}{\mathrm{d}y}\bigg|_{y=y_{vo}} - \rho\langle u'v'\rangle(y_{vo}). \tag{4.4}$$

The logarithmic law (4.3) represents an implicit equation that can be solved in $y_{vo}$ once the total stress profile is known (see also §3.2 for further details). The virtual origin of the external flow and the locations of the two inflection points of the mean velocity profile of a canopy flow in a *non-sparse* configuration, and particularly their mutual signed distances, constitute a signature of the actual canopy flow regime as they ultimately define the level and the nature of the interaction between the inner and the outer boundary layers. In particular, in our methodology, the canopy becomes sparser as its height $h$ is shortened leading to a shorter transition region that can be also interpreted as an increase in the size of the band where the internal and external boundary layers overlap. By further decreasing the canopy height, the virtual origin asymptotically moves towards the canopy bed and the two inflection points gradually merge and eventually disap-

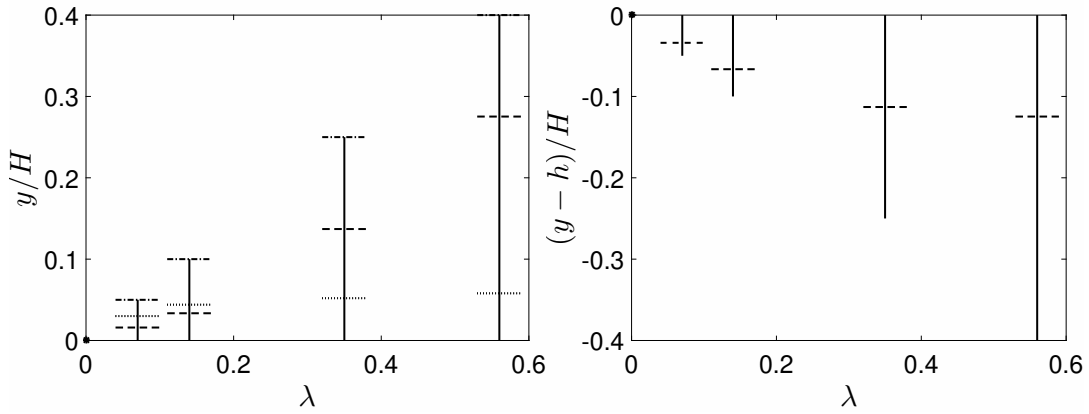


(a) (b)

Figure 4.2: (a) Mean locations of the two inflection points and of the virtual origin along the canopy stem (virtual origin: `---` ; inner inflection point: ·····; outer inflection point: `-·` ). (b) Location of the virtual origin in a reference system whose zero is set at the canopy tip. Note that the small dot on the left of the horizontal axis (bottom in (a) and top in (b)) represents a flow on a smooth surface (i.e. no-canopy).

pear by collapsing into a single location. This condition is typical of very sparse canopy regimes (i.e. $\lambda < 0.04$) or, more in general, of turbulent boundary layer flow over rough surfaces. Figure 4.2(a) shows the locations of the two inflection points and of the virtual origin found for the four $\lambda$ cases under consideration. Note that the location of the virtual origin has been determined by setting the von Kármán constant to the canonical value $\kappa = 0.41$ in (4.3) (selecting any other value within the range $0.37 \leq \kappa \leq 0.42$ gives a variation of the virtual origin within 5% of $h/H$, see Monti et al., 2019). As anticipated, Figure 4.2(a) shows that, as the height of the canopy (or, equivalently, $\lambda$) is reduced, the wall-normal location of the virtual origin moves closer to the wall and the innermost inflection point approaches the canopy edge where the outer inflection point is situated (i.e. at $y = h$). For the sparser cases that we have considered (i.e. the *MS* and *TR* cases of Table 4.1), the location of the virtual origin is below the close-to-the-bed inflection point indicating that the outer boundary layer has a strong interaction with the intra-canopy flow despite the fact that the values of $\lambda$ for the *MS* and the *TR* cases are above the sparse/dense threshold identified by Nepf (2012a). The above observation and, more in general, the variations of the distances of the two inflection points and of the virtual origin from the bed, caused by different values of $\lambda$ reported in Figure 4.2(a) suggest that a sharper and more stringent criterion to separate the flow regimes, in particular providing a lower bound for the inception of the dense regime, can be based on the signed distance between $y_{vo}$ and the

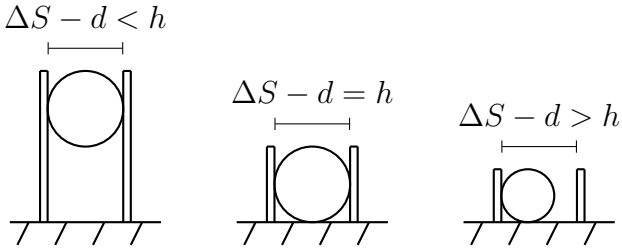


Figure 4.3: Sketch of the largest vortex size able to penetrate from the outer layer into the canopy. The vortex is represented as a circle with diameter $\Delta S - d$ or $h$.

coordinate of the inner inflection point. Figure 4.2(b) shows the variations of the distance between the virtual origin and the outer inflection point (i.e. the canopy tip). From the figure, it appears that $h - y_{vo}$ approaches a constant value as the canopy becomes denser (i.e. increasing the $\lambda$ value). This asymptotic saturation of the virtual origin location corresponds to a decoupling of the outer flow from the inner one: for large values of $\lambda$, the outer turbulent flow does not see a canopy but a rough wall with a roughness height that becomes progressively independent of an increasing $\lambda$ value.

A heuristic model able to explain the variations of the $y$ coordinates of the virtual origin and of the mean profile inflection points can be developed by considering the ratio of the size of the close-to-the-canopy, outer eddies and the geometric dimensions of the canopy. In particular, $(\Delta S - d)/h$ defines the magnitude of the in-plane canopy voids as compared to the canopy depth. If $\Delta S/h < 1$ (for slender canopies, $\Delta S/h >> d/h$), only vortices of diameter $\phi_{\text{eddy}} < O(\Delta S)$ will be able to fully penetrate the canopy. However, in this circumstance, the typical length scale close to the canopy tip is $\Delta S$ itself (by the stems tips, eddies are produced at a length scale comparable to their spacings) and therefore only eddies with a size $\simeq \Delta S$ can be hosted in-between the stems and the virtual origin of the outer flow will saturate close to the edge at a distance from the tip of $O(\Delta S)$ (see Figure 4.3 for a conceptual sketch). The given description is not very dissimilar from the *d-type* roughness scenario proposed by Perry et al. (1969) that envisaged a situation in which stable vortices forms in-between roughness elements. Conversely, if $\Delta S/h > 1$, the mean canopy separation $\Delta S$ will no more fix the allowed eddy size, and it will be the distance from the cores of the eddies to the bottom wall to determine how deep the outer eddies can *leak* into the canopy. In this condition, for sufficiently tall canopies, $y_{vo}$ becomes a function of $h/H$ (or $\lambda$), a situation that recalls a *k-type* roughness behaviour (Schultz and Flack, 2009). Using the heuristic argument explained above, we can estimate the value of the canopy height for which the virtual origin collapses into the innermost

inflectional point, i.e. when $\Delta S - d \simeq h$:

$$\frac{\Delta S - d}{h} \simeq 1 \;\rightarrow\; \frac{h}{H} \simeq (1 - 0.182)\,\frac{\Delta S}{H} \;\rightarrow\; \frac{h}{H} \simeq 0.1063 \;\rightarrow\; \lambda \simeq 0.15. \qquad (4.5)$$

In the above equation we have used the specific geometric data of the present simulation (i.e. $d \simeq 0.182\Delta S$, $\Delta S \simeq 0.13H$ and $\lambda = 0.14h/H$). The above estimate matches the numerical value corresponding to the crossing between $y_{vo}$ and the internal inflection point of Figure 4.2, showing that the simple argument used above can be used to predict the threshold $h/H$ value for *dense* canopies. Note that this value is also the value indicated by Schlichting (1936) to distinguish between the sparse and the dense $k-type$ roughness regimes. For values of $h/H$ exceeding the threshold value, the canopy becomes denser and the depth of the virtual origin saturates towards a value $\simeq \Delta S$. In these conditions, for large values of $h/\Delta S$, the outer and the internal boundary layers are almost decoupled with very weak interactions in-between them.

### 4.2.2 Statistical characterisation of the intra-canopy and of the outer flows

To identify the structure of the regions of a canopy flow, we start by considering the mean velocity profiles in semi-logarithmic axes, as shown in Figure 4.4. The profiles are made dimensionless using two different friction velocities inside and outside the canopy. In particular, for the inner boundary layer, the friction velocity is defined as $u_{\tau,in} = \sqrt{\tau_w/\rho}$, being $\tau_w$ the skin friction at the bottom wall at $y/H = 0$, while the external velocity profile is normalised with a different scale, $u_{\tau,out}$, computed using the total stress evaluated at the virtual origin $y_{vo}$ as in (4.4).

Figure 4.4 reveals that, close to the bed, the velocity profiles obtained with different values of $\lambda$ collapse together only in the viscous sublayer region where the wall friction dominates over the drag of the stems, independently of the canopy sparsity. Further away from the bed, the shape of the buffer layers is highly affected by the value of $\lambda$ that determines the importance of the local hydrodynamic effects versus the inrush of momentum from the outer layer. Unlike the intra-canopy flow, when the outer flow velocity profiles are scaled with $u_{\tau,out}$ and with the corresponding viscous length, $\delta_\nu = u_{\tau,out}/\nu$, a universal distribution following standard logarithmic profiles of boundary layers is recovered for all $\lambda$ values. The effect of the canopy sparsity is limited to the shift of the logarithmic layer revealing that, seen from the outer flow, the canopy simply acts as a rough wall with the equivalent surface elements height determined by the value of $\lambda$. In fact, the logarithmic law for a turbulent boundary layer over a rough wall can be

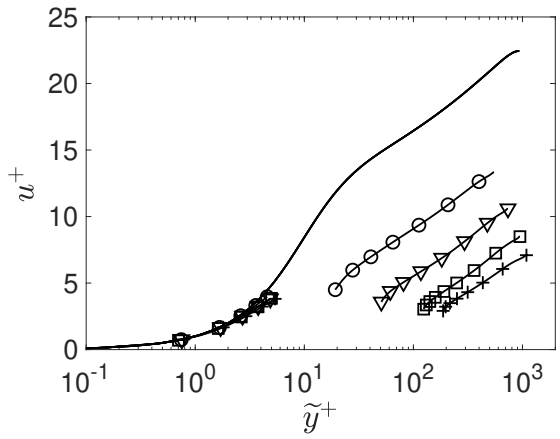


Figure 4.4: Mean velocity profiles normalised using both the inner wall units (below $y^+_{in} \simeq 4$) and the outer ones (above $y^+_{out} \simeq 10$). The abscissa $\widetilde{y}^+$ represents the wall-normal coordinate rescaled with the inner or outer wall units considering an origin located either on the canopy bed or at the virtual origin $y_{vo}$: i.e. $\widetilde{y}^+ = u_{\tau,in}y/\nu$ or $\widetilde{y}^+ = u_{\tau,out}(y - y_{vo})/\nu$, respectively. The solid black line without symbols refers to the profile of the plane channel flow at $Re_\tau = 950$ by Hoyas and Jiménez (2008). Symbols as in Table 4.1.

written as

$$U^+_{out} = \kappa^{-1} \log(y^+_{out}) + 5.5 - \Delta U^+_{out}, \tag{4.6}$$

where $\Delta U^+_{out}$, called *roughness function* (Hama, 1954, Jiménez, 2004, Perry et al., 1969), is a wall-offset that keeps into account the increased friction due to roughness. Figure 4.4 shows that the roughness function increases monotonically with the value of $\lambda$ (or, equivalently, with $h/H$). This behaviour is related with the previously discussed saturation of the location of the virtual origin for increasing $\lambda$ values that, in turns, determines the roughness solidity seen by the outer flow, i.e. $\lambda_{\text{eff}} = d\ (h - y_{vo})/\Delta S^2$. Apart from the roughness function $\Delta U^+$, the effect of the roughness on the mean flow can be measured by other, interchangeable quantities (Jiménez, 2004) such as the effective sand roughness $k_s$ (Nikuradse, 1933) defined via the modified log-law,

$$U^+_{out} = \kappa^{-1} \log\left(\frac{y-h}{k_s}\right) + 8.5. \tag{4.7}$$

From (4.6) and (4.7), we can express the roughness function $\Delta U^+_{out}$ as a function of $k_s$, i.e.

$$\Delta U^+_{out} = \kappa^{-1} \log\left(\frac{y - y_{vo}}{y-h} k^+_s\right) - 3. \tag{4.8}$$

By assuming that the outer turbulent flow sees the canopy as a rough wall, the

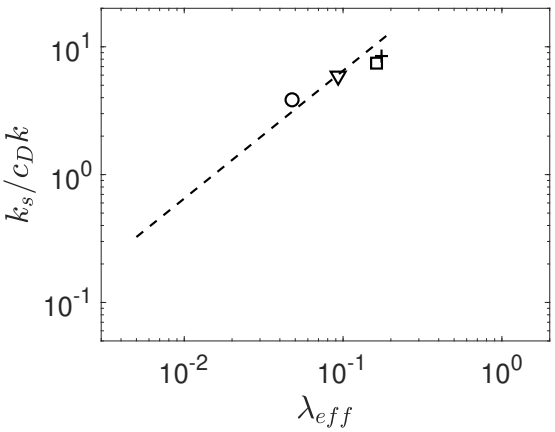


Figure 4.5: Equivalent sand roughness $k_s/k$ seen by the outer flows of the canopy versus the effective solidity $\lambda_{\text{eff}}$. As in Jiménez (2004, p.179, Figure 1a), $k_s/k$ has been corrected with the drag coefficients $C_D$ computed at the stem mid location where the local flow is unaffected by the ends. Symbols as in Table 4.1.The dash line represents a theoretical case for which $k_s/k \propto \lambda_{\text{eff}}$.

portion of the canopy that goes from the virtual origin to the canopy tip can be interpreted as a surface covered by cylindrical obstacles characterised by height,

$$k^+ = \frac{k u_{\tau,out}}{\nu} = \frac{(h - y_{vo}) u_{\tau,out}}{\nu}. \tag{4.9}$$

All the cases that we have considered are characterised by a value of $k^+ \gg 1$, a situation in which the elements drag dominates on the viscous one, i.e. *k-type* roughness (Jiménez, 2004). This type of roughness is characterised by two regimes defined by the functional relationship between the ratio $k_s/k$ and the solidity $\lambda_{\text{eff}}$ (Schlichting, 1936). For values of $\lambda_{\text{eff}} \lesssim 0.15$, $k_s/k$ linearly increases with $\lambda_{\text{eff}}$, while for $\lambda_{\text{eff}} \gtrsim 0.15$, $k_s/k$ decreases with $\lambda$ because the elements start shielding one another (Jiménez, 2004) (in particular $k_s/k \propto \lambda_{\text{eff}}^{-p}$, with $p \in [2, 5]$). Figure 4.5 shows the ratio $k_s/k$ as a function of $\lambda_{\text{eff}}$ for the four cases considered in this work. Note that the ratio $k_s/k$ has been corrected with a drag coefficient (here computed as a wall-normal average of $C_D(y)$ in the middle of the canopy region, obtained from the quadratic law of the drag). See also Figure 4.6 as reference, directly adapted from Figure 1 (a) of Jiménez (2004).

All the considered cases appear to belong to the *sparse–k-type* regime with the values corresponding to $h/H = 0.25$ and $h/H = 0.40$ in the range of the *sparse-dense* transition. Also note that, when $y_{vo}$ saturates, $h - y_{vo} \simeq h$ and $\lambda_{\text{eff}} \simeq \lambda$, thus, although the definition of dense and sparse canopies differs from the one used for the rough surface seen by the outer flow, when approaching the dense regime for the outer flow the separation value between rough regimes can

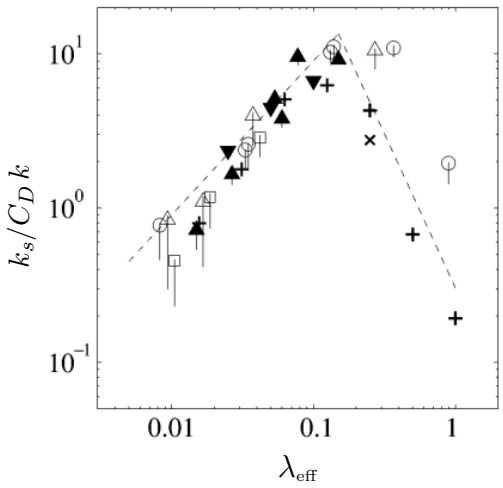


Figure 4.6: Equivalent sand roughness for various $k$-surfaces versus the solidity $\lambda_{\text{eff}}$, corrected with empirical drag coefficients $C_D$. Image adapted from Jiménez (2004, p.179, Figure 1 a). See Jiménez (2004) for further details on the symbols and $C_D$ adopted.

be inferred using indifferently $\lambda \simeq 0.15$ or $\lambda_{\text{eff}} \simeq 0.15$.

Next, we turn our attention to the comparison of the Reynolds stresses for the four canopies that we have considered. Before presenting the obtained distributions, we need to define velocity and length scales enabling a direct comparison between all the considered canopies. Concerning the selection of a velocity scale, we will use a local friction velocity, defined as

$$u_{\tau,l}(y) = \sqrt{\frac{\mu\, \mathrm{d}_y\langle u\rangle - \rho\,\langle u'v'\rangle}{\rho\,(1-y/H)}}, \tag{4.10}$$

that incorporates the effect of the mean drag exerted by the canopy on the flow (we also define an associated Reynolds number, $Re_{\tau,l}(y) = u_{\tau,l}(y)H/\nu$). The use of (4.10) to make the total stress nondimensional allows the latter to recover a linear distribution (Monti et al., 2019). The appropriateness of using a local friction velocity as a scaling factor has been previously appraised by Jiménez and co-workers for both smooth and manipulated walls (Jiménez, 2013, Tuerke and Jiménez, 2013). The well behaved scaling properties of (4.10) is also confirmed by the present results. In particular, Figure 4.7 shows a comparison between the diagonal Reynolds stresses normalised with the external friction velocity $u_{\tau,out}$ obtained using the total stress at the virtual origin (4.4), as opposed to the ones obtained non-dimensionalising with the local friction velocity defined in (4.10). The panels on the left column of Figure 4.7 clearly show that the diagonal Reynolds stresses obtained for different values of $\lambda$ do not collapse within the canopy with

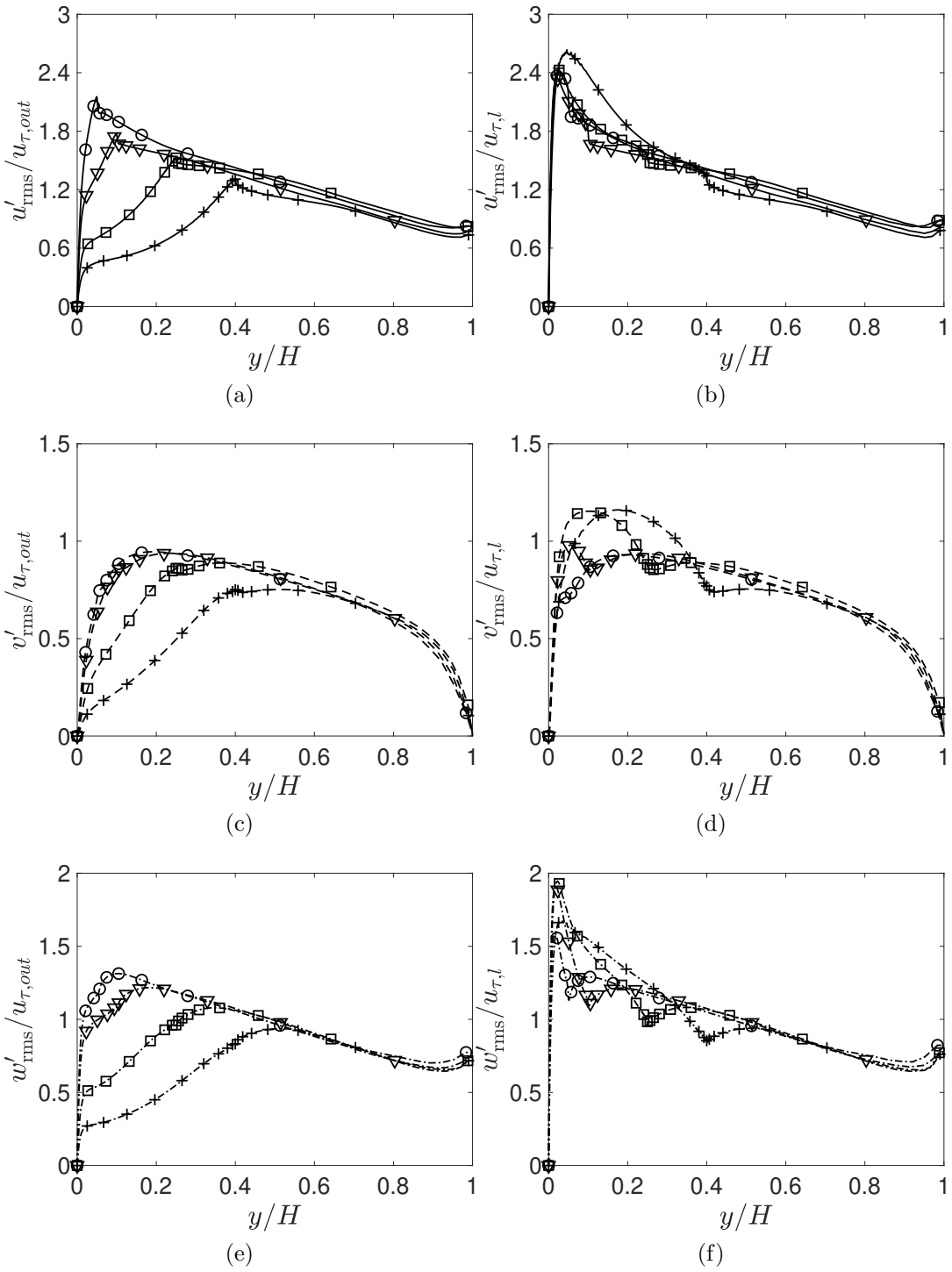


Figure 4.7: Diagonal Reynolds stresses distributions versus the wall normal, external coordinate $y/H$: panels (a) and (b): streamwise component; panels (c) and (d): wall-normal component; panels (e) and (f): spanwise component. The distributions on the left panels are made non-dimensional with the friction velocity computed at the virtual origin, $u_{\tau,out}$, whilst the distributions in the right panels are rescaled with the local friction velocity $u_{\tau,l}$ (4.10). Symbols as in Table 4.1; line styles are: —— $u'_{rms}$; - - - - $v'_{rms}$ and -·-·-· $w'_{rms}$.

the value of the maxima that clearly decreases monotonically as the density of the canopy is increased. The alternative scaling (4.10), used in the panels of the right column shows how the systematic decrease of the peak values of the stresses was basically due to the mean drag contribution. In fact, when the latter is kept into account using the local friction velocity (4.10), the distribution of the diagonal Reynolds stresses show a quite different behaviour: the distribution of the two sparser cases almost collapse for all three components, the peak of the streamwise component increases in the two denser case, the maximum of the wall-normal fluctuations increases in the two denser cases while the spanwise fluctuations show a different behaviour decreasing in the denser cases. Concerning the choice of the length scale, we have considered an outer and an inner scaling. The former uses the external length scale (in our case, the depth of the open channel $H$), the latter employs an inner scale in the order of the viscous length $\delta_\nu = \nu/u_\tau$. The appropriateness of $H$ as a length scale for the outer flow is clearly visible in Figure 4.7 that shows a collapse of all the diagonal stresses distributions for $y/H$ coordinates moving away from the canopy, independently of the choice of the velocity scale. A detailed comparison of the distribution of the velocity fluctuations is shown in Figure 4.8, where reference data from the plane channel flow (smooth walls) of Hoyas and Jiménez (2008) at $Re_\tau = 950$ have also been included (note that the curves do not match when $y/H \to 1$ since we are comparing an open channel flow with half of the domain of full plane channel flows). The marginal difference in the distribution of the diagonal Reynolds stresses far from the wall between a rough and a smooth wall was also highlighted by Scotti (2006), that analysed the flow over a set of transitional, *k-rough* surfaces. Concerning the most relevant internal length scale, the choice is between several possibilities since the filamentous layer covering the bed introduces several geometrical and physical scales, e.g. the height, $h$, and the diameter of the stems, $d$, the average separation between them, $\Delta S$, the location of the mean velocity profile's inflection points and the location of the virtual origin for the outer flow, $y_{vo}$. In an attempt to find a length scale delivering a unified behaviour, we introduce a *scaled viscous unit*, $y^+_\alpha$, defined using the localised friction velocity (4.10) and a *stretching* factor $\alpha$:

$$y^+_\alpha = \frac{1}{\alpha}\frac{u_{\tau,l}y}{\nu}. \tag{4.11}$$

The role of $\alpha$ in the above definition is to adapt the scaling to conditions that depend on the sparsity of the canopy (i.e. on the eventual saturation of length scales that depend on the value of the solidity $\lambda$). Figure 4.9(a) reveals that in denser canopies the stretching factor should be set to the nondimensional canopy height, $h/H$, meaning that the nondimensional wall-normal location should read as

$$y^+_h = \frac{u_{\tau,l}y}{\nu}\frac{H}{h} = \frac{y}{h}Re_{\tau,l}. \tag{4.12}$$

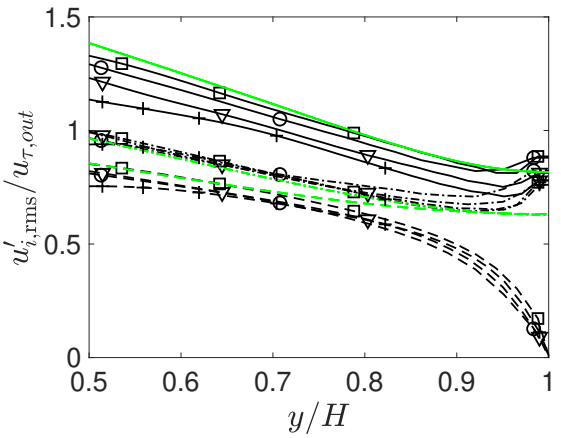


Figure 4.8: Wall-normal distribution of the diagonal Reynolds stresses in the outer region (i.e. above the canopy) made dimensionless with the outer friction velocity $u_{\tau,out}$ as a function of the wall-normal coordinate $y/H$. Line styles as in Figure 4.7 and open symbols as in Table 4.1. The green lines refer to the diagonal Reynolds stresses of a channel flow over a smooth wall at $Re_\tau = 950$ (Hoyas and Jiménez, 2008).

Thus, overall, for dense canopies (e.g. cases *MD* and *DE*), the normal coordinates should be made dimensionless considering two decoupled regions as the intra-canopy and outer flows asymptotically converge towards two independent wall flows bounded by surfaces located at the bed and at $y_{vo}$, respectively. Eventually, the two flows share a small overlapping region of thickness $h - y_{vo}$ where they interact. For sparser canopies, e.g. cases *MS* and *TR*, Figure 4.9(b) suggests that an appropriate value for the stretching factor $\alpha$ could be the average stem-to-stem spacing $\Delta S/H$. With this choice, the dimensionless wall-normal coordinates read as

$$y^+_{\Delta S} = \frac{u_{\tau,l} y}{\nu} \frac{H}{\Delta S} = \frac{y}{\Delta S} Re_{\tau,l}. \tag{4.13}$$

Although in this work we did not consider the effects of the variations of in-plane density (i.e. $\Delta S$), in view of the previously exposed conceptual model and previous works on *k-type* roughness (Leonardi et al., 2007), it seems physically sound to assume that it is the ratio $\Delta S/h$ that sets the size of the eddies that can penetrate the canopy in sparse regimes. Figure 4.9 also shows that the intermediate case *MD*, where $h/H = 0.25$, exhibits a consistent profile independently of the chosen $\alpha$ factor, possibly because of the transitional nature of this specific case. As a further confirmation of the validity of the proposed scalings, in Figure 4.9(c) we present the wall-normal distribution of the viscous and Reynolds shear stresses (made dimensionless with $\rho u^2_{\tau,l}$) versus the nondimensional coordinate $y^+_\alpha$ defined in (4.11). Choosing the values of $\alpha$ defined above for the denser and sparser cases, we obtain a good collapse for all the distributions.

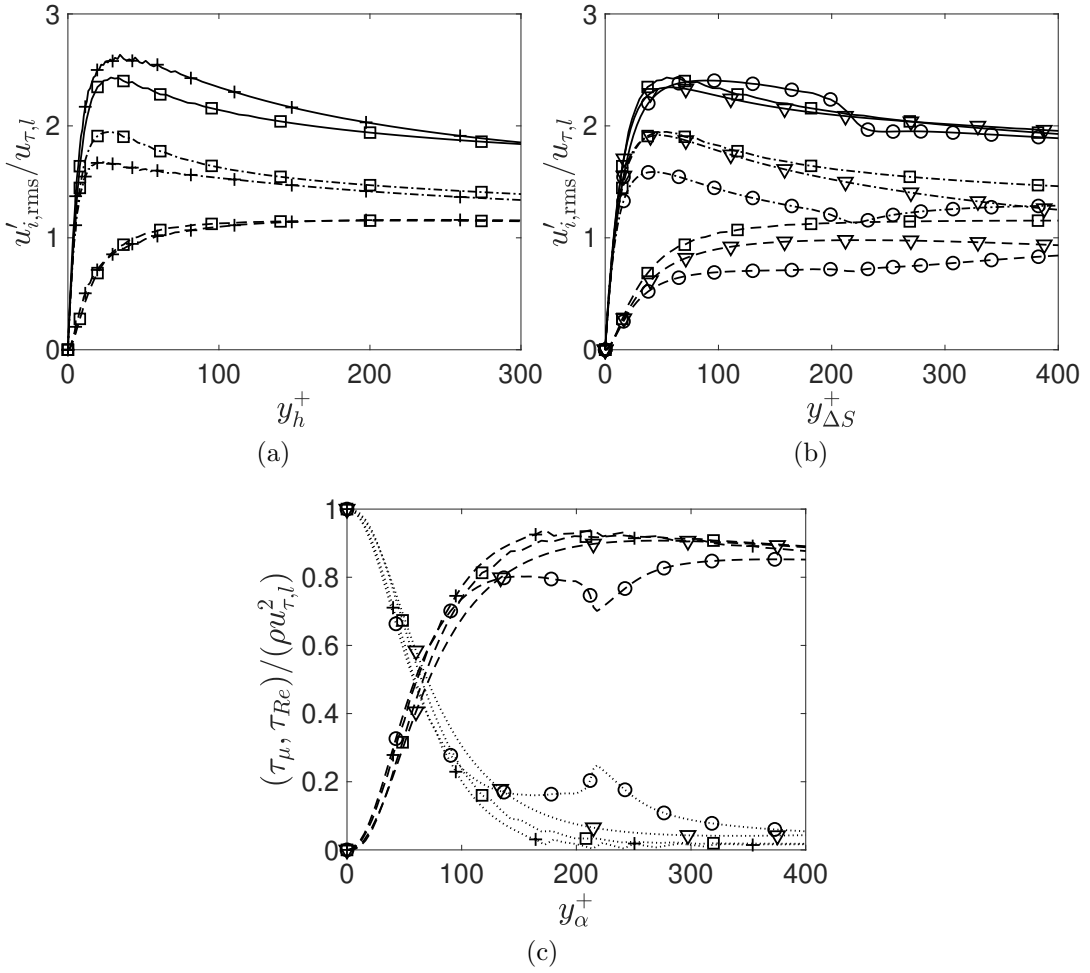


Figure 4.9: (a) and (b). Wall-normal distributions of the diagonal Reynolds stresses within the intra-canopy region. The stresses are made dimensionless using the local friction velocity $u_{\tau,l}$, defined in (4.10). In (a) only the dense cases *MD* and *DE* are represented using as a wall-normal coordinate the non-dimensional variable $y_h^+$, defined in (4.12). In (b) the distributions are shown for the sparse cases (*MS* and *TR*) and for the marginally dense case *MD* using as a wall-normal coordinate the dimensionless variable $y_{\Delta S}^+$ defined in (4.13). (c) Wall-normal distributions of the viscous ····· and of the Reynolds shear stresses - - - - . made dimensionless with the local shear $\rho u_{\tau,l}^2$. The wall-normal coordinate corresponds to the non-dimensional variable $y_\alpha^+$, as in (4.11), with $\alpha = h/H$ for the denser cases *MD* and *DE*, and $\alpha = \Delta S/H$ for the sparser cases *MS* and *TR*. For all panels, symbols as in Table 4.1 and line-styles as in Figure 4.7.

We close the discussion on the mean behaviour of the considered canopy flows by providing a brief, comparative analysis of the distribution of the velocity fluctuations. Further analysis of the contribution of the flow structures on the genesis of the fluctuations will be provided in the next section. Figure 4.9 shows that the maxima of the streamwise velocity fluctuations decrease as the canopy sparsity is increased and that the most sparse case *MS* is characterised by an iso-valued distribution spanning almost all the canopy. This behaviour is consistent with the alternating presence of the stems that locally decelerate the flow driven by the imposed pressure gradient. Clearly, the value of $\lambda$ determines the intensity of the stems blockage effect that becomes weaker for sparser conditions. Concerning the wall-normal component of the Reynolds stresses, it is observed that the two denser cases *DE* and *MD* present a wall-normal distribution that substantially does not differ from the one of a standard channel flow (see for example Hoyas and Jiménez, 2008). This behaviour is easily understood by noticing that denser canopies can be regarded as porous media with a high wall-normal permeability that does not hinder sweeps and ejections from and towards the outer flow to take place in a medium bounded by a *distant*, impermeable bed. The sparser cases show a different behaviour with the wall-normal velocity fluctuations decreasing when the solidity is decreased and the impermeability condition becoming more influential for the outer flow. Concerning the spanwise velocity fluctuations, a nonmonotonic behaviour when the value of $\lambda$ is decreased is noticed. In particular, we notice an overall increase in $\langle w'w' \rangle$ when moving from the *DE* to the *MD* case, an almost unchanged distribution for the transitional cases *MD* and *TR*, and a final decrease in the *MS* case. The increase in the spanwise velocity fluctuations observed in the transitional cases, *MD* and *TR*, have been explained by Monti et al. (2019) in terms of spanwise deviations of the intra-canopy flow that preferentially penetrates the layer through wall-normal sweeps and ejections generated by the dynamics of the outer, logarithmic layer structures.

### 4.2.3 The structures of the canopy flows

Further insight on the emergence and on the organisation of the large coherent structures that characterise the various flow regimes when different solidities are considered can be obtained by looking at the spectral energy content of the fluctuations of the velocity components.

We start by considering Figure 4.10 that shows the magnitude of the one-dimensional premultiplied cospectra of the Reynolds shear stress, $|\kappa_x \Phi_{u'v'}/u^2_{\tau,l}|$ (or $|\kappa_z \Phi_{u'v'}/u^2_{\tau,l}|$, where $u_{\tau,l}(y)$ is the local friction velocity defined in (4.10)), as a function of the distance from the bed and of the streamwise (top row) and the spanwise (bottom row) wavelengths. Each row incorporates four panels corresponding to the cospectra that have been obtained by increasing the $\lambda$ values. In this figure and in the premultiplied spectra of the velocity fluctuations (to

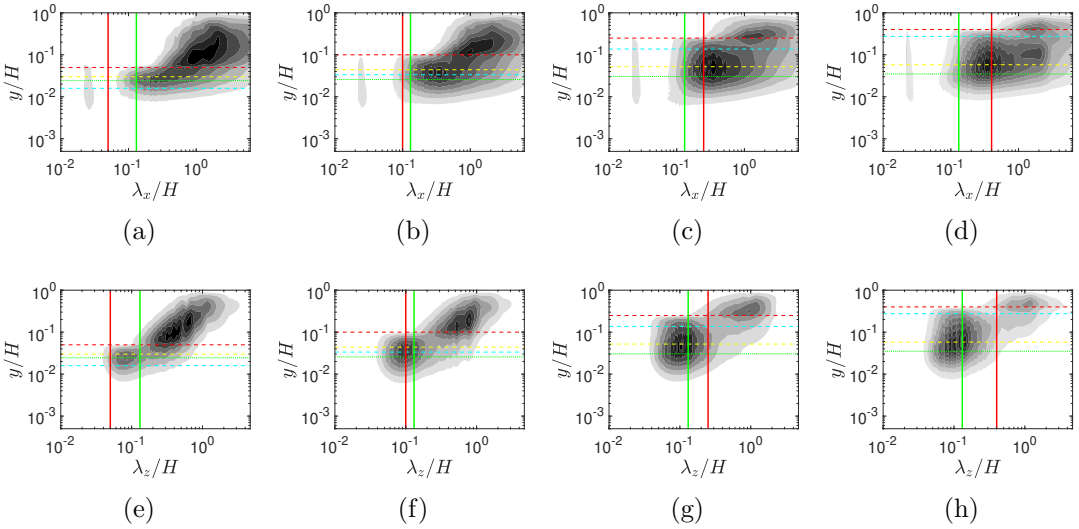


Figure 4.10: Magnitude of the premultiplied cospectra of the streamwise and spanwise velocity fluctuations $u'$ and $v'$ as a function of the wall-normal coordinates in outer units. Panels (a) to (d) refer to the dependence form the streamwise wavelengths (in outer units) for increasing values of $\lambda$ (i.e., $\lambda = 0.07,\ 0.14,\ 0.35$ and $0.56$); contour levels range in the interval $[0, 0.4]$ with an increment of $0.02$. Panels (e) to (h) refer to the spanwise wavelengths for the same increasing set of $\lambda$ values; contours extracted in the $[0, 0.5]$ range with an increment of $0.05$. Vertical solid lines: red is $h/H$, green is $\Delta S/H$. Horizontal dashed lines: yellow is the location of the inner inflection point, red is the canopy height (outer inflection point), cyan is the location of the virtual origin; the green dotted line is the location of maximum curvature of the mean velocity profile.

be presented later), the wavelengths and wall-normal distances have been made nondimensional with the open channel height, $H$. Both the cospectra and premultiplied spectra have been plotted using *log-log* axes to facilitate the interpretation of the results within the intra-canopy region.

Observing the cospectra of Figure 4.10 obtained for different solidities, we notice that all of them present at least two distinct peaks whose locations move towards the $y$ coordinates of the two inflection points of the mean velocity profile (yellow and red horizontal, dashed lines in every subfigure) as $\lambda$ is increased. More precisely, the outer peak approaches asymptotically the tip of the canopy for increasingly dense conditions with the associated streamwise and spanwise wavelengths of sizes $O(H)$. Since $\langle u'v' \rangle$ is a good indicator of spanwise-oriented coherent structures, the outer peak suggests the presence of a set of rollers centred at the canopy tip. Their presence is confirmed by visual inspection of the streamlines plotted on the $x$–$y$ side of the computational boxes of the four considered cases in Figure 4.11 (streamlines obtained by spanwise averaging an instantaneous realisation of the $u'$ and $v'$ velocity components). The appearance of spanwise oriented rollers is a ubiquitous feature of many flow fields over textured surfaces that induce an inflection point in the mean velocity profile, e.g. flow over canopies, see Nepf (2012a) or Finnigan et al. (2009), or porous and ribbleted walls, see Jiménez et al. (2001) and García-Mayoral and Jiménez (2011). In our case, the outer inflection point is generated by the discontinuous drag imposed by the canopy on the mean flow at its tip. As observed by other authors, the resulting scenario resembles the one of a plane mixing-layer (Finnigan, 2000, Nepf, 2012a, Raupach et al., 1996) sharing with it also the appearance of a system of spanwise rollers that form as a consequence of a Kelvin-Helmholtz instability. The streamwise wavelength $\Lambda_x$ associated with these rollers in dense canopy flows (i.e. $\lambda \gg 0.1$) has been found to be within the range $7 < \Lambda_x/L_s < 10$ (Raupach et al., 1996), where $L_s$ is a measure of the vorticity thickness above the canopy tip,

$$L_s = \frac{\langle u \rangle_{tip}}{\partial_y \langle u \rangle_{tip}} = \frac{1}{2}\delta_\omega. \tag{4.14}$$

Raupach et al. (1996), after analysing data from several experiments on dense canopy flows, provided a sharper estimate as $\Lambda_x = 8.1L_s$. In Figure 4.12, we compare this last estimate of $\Lambda_x$ with the one computed in our canopy flows associated with the outer peaks of Figure 4.10, as a function of the shear length, $L_s$. Clearly, the estimate provided by Raupach et al. (1996) holds only for the two denser scenarios while for the two sparser canopies *MS* and *TR* the correlation is not verified showing a linear relation $\Lambda_x = 19.5L_s - 4$. A possible explanation for this inconsistency can be attributed to the fact that the mean velocity in the inner canopy region can no more be neglected and that (4.14) is no more a valid estimate of the vorticity thickness above the canopy.

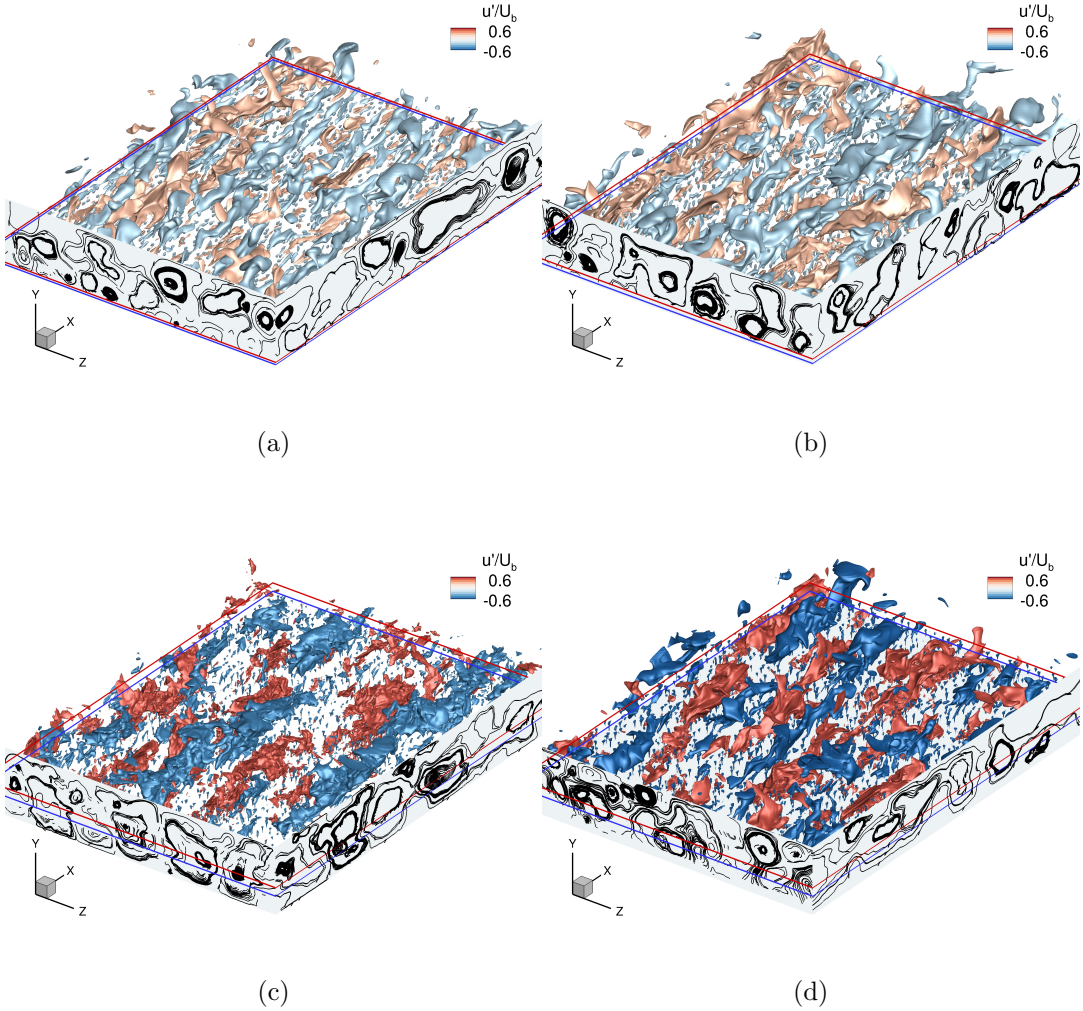


Figure 4.11: Instantaneous isosurfaces of streamwise velocity fluctuations. The streamlines drawn on the lateral sides have been obtained by averaging the instantaneous velocity fluctuations along the normal to the considered faces: the spanwise direction ($\langle u \rangle_z$, $\langle v \rangle_z$) for the left lateral side and the streamwise direction ($\langle v \rangle_x$, $\langle w \rangle_x$) for the frontal face. (a), (b), (c) and (d) correspond to the cases *MS*, *TR*, *MD* and *DE* respectively. The plane indicated with the red lines corresponds to the tip of the canopy, while the blue line indicates the plane at a distance $y_{vo}$ from the bed.

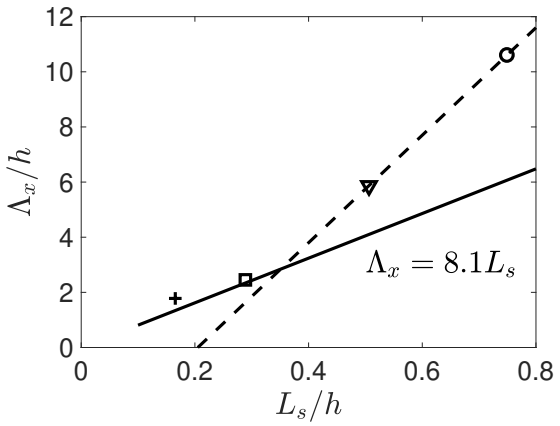


Figure 4.12: Streamwise wavelength $\Lambda_x$ of the large coherent motions triggered by the Kelvin-Helmholtz instability versus the shear length $L_s$. The solid line represents $\Lambda_x = 8.1L_s$ (Raupach et al., 1996), whilst the dashed line represents $\Lambda_x = 19.5L_s - 4$. Symbols as in Table 4.1.

Concerning the inner peak of the $\langle u'v' \rangle$ cospectra, it is noticed that its wall-normal location matches the position of the inner inflection point for all the considered $\lambda$ values and that for increasing values of the canopy solidity the interior maxima correspond to modes with $\lambda_x/H \simeq h/H$ and $\lambda_z/H \simeq \Delta S/H$. From Figure 4.13 showing the mean velocity profile inside the canopy, it is also noticed that the Fjørtoft's criterion (i.e. a necessary condition for an inviscid flow instability), given by

$$\partial_{yy}\langle u \rangle(y) \left[ \langle u \rangle(y) - \langle u \rangle(y_s) \right] < 0, \tag{4.15}$$

for any point $y$ in the neighbourhood of the inflection point $y_s$, is satisfied at the interior inflection point (see panel (b) of Figure 4.13) of the mean velocity profile (Drazin and Reid, 1981), thus leading to the conjecture that the inner peak in the cospectra of $\langle u'v' \rangle$ is related to a shear instability inside the canopy.

A series of snapshots offering a visual clue on the structure of the velocity field inside the canopy is provided in Figure 4.14. Although these snapshots only concern $x - z$ planes for case *DE*, it clearly appears that the velocity fluctuations at the location of the inner inflection point do not seem to inherit the same organised pattern visible in planes that are further away from the wall suggesting that a different mechanism is operating in this region.

To clarify the general structure of the velocity fields and its variations when different solidity values are considered, next we turn our attention to the pre-multiplied spectra of the velocity fluctuations. In particular, in Figure 4.15 we present the spectra associated with the fluctuations of the three velocity components as a function of the streamwise wavelength and the distance from the

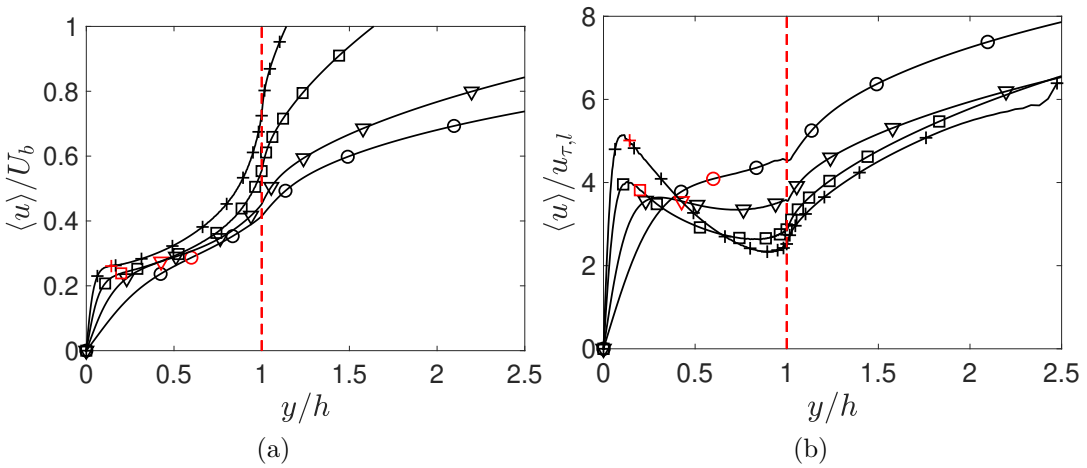


Figure 4.13: Mean velocity profiles for the four cases normalised with the bulk velocity in panel (a) and the local friction velocity in panel (b), as functions of the distance from the wall normalised with the canopy height $h$. The red markers indicate the locations of the inflection point closer to the solid wall, while the red dashed line indicates the location of the canopy edge. Symbols as in Table 4.1.

bed. Figure 4.16 shows the spectra as a function of the spanwise wavelength instead. These two figures are organised as a $4 \times 3$ matrix of panels in which each panel $(i, j)$ represents the spectra of the fluctuations associated to the $j$th velocity component and the $i$th solidity value (i.e. $\lambda_{i=1,\cdots,4} = [0.07, 0.14, 0.35, 0.56]$).

All the spectra of Figures 4.15 and 4.16 share the presence of a peak located outside the canopy. In particular, the streamwise velocity fluctuations show a clear external peak above the canopy tip characterised by a very long streamwise wavelength associated with a large scale modulation in the spanwise direction. These outer, large scale, streamwise velocity structures take on the shape of elongated velocity streaks typical of the logarithmic region of wall-bounded flows (Jiménez, 2018). The $u'$ premultiplied spectra, obtained for different $\lambda$ values, clearly indicate that the coherence length of these streaks scales in outer units. The presence of these large velocity streaks is also visually confirmed by the streamwise isosurfaces of the snapshots of Figure 4.11. By looking at the $y$–$z$ sides of the computational boxes of the snapshots of the four considered cases in Figure 4.11 (streamlines obtained by streamwise averaging an instantaneous realisation of the $v'$ and $w'$ velocity components), we notice that the outer streamwise velocity streaks are flanked by a set of large streamwise vortices that occupy all the wall-normal portion of the flow outside the canopy. The presence of these streamwise oriented vortices is confirmed by the outer peaks of the premultiplied peaks of $v'$ and $w'$ in Figures 4.15 and 4.16.

We next consider the spectra within the canopy region, starting with the dens-

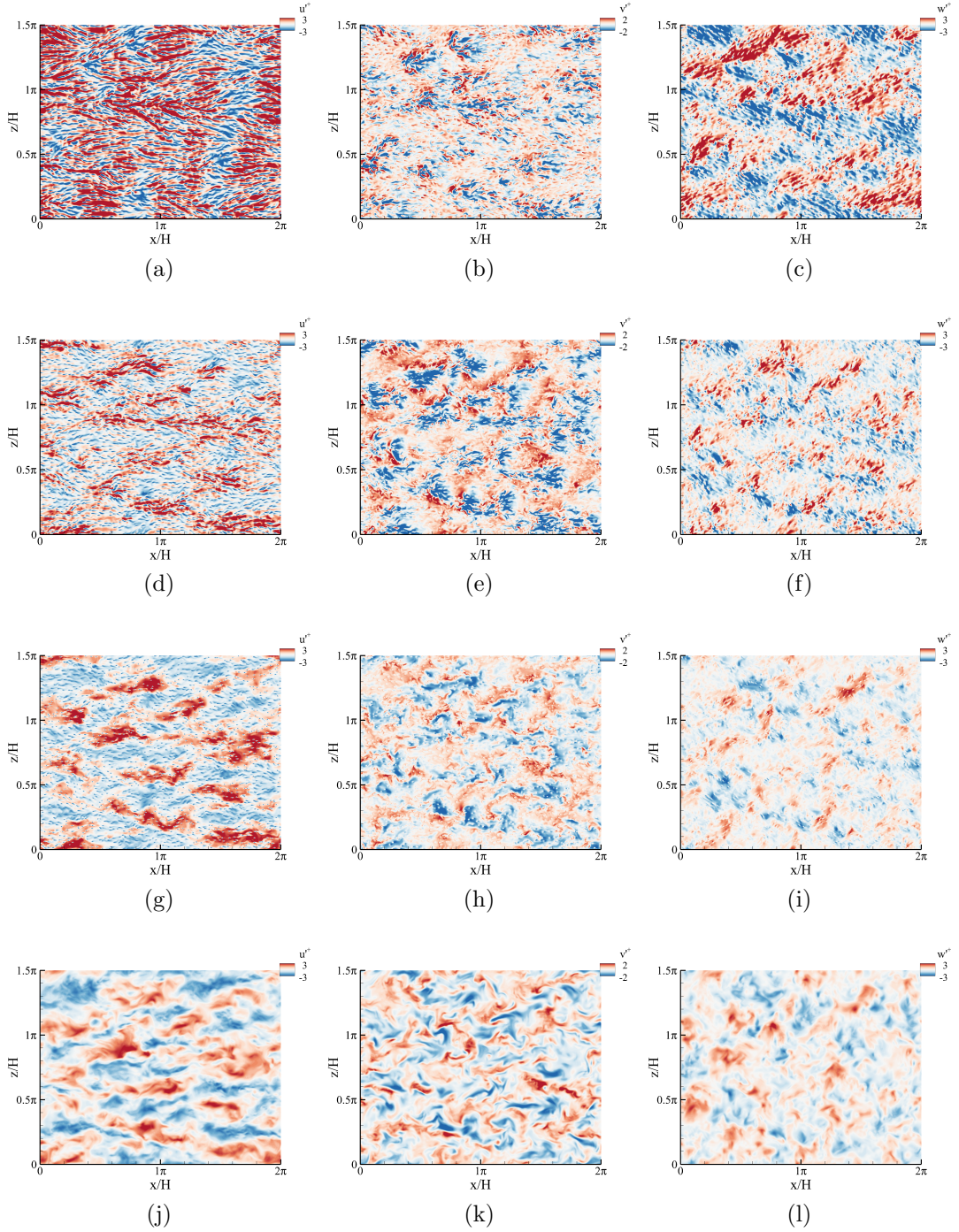


Figure 4.14: Case *DE*. Instantaneous contours of velocity fluctuations on planes parallel to the wall. Panels (a), (d), (g) and (j): $u'/u_{\tau,l}$; Panels (b), (e), (h) and (k): $v'/u_{\tau,l}$; Panels (c), (f), (i) and (l): $w'/u_{\tau,l}$. The planes are located at: $y/H = 0.059$ (location of the lower inflection point), first row; $y/H = 0.275$ (location of the virtual origin), second row; $y/H = 0.40$ (location of the upper inflection point, i.e. the canopy edge), third row; $y/H = 0.50$ (outer region), fourth row.

est case *DE* for which the last rows of Figures 4.15 and 4.16 show the presence of two distinct, interior peaks in the energy content of the three velocity fluctuations components. The leftmost peaks in the spectra of $u'$ and $w'$ (panels (j) and (l) of Figure 4.16) are associated with a spanwise length $\lambda_z \simeq \Delta S$ and are therefore imputable to the internal meandering motion imposed by the presence of the stems (also visible by the fine spanwise textures of the velocity isocontours (a-d) and (c-f) of the planar snapshots of Figure 4.14). The leftmost peaks of $u'$ and $w'$ in the bottom row of Figure 4.16 show that the associated streamwise wavelength takes on a value between $h$ and $\Delta S$ which is probably related to the coherence length of the wakes formed around the stems.

For sparser conditions, the leftmost peak of $u'$ and $w'$ is still observable in Figure 4.16 (i.e. spanwise structures) just below the location of maximum curvature of the mean velocity profile. Differently, Figure 4.15 (i.e. streamwise structures) shows a trend of the leftmost peak in merging with the rightmost peak when the value of $\lambda$ is decreased. It is also noticed that the leftmost peaks associated with the $v'$ fluctuations in Figures 4.15 and 4.16 are located in the same locations as the ones of the cospectra of $\langle u'v' \rangle$ shown in Figure 4.10.

The rightmost peaks inside the canopy of the premultiplied spectra of $u'$ and $w'$ are associated with larger space scales and thus generated by a different physical mechanism. Focusing on the dense case *DE* (panels (j) and (l) of both premultiplied spectra of $u'$ and $w'$) and looking at panels (a) and (c) of Figure 4.14, we realise that a new set of structures is introduced, with the $u'$ and $w'$ fluctuations organised in stripes that are highly coherent in the spanwise direction in the $u'$ case and along a diagonal direction for the $w'$ case. This organization explains why the spectra of $u'$ do not have a clear second peak in panel (j) of Figure 4.16 while $w'$ does in panel (l) of the same figure. Considering again Figure 4.14 and comparing panels (a) and (c) (corresponding to planes located by the wall normal position of the rightmost peak in the spectra of $u'$ and $w'$) with panels extracted further away from the wall, it becomes quite evident that the flow structure is very different. This observation leads to the conclusion that the region close to the bed is almost decoupled from the regions of the canopy closer to its tip, at least in the denser cases.

The spectra of Figure 4.16 show that the rightmost peaks of $u'$ and $w'$ share the same wavelengths as the rightmost peak of $v'$ (in the outer flow, or by the canopy tip) although located at different distances from the wall. This correlation is also visually evident from the snapshots of Figure 4.11 showing a large penetration of the outer quasi-streamwise vortices into the canopy in the wall-normal direction. Since the canopy acts as a porous medium with a $y$ permeability much larger than the in-plane $x - z$ ones, the flow that reaches the bottom wall must deviate its momentum to preserve the wall impermeability and the solenoidal condition generating new scales for the $u'$ and $w'$ components.

All the aforementioned structures, i.e. the ones triggered by the two inflection

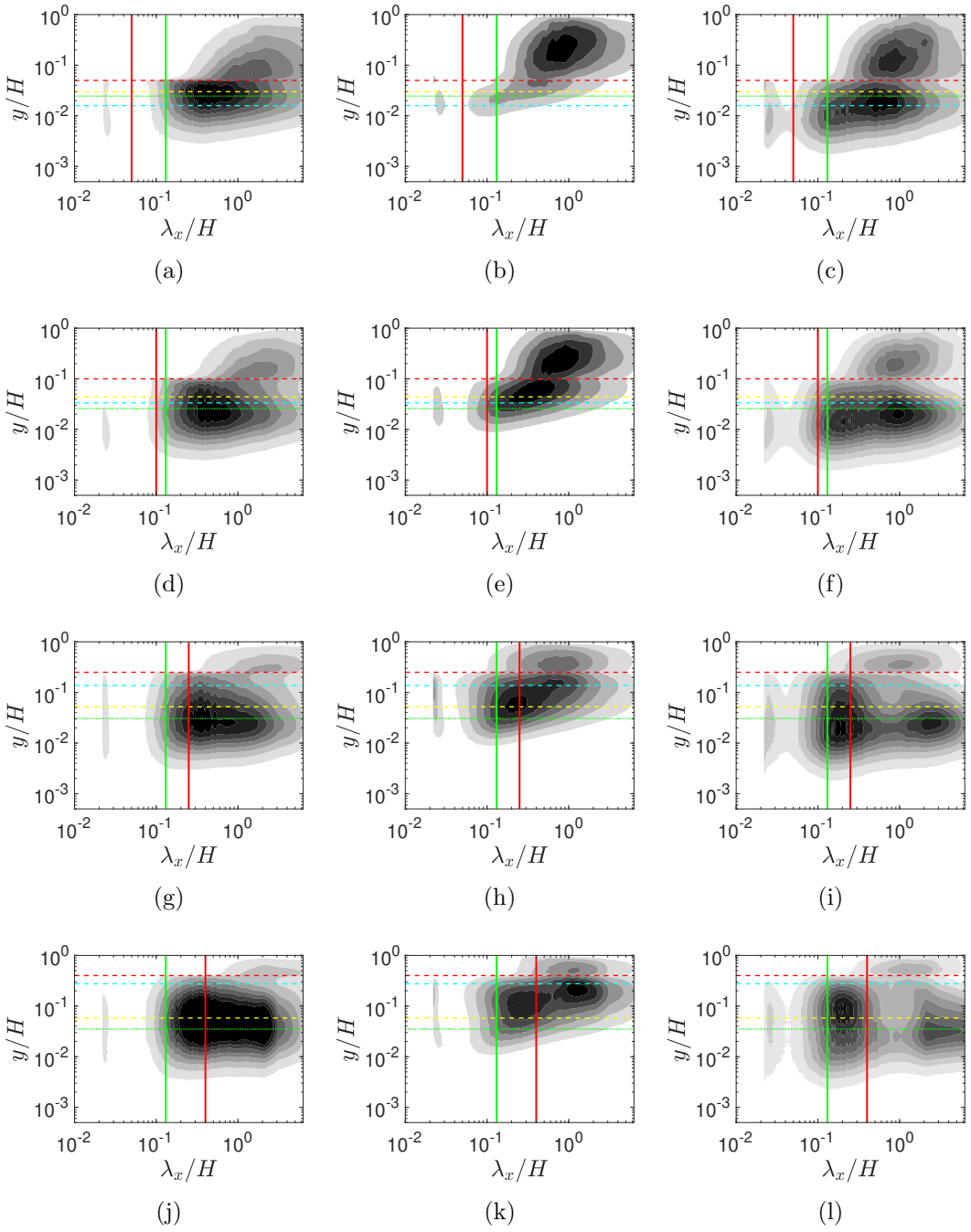


Figure 4.15: Premultiplied spectra of the velocity components as a function of the streamwise wavelength and the wall-normal coordinates in wall units. Panels (a), (d), (g) and (j): $\kappa_x \Phi_{u'u'}/u_{\tau,l}^2$ with grey levels range in $[0, 0.8]$ with a 0.1 increment; Panels (b), (e), (h) and (k): $\kappa_x \Phi_{v'v'}/u_{\tau,l}^2$ with grey levels range in $[0, 0.3]$ with a 0.03 increment; Panels (c), (f), (i) and (l): $\kappa_x \Phi_{w'w'}/u_{\tau,l}^2$ with grey levels range in $[0, 0.5]$ with a 0.05 increment. The first row (panels a, b and c) refers to the *MS* case; the second row (panels d, e, and f) refers to the *TR* case; the third row (panels g, h, and i)refers to the *MD* case; the fourth row (panels j, k, and l)refers to the *DE* case. Colour lines have the same meaning as in Figure 4.10.

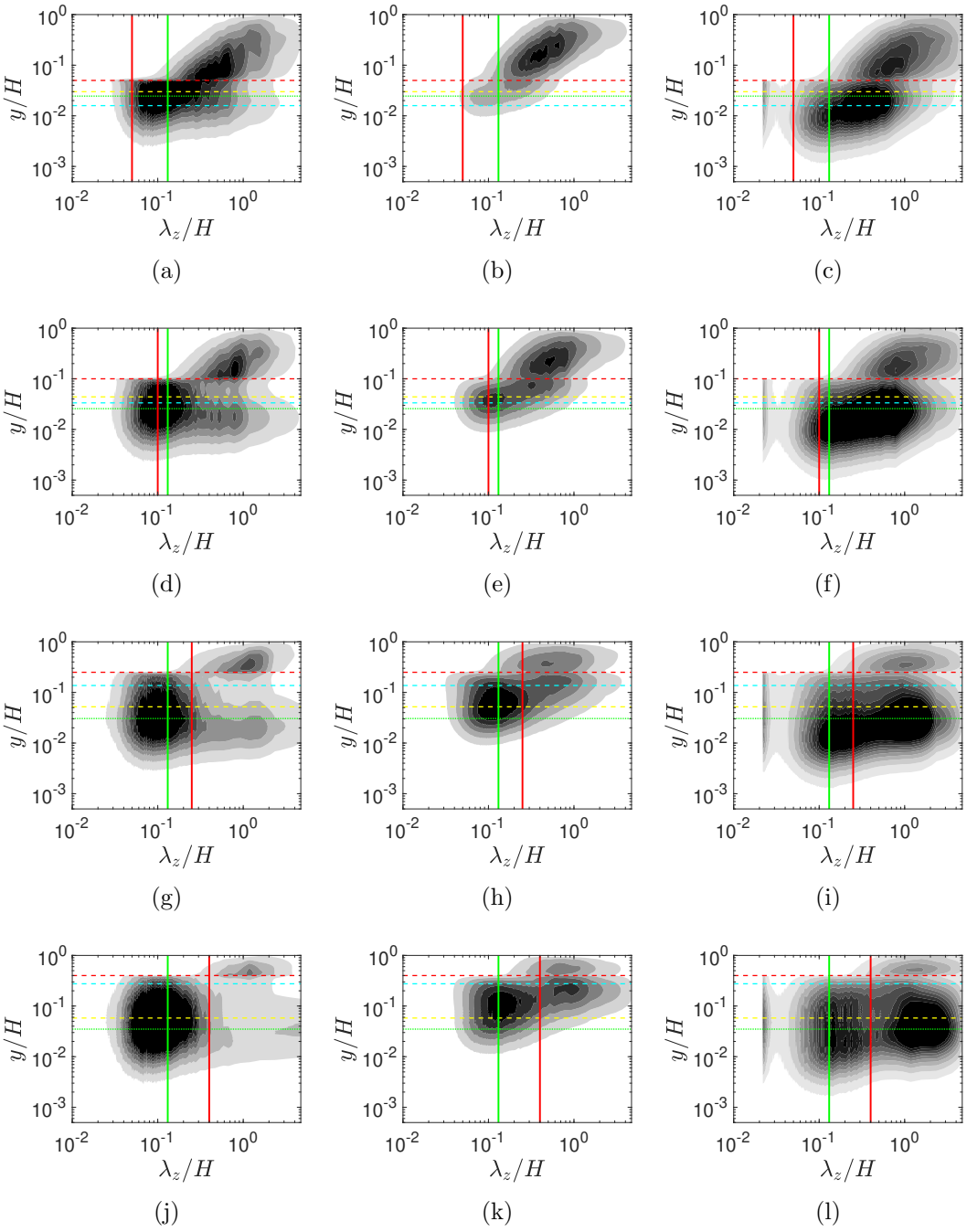


Figure 4.16: Premultiplied spectra of the velocity components as a function of the spanwise wavelength and the wall-normal coordinates in wall units. Panels (a), (d), (g) and (j): $\kappa_z \Phi_{u'u'}/u_{\tau,l}^2$ with grey levels range in $[0, 1.05]$ with a 0.15 increment; Panels (b), (e), (h) and (k): $\kappa_z \Phi_{v'v'}/u_{\tau,l}^2$ with grey levels range in $[0, 0.3]$ with a 0.05 increment; Panels (c), (f), (i) and (l): $\kappa_z \Phi_{w'w'}/u_{\tau,l}^2$ with grey levels range in $[0, 0.5]$ with a 0.05 increment. Rows ordering, as in Figure 4.15 and colour lines have the same meaning as in Figure 4.10.

points as well as the ones driven by the outer coherent large scale motions are in continuous interaction. However, this interaction is almost limited to the wall normal direction due to the high $y$ permeability of the canopy. This high normal permeability fixes the location of the interior inflection point in a situation that resembles the one of a set of radial jets of cross-section $\Delta S - d$ striking normally into the bed (Banyassady and Piomelli, 2015). The wall normal permeability also establishes the momentum exchange between large scale structures within and outside the canopy.

## 4.3 Conclusions

In this chapter, we have undertaken a parametric study based on the variations of the thickness of the baseline canopy studied in Chapter 3. The key objective of the analysis was to characterise the different flow regimes that emerge as a result of the variations of the $\lambda$ value and to establish a sound physical criterion enabling an a-priori prediction of the inner and outer canopy flow features. We found that the wall-normal location of the three points that characterise the mean velocity profile inside the canopy, i.e. the two inflection points and the location of the virtual origin of the outer flow, plays a key role in determining the establishment of a particular regime. Specifically, the passage from the transitional towards the dense scenario is regulated by the relative location of the inner inflection point and the virtual origin. These locations define two natural boundaries for the inner and outer flows. When the two flows are separated (i.e. the virtual origin stands above the inner inflection point) the canopy can be considered to be hydrodynamically dense. While Poggi et al. (2004) identified the lower bound for the solidity value $\lambda$ for nonsparse canopies, we have identified a sharp threshold separating the transitional and dense regimes, i.e. $\lambda \approx 0.15$. This specific value, defined through the crossing condition between the virtual origin and the inner inflection point, marks the establishment of different canopy flow regimes.

The parametric study also allowed us to define a length scale that guarantees the collapse of the Reynolds stresses curves independently of the sparsity of the canopy under consideration. Specifically, while the structure of the outer flow is regulated by the distance between the origin of the outer flow (i.e. the virtual origin) and the open channel height, the size of the most energetic eddies populating the intra-canopy flow is determined by local viscous length scale weighted with a parameter that depends on the density of the canopy.

The chapter ends with a detailed analysis of the flow structures that emerge in the various regimes. Their classification has been carried out through a spectral analysis of the energy content of the velocity fluctuations. We have noticed that the increasing canopy solidity leads to a separation of peaks in the premultiplied spectra of the velocity components. For the densest scenario, we found two sets of

large coherent structures (one inside and one outside the canopy) fed by the two unstable inflection points of the mean velocity profile. The momentum transfer between the two clusters of coherent structures takes place through the wall-normal direction which is characterised by a large permeability.

# Chapter 5

# Conclusions and future works

This doctoral dissertation is centred on the resolved numerical simulation of rigid filamentous canopies. The simulations were used as a tool to unravel the dominant physical mechanisms that determine the character of the different flows that emerge from the interaction of an external turbulent shear flow with canopies of different solidities. In particular we have considered an open channel flow at bulk Reynolds number $Re_b = 6000$ bounded by a filamentous layer whose configuration encompasses various nominal canopy flow regimes: sparse, transitional and dense. One of the most important outcomes of the thesis is of methodological nature as a novel method has been put forward for the resolved simulation of the canopy flows. The numerical approach is based on a modification of an existing immersed boundary method that has been formulated and validated on both a model case and versus experimental data. By taking advantage of the numerical efficiency and accuracy of the developed numerical technique, to the authors' knowledge, this is the first time that a canopy-flow simulation in which the physical boundary values are imposed stem-by-stem has been reported in the literature.

Having assessed the validity of the numerical approach, we have turned our attention to the physical mechanisms that govern the behaviour of canopy flows. To this end, we have conducted a parametric study to unravel the mechanisms that determine the development and the transition between canopy flow regimes, from sparse to dense. Specifically, the parametric analysis has been carried out by varying the canopy height, keeping constant the average spacing among the filament, $\Delta S$, the diameter of the filaments, $d$, the open channel depth, $H$, and the bulk velocity $U_b$, i.e. we kept constant the bulk Reynolds number, $Re_b = U_b\ H/\nu$. The canopies implemented were all made of rigid filaments vertically mounted on an impermeable wall. It is found that the first and second-order statistics of the flow are sufficient to provide an exact classification of the actual regime of the canopy flow. The classification is based on the location of three characteristic points on the mean velocity profile, i.e. the two inflection points

and the location of the virtual wall for the outer flow. We have shown that the interplay between these points determines the occurrence of the transition between regimes. This approach allows the improving of the transition criterion based on the canopy solidity found in the literature (Nepf, 2012a, Poggi et al., 2004). We have characterised the structures that dominate the different regions in an open channel flow over a canopy in all the regimes. In particular, for the dense case scenario, we have clarified the mechanisms of interaction between the large clusters of structures found inside and outside the canopy region. We found that both inflection points are unstable and trigger the presence of large coherent structures inside and outside the canopy layer. This is an absolutely new observation as the instability of the inner inflection point at the genesis of new coherent structures triggered by its nonlinear evolution has never been reported in the literature before.

Despite the modest exploration of the parametric space, this thesis opens a new research strand on the analysis of canopy flows. The full understanding of the physics of these flows and its consequent exploitation will bring bio-inspired technological innovations. The hydrological management of rivers, energy harvesting and wings covered with filaments for flow control purpose are just few examples of the potential applications of technologies based on a smart exploitation of this type of distributed fluid-structure interaction.

One of the major tasks in the continuation of the present research concerns the enlargement of the parametric space that influences the global behaviour of canopy flows. In particular, the effect of the average filaments distance, $\Delta S$, on the solidity, $\lambda$, should be studied. Changing the size of the tile where each filament is mounted on is expected to lead to a different flow behaviour as the action of the outer streamwise and spanwise momenta can also influence the intra-canopy flow. Indeed, as mentioned in the introduction (Chapter 1), modifying $\lambda$ using either $\Delta S$ or $h$ might bring to two very different limiting behaviours, i.e. a porous media or an emergent canopy, respectively, if $\lambda$ is increased, or a flow around a few cylinders and a flow over a smooth wall when $\lambda$ is decreased. Hence, a parametric study similar to what seen in Chapter 4, possibly keeping the same solidity values used in this work, should be undertaken as a continuation of this research.

Another interesting configuration to be considered before tackling the case of flexible canopies is the one of a canopy built with inclined filaments. This is useful to understand the effect of the solid volume fraction. In fact, according to Nepf (2012a), when the filaments are bent, the effective frontal area, i.e the projection of the frontal area on the wall-normal planes, plays an important role in determining the features of the resulting flow structure. It is also noticed that a canopy made of stems inclined along the streamwise direction is also a simplified model of a very soft canopy deformed by the mean drag. The inclined canopy case would also allow studying dense cases that could be related to porous

media characterised by a complex permeability tensor. Research on these two aforementioned configurations are ongoing and the results will be soon diffused via publication in peer-reviewed journals.

Finally, after having well understood the importance of these extra parameters on rigid canopies, one could incorporate flexible filaments whose structural properties will enlarge the parametric study even more, thus opening more opportunities for engineering canopies that can deliver technological advantages.

# Bibliography


Bailey, B. and Stoll, R. (2013). Turbulence in sparse, organized vegetative canopies: a large-eddy simulation study. *Boundary-Layer Meteorology*, 147(3):369–400.

Bailey, B. and Stoll, R. (2016). The creation and evolution of coherent structures in plant canopy flows and their role in turbulent transport. *Journal of Fluid Mechanics*, 789:425–460.

Balay, S., Abhyankar, S., Adams, M. F., Brown, J., Brune, P., Buschelman, K., Dalcin, L., Eijkhout, V., Gropp, W. D., Kaushik, D., Knepley, M. G., May, D. A., McInnes, L. C., Rupp, K., Smith, B. F., Zampini, S., Zhang, H., and Zhang, H. (2017). PETSc Web page. `http://www.mcs.anl.gov/petsc`.

Banyassady, R. and Piomelli, U. (2015). Interaction of inner and outer layers in plane and radial wall jets. *Journal of Turbulence*, 16(5):460–483.

Belcher, S., Jerram, N., and Hunt, J. (2003). Adjustment of a turbulent boundary layer to a canopy of roughness elements. *Journal of Fluid Mechanics*, 488:369–398.

Böhmer, K., Hemker, P., and Stetter, H. (1984). The defect correction approach. In *Defect correction methods*, pages 1–32. Springer.

Canuto, C., Hussaini, M., Quarteroni, A., Thomas Jr, A., et al. (2012). *Spectral methods in fluid dynamics*. Springer Science & Business Media.

Carruthers, A., Thomas, A., and Taylor, G. (2007). Automatic aeroelastic devices in the wings of a steppe eagle aquila nipalensis. *Journal of Experimental Biology*, 210(23):4136–4149.

Chorin, A. (1968). Numerical solution of the Navier–Stokes equations. *Mathematics of Computation*, 22(104):745–762.

Costanza, R., d'Arge, R., De Groot, R., Farber, S., Grasso, M., Hannon, B., Limburg, K., Naeem, S., O'neill, R., Paruelo, J., et al. (2016). The value of the

world's ecosystem services and natural capital (1997). *The Globalization and Environment Reader*, page 117.

Cui, J. and Neary, V. (2008). LES study of turbulent flows with submerged vegetation. *Journal of Hydraulic Research*, 46(3):307–316.

Dauptain, A., Favier, J., and Bottaro, A. (2008). Hydrodynamics of ciliary propulsion. *Journal of Fluids and Structures*, 24(8):1156–1165.

Drazin, P. and Reid, W. H. (1981). *Hydrodynamic stability*. Cambridge university press.

Fadlun, E., Verzicco, R., Orlandi, P., and Mohd-Yusof, J. (2000). Combined immersed-boundary finite-difference methods for three-dimensional complex flow simulations. *Journal of Computational Physics*, 161(1):35–60.

Favier, J., Revell, A., and Pinelli, A. (2014). A Lattice Boltzmann–Immersed Boundary method to simulate the fluid interaction with moving and slender flexible objects. *Journal of Computational Physics*, 261:145–161.

Ferziger, J. and Peric, M. (2012). *Computational methods for fluid dynamics*. Springer Science & Business Media.

Finnigan, J. (2000). Turbulence in plant canopies. *Annual Review of Fluid Mechanics*, 32(1):519–571.

Finnigan, J., Shaw, R., and Patton, E. (2009). Turbulence structure above a vegetation canopy. *Journal of Fluid Mechanics*, 637:387–424.

Flores, O. and Jiménez, J. (2006). Effect of wall-boundary disturbances on turbulent channel flows. *Journal of Fluid Mechanics*, 566:357–376.

García-Mayoral, R. and Jiménez, J. (2011). Hydrodynamic stability and breakdown of the viscous regime over riblets. *Journal of Fluid Mechanics*, 678:317–347.

Gardiner, M. (2005). The importance of being cilia. *HHMI Bulletin*, 18(2):32–37.

Ghisalberti, M. and Nepf, H. (2002). Mixing layers and coherent structures in vegetated aquatic flows. *Journal of Geophysical Research: Oceans*, 107(C2).

Ghisalberti, M. and Nepf, H. (2004). The limited growth of vegetated shear layers. *Water Resources Research*, 40(7).

Guilmineau, E. and Queutey, P. (2002). A numerical simulation of vortex shedding from an oscillating circular cylinder. *Journal of Fluids and Structures*, 16(6):773–794.

Hama, F. R. (1954). Boundary layer characteristics over smooth and rough surfaces. *Transactions - The Society of Naval Architects and Marine Engineers*, 62:333.

Harman, I. and Finnigan, J. (2007). A simple unified theory for flow in the canopy and roughness sublayer. *Boundary-Layer Meteorology*, 123(2):339–363.

Hoyas, S. and Jiménez, J. (2008). Reynolds number effects on the Reynolds-stress budgets in turbulent channels. *Physics of Fluids*, 20(10):101511.

Huang, J., Cassiani, M., and Albertson, J. (2009). The effects of vegetation density on coherent turbulent structures within the canopy sublayer: a large-eddy simulation study. *Boundary-Layer Meteorology*, 133(2):253–275.

Itoh, M.and Iguchi, R., Yokota, K., Akino, N., R., H., and S., K. (2006). Turbulent drag reduction by the seal fur surface. 18 - 065102.

Jiménez, J. (2004). Turbulent flows over rough walls. *Annual Review of Fluid Mechanics*, 36:173–196.

Jiménez, J. (2013). Near-wall turbulence. *Physics of Fluids*, 25(10):101302.

Jiménez, J. (2018). Coherent structures in wall-bounded turbulence. *Journal of Fluid Mechanics*, 842:1–100.

Jiménez, J. and Pinelli, A. (1999). The autonomous cycle of near-wall turbulence. *Journal of Fluid Mechanics*, 389:335–359.

Jiménez, J., Uhlmann, M., Pinelli, A., and Kawahara, G. (2001). Turbulent shear flow over active and passive porous surfaces. *Journal of Fluid Mechanics*, 442:89–117.

Kim, J. and Moin, P. (1985). Application of a fractional-step method to incompressible Navier–Stokes equations. *Journal of Computational Physics*, 59(2):308–323.

Kim, J., Moin, P., and Moser, R. (1987). Turbulence statistics in fully developed channel flow at low Reynolds number. *Journal of Fluid Mechanics*, 177:133–166.

Lang, A., Bradshaw, M., Smith, J., Wheelus, J., Motta, P., Habegger, M., and Hueter, R. (2014). Movable shark scales act as a passive dynamic micro-roughness to control flow separation. *Bioinspiration & Biomimetics*, 9(3):036017.

Lee, E., Ranasinghe, D., Ahangar, F., Amini, S., Mara, S., Choi, W., Paulson, S., and Zhu, Y. (2018). Field evaluation of vegetation and noise barriers for mitigation of near-freeway air pollution under variable wind conditions. *Atmospheric Environment*, 175:92–99.

Leonard, A. (1975). Energy cascade in large-eddy simulations of turbulent fluid flows. *Advances in Geophysics*, 18:237–248.

Leonardi, S., Orlandi, P., and Antonia, R. A. (2007). Properties of d- and k-type roughness in a turbulent channel flow. *Physics of Fluids*, 19(12):125101.

Lightbody, A. and Nepf, H. (2006). Prediction of velocity profiles and longitudinal dispersion in salt marsh vegetation. *Limnology and Oceanography*, 51(1):218–228.

Liu, D., Diplas, P., Fairbanks, J., and Hodges, C. (2008). An experimental study of flow through rigid vegetation. *Journal of Geophysical Research: Earth Surface*, 113(F4).

Liu, W., Chen, Y., Uras, R., and Chang, C. (1996). Generalized multiple scale reproducing kernel particle methods. *Computer Methods in Applied Mechanics and Engineering*, 139(1-4):91–157.

Liu, W., Jun, S., and Zhang, Y. (1995). Reproducing kernel particle methods. *International Journal for Numerical Methods in Fluids*, 20(8-9):1081–1106.

López, F. and García, M. (2001). Mean flow and turbulence structure of open-channel flow through non-emergent vegetation. *Journal of Hydraulic Engineering*, 127(5):392–402.

Mars, R., Mathew, K., and Ho, G. (1999). The role of the submergent macrophyte triglochin huegelii in domestic greywater treatment. *Ecological Engineering*, 12(1):57–66.

Mittal, R. and Iaccarino, G. (2005). Immersed boundary methods. *Annual Review of Fluid Mechanics*, 37:239–261.

Mizuno, Y. and Jiménez, J. (2013). Wall turbulence without walls. *Journal of Fluid Mechanics*, 723:429–455.

Monti, A., Omidyeganeh, M., and Pinelli, A. (2019). Large-eddy simulation of an open-channel flow bounded by a semi-dense rigid filamentous canopy: Scaling and flow structure. *Physics of Fluids*, 31(6):065108.

Moser, R., Kim, J., and Mansour, N. (1999). Direct numerical simulation of turbulent channel flow up to $Re_\tau$= 590. *Physics of Fluids*, 11(4):943–945.

Muzaferija, S. (1994). *Adaptive finite volume method for flow prediction using unstructured meshes and multigrid approach.* PhD thesis, University of London UK.

Nepf, H. (2012a). Flow and transport in regions with aquatic vegetation. *Annual Review of Fluid Mechanics*, 44:123–142.

Nepf, H. (2012b). Hydrodynamics of vegetated channels. *Journal of Hydraulic Research*, 50(3):262–279.

Nepf, H. and Vivoni, E. (2000). Flow structure in depth-limited, vegetated flow. *Journal of Geophysical Research: Oceans*, 105(C12):28547–28557.

Nezu, I. and Sanjou, M. (2008). Turbulence structure and coherent motion in vegetated canopy open-channel flows. *Journal of Hydro-Environment Research*, 2(2):62–90.

Nikuradse, J. (1933). *Strömungsgesetze in rauhen Rohren.* VDI-Verlag.

Okamoto, T. and Nezu, I. (2009). Turbulence structure and "monami" phenomena in flexible vegetated open-channel flows. *Journal of Hydraulic Research*, 47(6):798–810.

Omidyeganeh, M. and Piomelli, U. (2011). Large-Eddy Simulation of two-dimensional dunes in a steady, unidirectional flow. *Journal of Turbulence*, (12):N42.

Omidyeganeh, M. and Piomelli, U. (2013a). Large-Eddy Simulation of three-dimensional dunes in a steady, unidirectional flow. Part 1. turbulence statistics. *Journal of Fluid Mechanics*, 721:454–483.

Omidyeganeh, M. and Piomelli, U. (2013b). Large-Eddy Simulation of three-dimensional dunes in a steady, unidirectional flow. Part 2. flow structures. *Journal of Fluid Mechanics*, 734:509–534.

Ong, L. and Wallace, J. M. (1998). Joint probability density analysis of the structure and dynamics of the vorticity field of a turbulent boundary layer. *Journal of Fluid Mechanics*, 367:291–328.

Pan, Y., Follett, E., Chamecki, M., and Nepf, H. (2014). Strong and weak, unsteady reconfiguration and its impact on turbulence structure within plant canopies. *Physics of Fluids (1994-present)*, 26(10):105102.

Perry, A. E., Schofield, W. H., and Joubert, P. N. (1969). Rough wall turbulent boundary layers. *Journal of Fluid Mechanics*, 37(2):383–413.

Peskin, C. (1972). Flow patterns around heart valves: a numerical method. *Journal of Computational Physics*, 10(2):252–271.

Pinelli, A., Naqavi, I., Piomelli, U., and Favier, J. (2010). Immersed-boundary methods for general finite-difference and finite-volume Navier–Stokes solvers. *Journal of Computational Physics*, 229(24):9073–9091.

Pinelli, A., Omidyeganeh, M., Brücker, C., Revell, A., Sarkar, A., and Alinovi, E. (2017). The PELskin project: part IV—control of bluff body wakes using hairy filaments. *Meccanica*, 52(7):1503–1514.

Piomelli, U., Rouhi, A., and Geurts, B. (2015). A grid-independent length scale for large-eddy simulations. *Journal of Fluid Mechanics*, 766:499–527.

Poggi, D., Porporato, A., Ridolfi, L., Albertson, J., and Katul, G. (2004). The effect of vegetation density on canopy sub-layer turbulence. *Boundary-Layer Meteorology*, 111(3):565–587.

Raupach, M., Finnigan, J., and Brunei, Y. (1996). Coherent eddies and turbulence in vegetation canopies: the mixing-layer analogy. *Boundary-Layer Meteorology*, 78(3-4):351–382.

Raupach, M. and Thom, A. (1981). Turbulence in and above plant canopies. *Annual Review of Fluid Mechanics*, 13(1):97–129.

Ree, W. and Palmer, V. (1949). *Flow of water in channels protected by vegetative linings*. Number 967. US Department of Agriculture.

Rhie, C. and Chow, W. (1983). Numerical study of the turbulent flow past an airfoil with trailing edge separation. *AIAA Journal*, 21(11):1525–1532.

Roma, A., Peskin, C., and Berger, M. (1999). An adaptive version of the immersed boundary method. *Journal of Computational Physics*, 153(2):509–534.

Rosti, M. (2016). *Direct numerical simulation of an aerofoil at high angle of attack and its control*. PhD thesis, City, University of London.

Rosti, M., Omidyeganeh, M., and Pinelli, A. (2016). Direct numerical simulation of the flow around an aerofoil in ramp-up motion. *Physics of Fluids*, 28(2):025106.

Rouhi, A., Piomelli, U., and Geurts, B. (2016). Dynamic subfilter-scale stress model for large-eddy simulations. *Physical Review Fluids*, 1(4):044401.

Schlichting, H. (1936). Experimentelle untersuchungen zum rauhigkeitsproblem. *Archive of Applied Mechanics*, 7(1):1–34.

Schultz, M. P. and Flack, K. A. (2009). Turbulent boundary layers on a systematically varied rough wall. *Physics of Fluids*, 21(1):015104.

Scotti, A. (2006). Direct numerical simulation of turbulent channel flows with boundary roughened with virtual sandpaper. *Physics of Fluids*, 18(3):031701.

Sharma, A. and García-Mayoral, R. (2018). Turbulent flows over sparse canopies. In *Journal of Physics: Conference Series*, volume 1001, page 012012. IOP Publishing.

Shimizu, Y., Tsujimoto, T., Nakagawa, H., and Kitamura, T. (1991). Experimental study on flow over rigid vegetation simulated by cylinders with equispacing. *Doboku Gakkai Ronbunshu*, 1991(438):31–40.

Sundin, J. and Bagheri, S. (2019). Interaction between hairy surfaces and turbulence for different surface time scales. *Journal of Fluid Mechanics*, 861:556–584.

Townsend, A. (1976). *The structure of turbulent shear flow*. Cambridge university press.

Tuerke, F. and Jiménez, J. (2013). Simulations of turbulent channels with prescribed velocity profiles. *Journal of Fluid Mechanics*, 723:587–603.

Vogel, S. (1984). Drag and flexibility in sessile organisms. *American Zoologist*, 24(1):37–44.

Vogel, S. (1989). Drag and reconfiguration of broad leaves in high winds. *Journal of Experimental Botany*, 40(8):941–948.

Watanabe, T. (2004). Large-eddy simulation of coherent turbulence structures associated with scalar ramps over plant canopies. *Boundary-Layer Meteorology*, 112(2):307–341.

Williamson, C. (1996). Vortex dynamics in the cylinder wake. *Annual Review of Fluid Mechanics*, 28(1):477–539.

Yang, U. et al. (2002). Boomeramg: a parallel algebraic multigrid solver and preconditioner. *Applied Numerical Mathematics*, 41(1):155–177.

Zhang, L., Gerstenberger, A., Wang, X., and Liu, W. (2004). Immersed finite element method. *Computer Methods in Applied Mechanics and Engineering*, 193(21-22):2051–2067.